Quantification of Particle Size Distribution with Different Analytical and Statistical Techniques

Hamid Reza Sam

64226

Faculty of Geosciences, Geotechnics, and Mining

Advanced Mineral Resources Development

Technical University Bergakademie Freiberg

March 2021

Declaration of Authorship

I declare that all information in this document has been obtained and presented under academic rules and ethical conduct. I also say that, as required by these rules and behavior, I have cited and referenced some material and results that are not original in this work. This also applies to all figures, drawings included in the thesis.

Freiberg, 25.03.2021

_____

Hamid Reza Sam

Abstract

Global trends of increasing ore complexity, growing demand for mineral resources, and rising social, environmental, and health issues awareness of mining have led the mining sector, as the primary sector of many national economies, to implement sustainable and resource-efficient strategies. Geological and geometallurgical block models of the resources and reserves play a crucial role in resource efficiency, along with the management of mines and tailings (dumps). Data must flow into such models throughout all stages, from designing and planning and operation stages from exploration to reclamation and rehabilitation. In this regard, early knowledge of ore and waste characteristics is necessary for, e.g., early-stage constraints on the mine system's geotechnical stability or the physical-chemical behavior of dumps and tailings, and of course, for defining mine products and concentrate qualities. An analytical technique to characterize modal mineralogy, mineral association, and grain size distribution of ore and waste samples is scanning electron microscope based automated mineralogy (such as mineral liberation analysis, MLA, or Zeiss Mineralogical) which provides detailed information on many single particles, albeit on the polished section of the sample and not concerning the whole volume. In this study, a method to reconstruct the true 3D size (with uncertainty) from such 2D sections will be developed using Bayes' Theorem. This study constructs particle size distributions from a combination of 2D individual-particle measurements and bulk particle size distribution measured by sieving and laser diffraction. Verification of the prediction of the statistical model for the 3D sizes were done with data from X-ray computed tomography (XCT).

Keywords: Particle size distribution, MLA, Laser diffraction, X-ray computed tomography, Bayes Theorem, Q-values

Acknowledgments

Table of Contents

List of Figures

List of Tables

List of Abbreviations

PSD   Particle size distribution

LD   Laser diffraction

XCT   X-ray computed tomography

MLA   Mineral liberation analysis

SEM   Scanning electron microscope

BSE   Back scatter electron

EDS   Energy Dispersive X-ray Spectroscopy

2D   Two dimensional

3D   Three dimensional

ECD   Equivalent circular diameter

HIST   Histogram

SEQ   Sequence

Q   Quartile

Chapter 1. Introduction

1.1.   Mining and Particles Size Distribution

Increasing ore complexity and demand for mineral resources led the mining sector, as the primary sector of many national economies, implement sustainable and resource-efficient strategies. Optimized and efficient geological and geometallurgical block models of the resources and reserves play an important role in such resource efficiency throughout the life cycle of mines and tailings (dumps). Data must flow into such models throughout all stages, from designing and planning mines and operation stages from exploration to reclamation (rehabilitation); hence, early knowledge of ore and waste characteristics is necessary. A critical characteristic of minerals particles is particle size distribution (PSD), which plays a crucial role in optimization in various stages of mining and other industries. For instance Wu et al. (2018) showed that optimizing the particle size distribution of the aggregate in the cemented rockfill could improve the loading capacity of the backfill to improve the filling effect, and it could decrease the internal stress of the rock mass to reduce the potential dangers around the coalface, such as rockburst. In another example, in a hard coal mine, Skubacz et al. (2016) implement the results of particle size distributions of ambient aerosols, the assessment of the radioactive particle size distribution of the short-lived radon decay products, and the corresponding values of dose conversion factors. Furthermore, Harris et al. (2015) examined the particle size distributions of rock dust, which uses as a mitigation for the hazard of float coal dust that can contribute to a significant underground coal mine explosion. Al-Thyabat et al. (2007) shows the estimation of the sieve size distribution of particles moving on a conveyor belt. In a bigger scale in surface mining, Zhou et al. (2019) predicted the particle size distribution of a muck-pile after blasting, which directly affects the costs of drilling and blasting the subsequent economic growth operations of loading, hauling, and crushing.

1.2.   Relevance and Importance of PSD

Several techniques characterize PSD; these techniques include physical operations like sieving and sedimentation, and spectroscopic techniques like laser diffraction (LD), image analysis based on optical and electron microscopy, and electrozone instruments (Li et al., 2019). Some of these analytical techniques, including sieving and LD, measure the particle size of the whole sample population (bulk sample) and not on an individual particle; nevertheless, they are much

faster and cheaper than image-based techniques. On the other hand, techniques such as X-ray computed tomography (XCT) and scanning electron microscope (SEM) can measure the particle size of individual particles. One of the conventional SEM-based techniques to characterize particle is the mineral liberation analysis system (MLA), which integrates Back Scatter Electron (BSE) and Energy Dispersive X-ray Spectroscopy (EDS) analyses (Fandrich et al., 2007). It is performed on sliced and polished specimens, which can be a section of a drill core or an epoxy block containing the particles to be analyzed. Due to the 2D nature of SEM-EDS, obtaining 3D features like size and volumetric composition exhibits a stereological bias (Furat et al., 2018). The advantage of measuring characteristics such as mineral grain size in three-dimensions is that the stereological issues that bias many measurements made on polished sections are removed (Evans et al., 2015), albeit the 3D measurement of XCT increases time and costly greatly on an industrial scale. Therefore, assessing the actual 3D particle size distributions from simple 2D measurements is a fundamental problem both in scientific and industrial applications (Benito et al., 2019).

1.3.   Background

The key problem has been mentioned in classic stereological textbooks (Russ and Dehoff, 2000). In previous researches, Goldsmith (1967) developed a theoretical solution based on integrated kernels to relate the true distribution of spherical shape particle sizes to the apparent distribution seen in a thin slice. Orive (1976) presented a theoretical solution to the problem, in terms of the continuous, bivariate distributions involved, for spherical shape particles. Eisenhour (1996) provided a procedure that describes chondrule (spherical shape) sizes and relative abundances derived from thin-section data by considering non-diametrical cuts from random cuts of a sphere and the specific thickness of cuts. Sahagian and Proussevitch (1998) applied a numerical technique and showed for the first time that the vital parameter controlling calculated size distribution is particle aspect ratio; this allows the technique be applied to a range of particle shapes and sizes (multidispersal) and not only spherical shapes. However, the reliability of these estimates is also probably insufficient for many applications. They also developed stereology as a statistical technique to determine the number of particles of a particular size and shape enclosed by a given volume from the observed number of particle cuts of a particular size and shape in a random cross-section for mono and polydispersal systems (particles at same shape and different sizes). In another work Rickman et al. (2016) used the parameters aspect ratio and Heywood factor (circumference of a circle with the same area as the particle divided by the observed particle perimeter) to calculate particles shape and size in three-

dimensional space by using two-dimensional projections on a plane. Cuzzi and Olson (2017) showed a method to recover spherical shape particles by considering the larger particle effects, as the cuts of bigger particles might be sampled more often than the smaller ones due to their larger diameter and deal with the bias of non-diametrical cuts. They found a method that with a particular inversion using geometrical binning provide the least biased overall results. They proposed a matrix (F) which is a description of how a true diameter distribution (N_v) is represented in a different apparent circle diameter distribution (N_A) as Eq. (1-1). Due to the discrete nature of this matrix representation, the diameter distributions have to be discretized into bins. The upper bin edges are defined, according to the binning method, bin width and number of bins selected. The matrix (F) is determined exclusively by the binning method and its parameters.

$$N_A = F.N_v$$

$$N_v = F^{-1}.N_A$$

(1-1)

The simplicity and flexibility of the method is clear: computing the matrix (F) is extremely simple and many efficient ways to solve linear systems like these are easy to find. Nevertheless, there are two points in their study that could be improved: 1) the quality of predicting the true 3D size of particles depends strongly on the number of bins, i.e. the number of apparent diameters measured; and 2) Any bias on the measurement process is likely to produce incoherent results such as a negative number of observations of the true diameter distribution in some of the smallest bins. Benito et al. (2019) provided a method based on the linear representation of each particle effect on the smaller apparent sizes that are measurable in the 2D plane. They considered thickness of the section and the cuts, which are close to the centre of particle. Furthermore, they demonstrated that the required number of measurements to accomplish detailed recoveries could be reduced by conveniently modifying and complementing it. The two improvements to the original algorithm are 1) the inclusion of either a parametric or a nonparametric fit to the measured data and 2) the utilization of optimization tools to solve the resulting linear system. As we can see, the methods and results to solve the problem derived from different fields such as material science, biology, mineralogy, and all together supplied the basis for solving the 3D recovery problem. More or less, there are the same multiple biases in previous works to recover 3D particle size distribution, as can be list as below:

- Recovering the 2D cuts from sections, which cuts are slightly off the centre of the particle, might be difficult due to limits in the measuring method.
- In random cuts, larger particles will be sampled more often because of their larger sizes.

3

- A random cut is likely to be non-diametrical.
- The sections might have a certain thickness.

1.4. Goal and Aim

In this study, a new 3D size reconstruction method is developed, with the specific objective of obtaining a probability distribution of the 3D particle sizes for each individual particle, by combining its 2D cut from our cross-sections with 3D bulk particle size distribution from the sample population (LD or sieving) as a development for MLA technique. To do this, a combination of analytical techniques is used, and a statistical prediction model is provided that allows the probability distribution of the actual 3D particle size from its 2D cuts to be generated. The model is based on Bayes' Theorem as an inversion method. Bayes' Theorem provides a quantitative relationship between two conditional probability assessments. This thesis is structured as follows; chapter 2 introduces the analytical and statistical methods. The model proposal and diagnostic settings are proposed in chapter 3. In chapter 4 results by using the actual data are shown and at the end in chapter 5, the conclusions, strengths and weaknesses of the study and future works are presented. As a framework for the scope of this master thesis, the following elements are remarked:

Table 1. 1: Scope of the thesis

Included	Excluded
Quantification of 3D particle size uncertainty with different analytical and statistical techniques.	Technical and economic evaluation
Analytical techniques to measure particle size distribution such as sieving, laser diffraction and x-ray computed tomography	Implementation of the method on a case study of underground or surface mining
Statistic based on Bayes Theorem	Use of MLA data as the 2D cuts
Stereological bias reduction for 2D data	--------
Prediction of probability distribution of 3D size of particle by given its 2D cuts	--------
Evaluation of the method performance	--------

Chapter 2. Methodology

A combination of analytical and statistical methods were used to evaluate 3D particle size distribution from the size of 2D cuts of particles. In this chapter, the analytical steps, sample preparation, aim, and purpose of each different analytical techniques will be reported. Afterwards, we will briefly discuss which analysis relates to which step in the statistical model, and each analysis procedure will be explained. Finally, the procedure and role of Bayes' Theorem in this study to predict 3D particle size distribution from a 2D distribution, as applied in this study will be described.
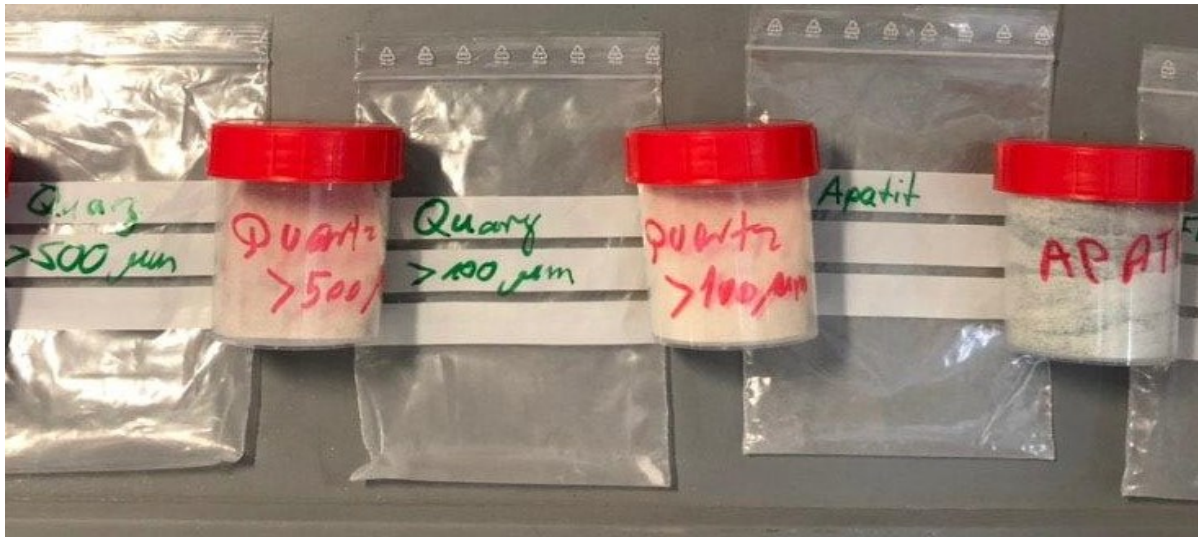
Figure 2. 1: Three different materials, including quartz lump, quartz fine, and apatite

2.1. Analytical Methods and Steps to Measure the PSD

Three different pure materials were chosen; quartz fine, quartz lump, and apatite (Figure 2.1). The reason for choosing quartz and apatite was to observe the effect of shape of minerals in the results of this study. Different analytical techniques were performed depending on their roles in this study (Table 2.1).

These analytical techniques were divided into sample preparation, model construction and validation. For sample preparation grinding and splitting techniques were used. For the obtention of data for model construction, three analytics techniques were applied: sieving, laser diffraction and two-dimensional XCT. Finally, for validation, three-dimensional XCT was used.

Table 2. 2: Analytical techniques and their goals

Goal of analyze	Analytical technique		
Sample preparation	Grinding		Splitting
Model construction	Sieving	Laser diffraction	XCT (2D)
Validation	XCT (3D)		

2.1.1. Sample preparation

To begin with, grinding was applied to reduce the size of particles with a combination of impact and abrasion; it was performed in cylindrical steel vessels (Finch and Wills, 2016). The samples were added to the cylinder with milling balls and the machine ran for 3 minutes. Figure 2.2 shows the machine parts and milling balls were used during the process.

Figure 2. 2: Grinding machine during sample preparation

In the next step, samples were split to have a small representative sample for each material. Depending on the amount of material, two different splitting techniques riffle splitting and rotary splitting.

(a)   (b)
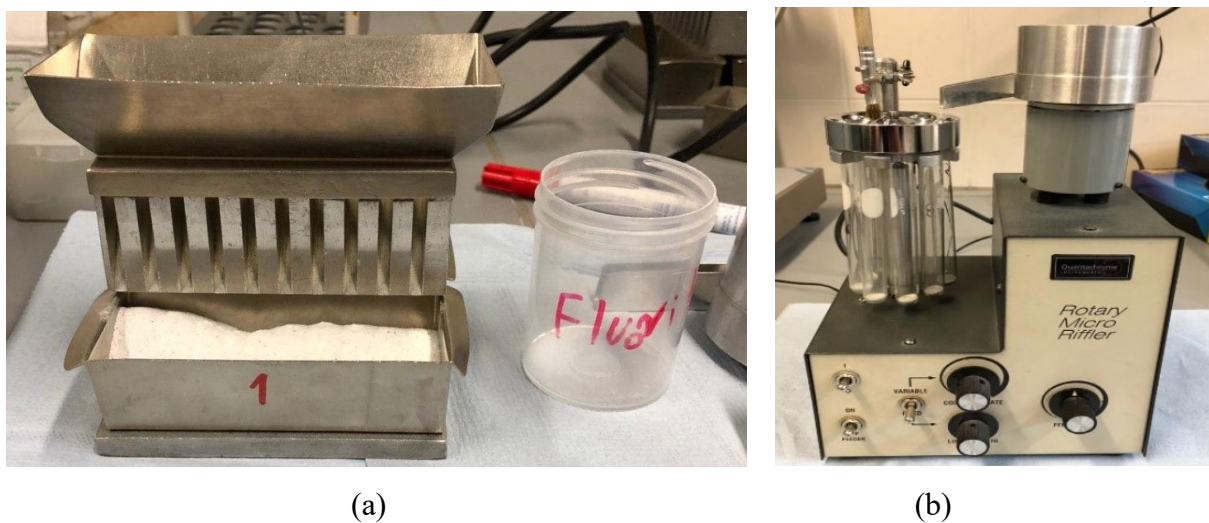
Figure 2. 3: (a) riffles and (b) rotary splitting at Helmholtz Institute Freiberg

A large amount of material was split by riffle and rotary splitting. Twelve to sixteen split samples of each material with an amount of 2-4 grams were retained. These samples were used for analysis in the following steps.

2.1.2. Analytical techniques for model construction

As mentioned before, three analytical techniques were used to construct the statistical model requirements. These analytical methods were divided into sieving, laser diffraction and XCT in 2D. In the following subsections, these analytical techniques are described in detail.

2.1.2.1. Sieving

Sieve analysis (or screening) is one of the oldest methods of size analysis and is performed by passing a known weight of sample material through successively finer sieves and weighing the amount collected on each sieve to determine the percentage weight of each size fraction (Finch and Wills, 2016). In this study, a vibration sieving tower was used with eight sieve size classes.

Figure 2. 4: Vibration sieving tower machine

The mesh sizes of the sieves used were 53, 75, 106, 150, 212, 300, 425 and 600 microns. The sieves were placed from the biggest (600 μm) to the smallest one (53 μm) on the tower, from top to bottom. For having accurate measurements, each material was sieved four rounds, and each round lasts fifteen minutes. After each round of sieving, the tared sieves were weighed. Table 2.3 shows the obtained distribution in detail. Analyses of the fourth round were recorded as the results and shows in Figure 2.5. As it was shown for each material, the distribution is in percentage with a size fraction between 50 to 1000 μm.

Table 2. 3: Sieving results for all materials

Sieve size	Sieve fraction (wt %)		
(µm)	Quartz lump	Quartz fine	Apatite
53	0	1	10
75	0	1	7
106	1	28	6
150	35	59	9
212	32	10	12
300	28	1	17
425	4	0	24
600	0	0	15
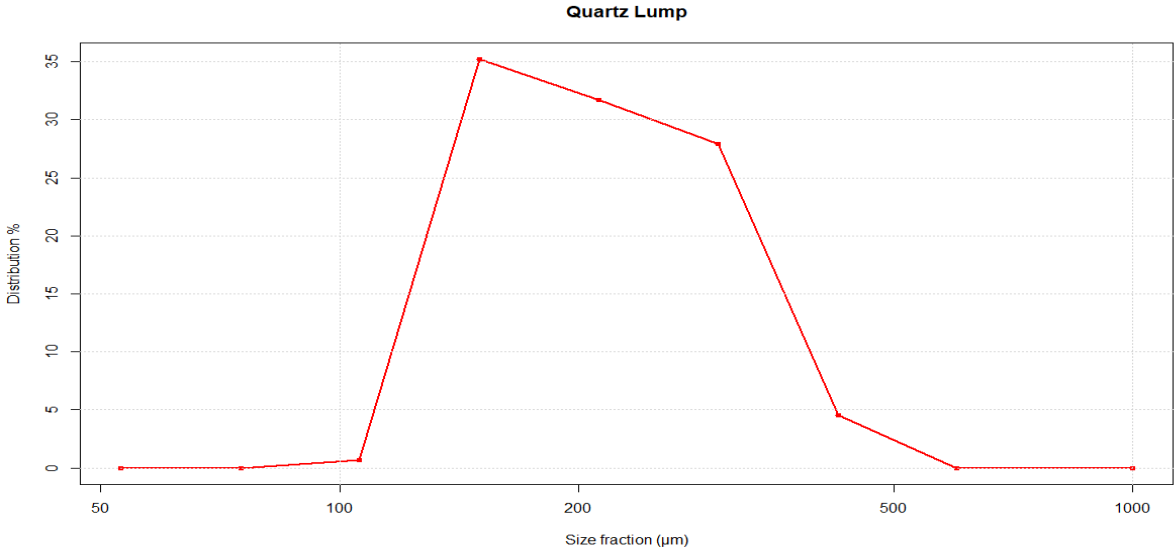
(a)
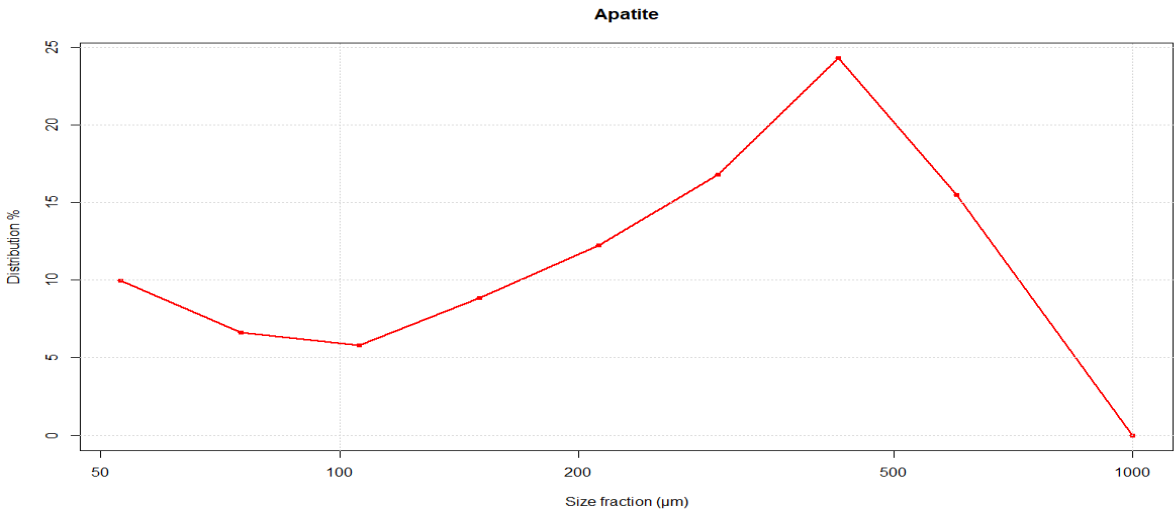
(b)
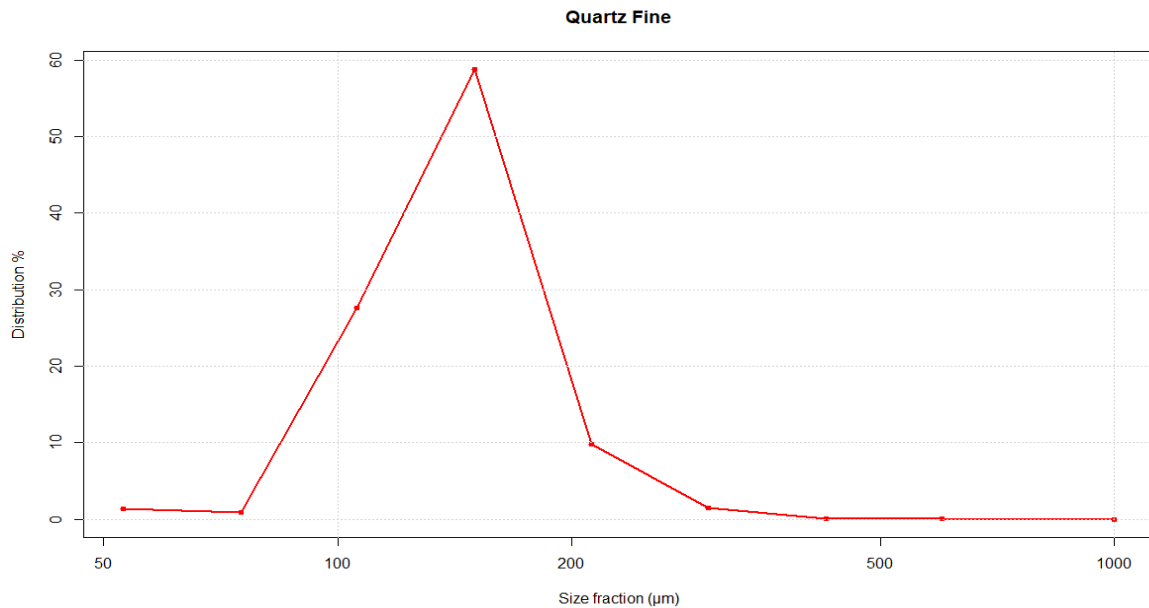
(c)

Figure 2. 5: Sieving results for each material (a) quartz lump (b) apatite (c) quartz fine

2.1.2.2.   Laser Diffraction (LD)

LD is one of the sub-sieve techniques, which allows having results that are typically more accurate on smaller size particles, although this ultimately depends on the characteristics of the material (Li et al., 2019). In this technique, particles flow through a dilute suspension, and laser light is projected through them; the light is scattered by the particles, and the scatter pattern is detected by a solid-state detector measuring light intensity over a range of angles (Finch and Wills, 2016).
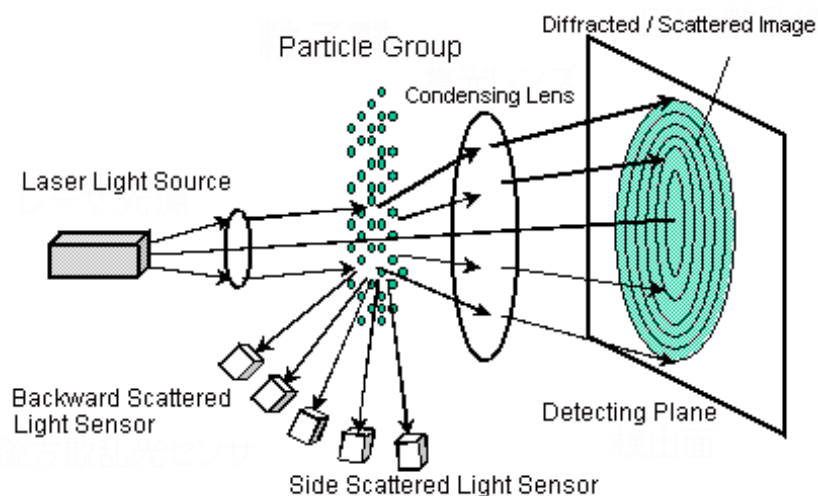
Figure 2. 6: Basic Optical System of an LD particle size analyser (Olawuyi and Asante Samuel, 2016).

A light scattering reconstruction is used to estimate the PSD from the light distribution pattern, thanks to the fact that finer particles induce more scatter than coarser ones. LD instruments are fast, easy to use, and give reproducible results. LD size distributions tend to appear coarser than those of other methods, such as sieving (Finch and Wills, 2016). Care is necessary when comparing output across several environments or materials, or with data obtained by different methods.

Figure 2. 7: LD machine Helos/KR at Helmholtz Institute Freiberg

For each material, four to six samples were measured. In the end, average distribution of each material in percentage with size fractions between 5.5 to 1000 μm was used. Figures 2.8 to 2.10 show the size distribution of particles for each material, and Figure 2.11 shows the average results of each material that can be used as representative data from LD. As the sample materials were monomineralic (one class of mineral), the volume and mass are equivalent because of the constant density.
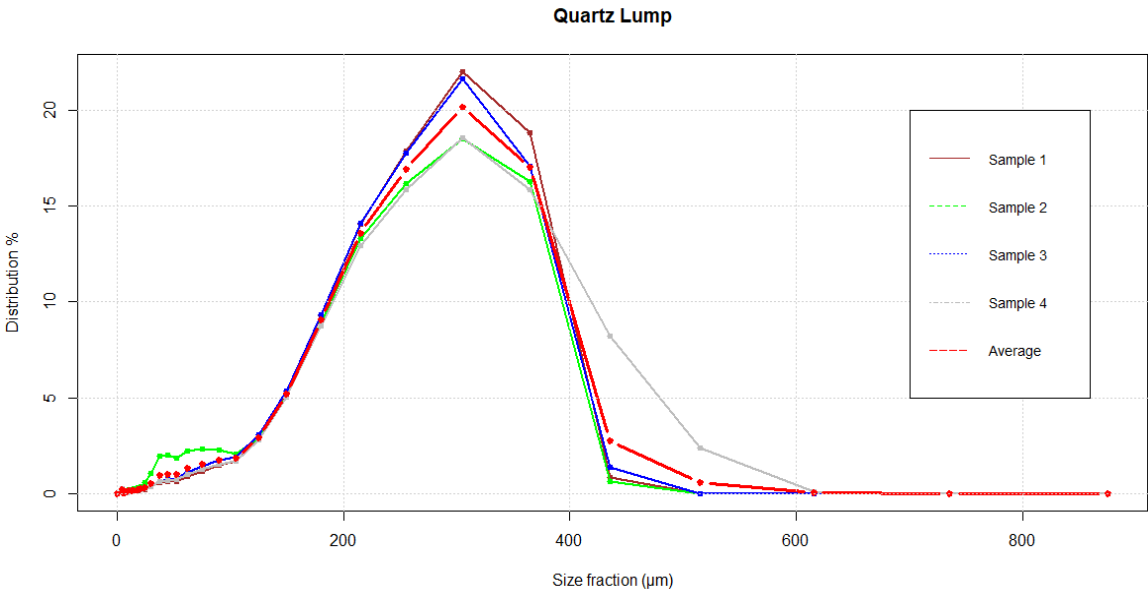
Figure 2. 8: LD result of volume (mass) size distribution for quartz lump.
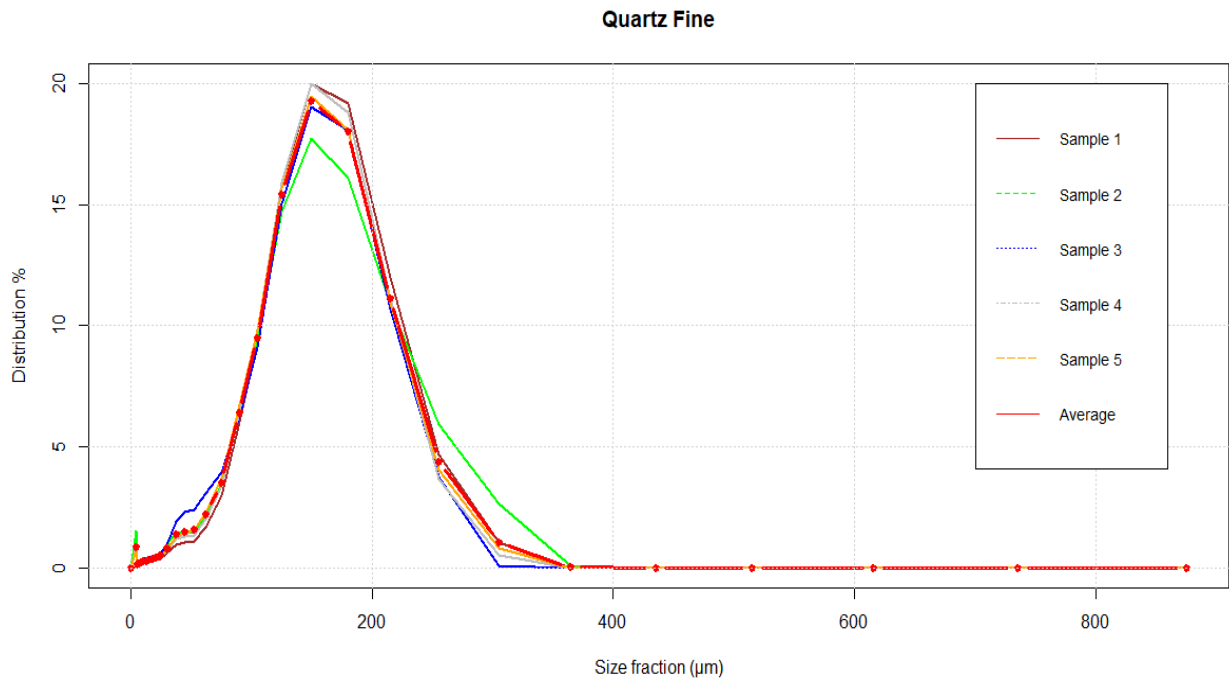
Figure 2. 9: LD result of volume (mass) size distribution for quartz fine.
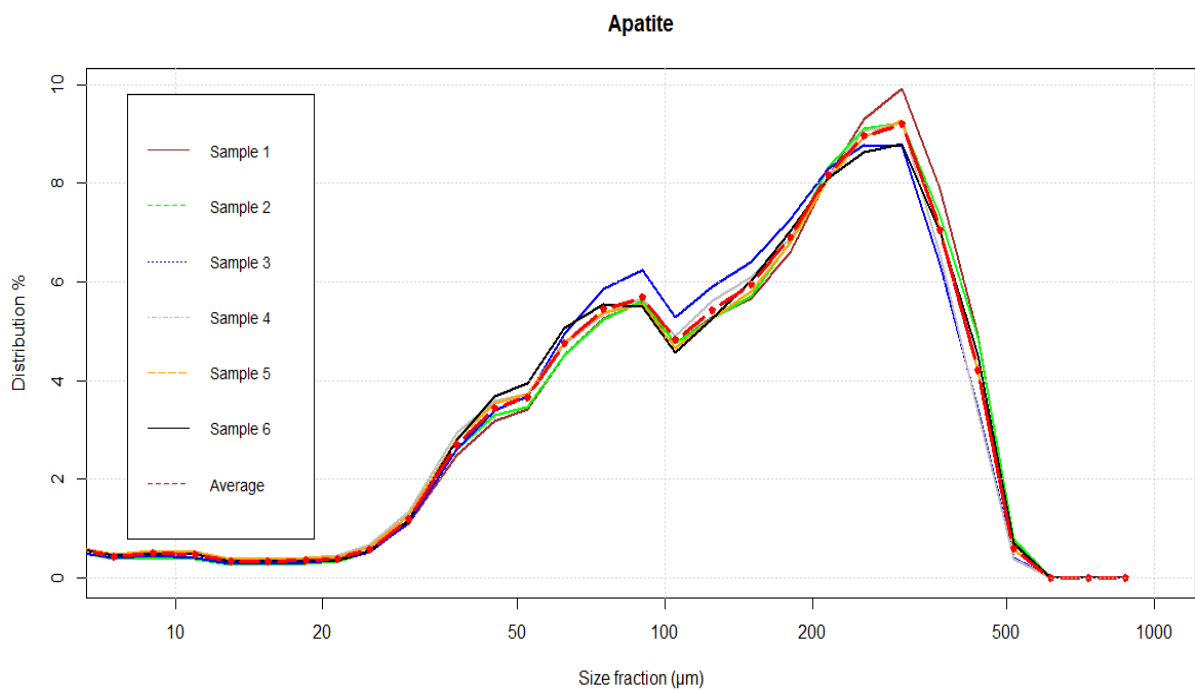
Figure 2. 10: LD result of volume (mass) size distribution for Apatite.

Two measurements of LD and sieving were done. In this study, all materials size was less than one millimetre. Comparison of the laser diffraction method with sieving shows that the number of sieve size fractions in the laser diffraction technique is higher than in the sieving technique and doing the same for sieving with many fine sieve meshes was not worth it. More amount of sieve size fractions help to have more data and smoother graphs and more reliable results on -

11

Table 2. 4: LD results of the average of each material

Sieve size (µm)	Fraction (wt %)		
	Quartz lump	Quartz fine	Apatite
0.5	0	0	0
4.5	0.229	0.852	7.125
5.5	0.061	0.147	0.714
6.5	0.062	0.167	0.556
7.5	0.063	0.171	0.438
9	0.096	0.245	0.498
11	0.131	0.307	0.469
13	0.135	0.289	0.340
15.5	0.174	0.344	0.333
18.5	0.221	0.404	0.355
21.5	0.244	0.411	0.386
25	0.325	0.508	0.575
30	0.547	0.804	1.190
37.5	0.958	1.379	2.705
45	1.011	1.507	3.444
52.5	1.003	1.565	3.661
62.5	1.300	2.230	4.758
75	1.536	3.494	5.441
90	1.761	6.403	5.692
105	1.840	9.502	4.819
125	2.938	15.398	5.426
150	5.175	19.245	5.953
180	9.068	18.029	6.899
215	13.599	11.125	8.185
255	16.915	4.397	8.966
305	20.179	1.035	9.204
365	17.020	0.028	7.045
435	2.770	0	4.218
515	0.597	0	0.591
615	0.031	0	0
735	0	0	0
875	0	0	0
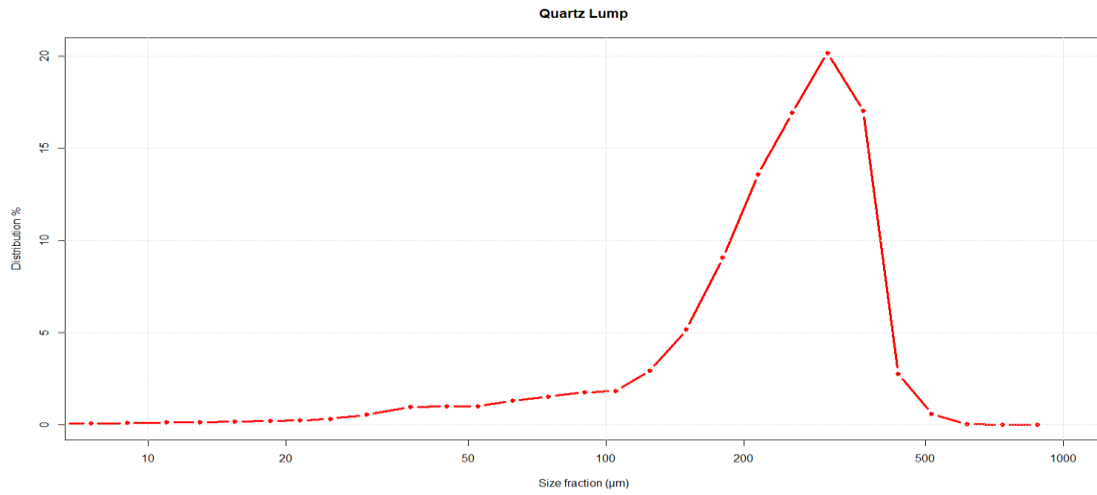
(a)
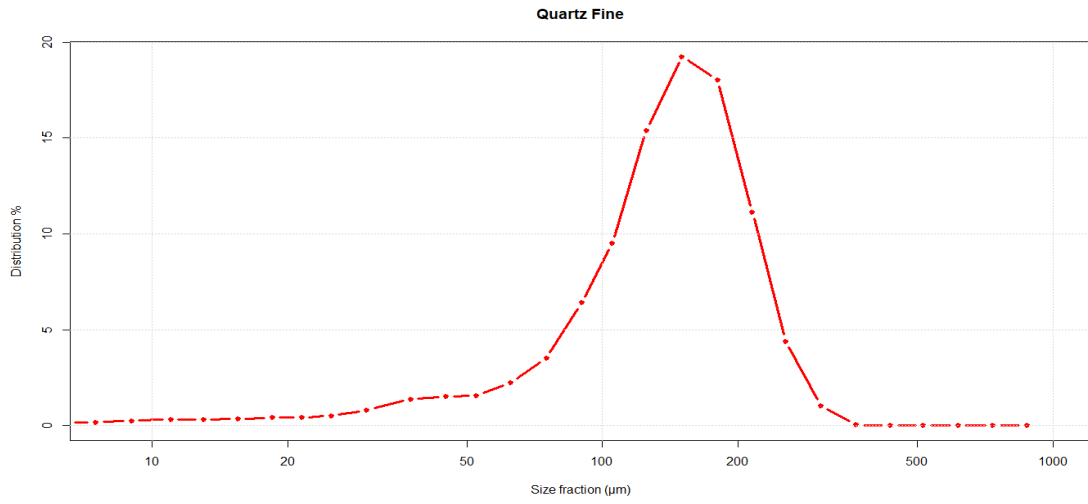
(b)
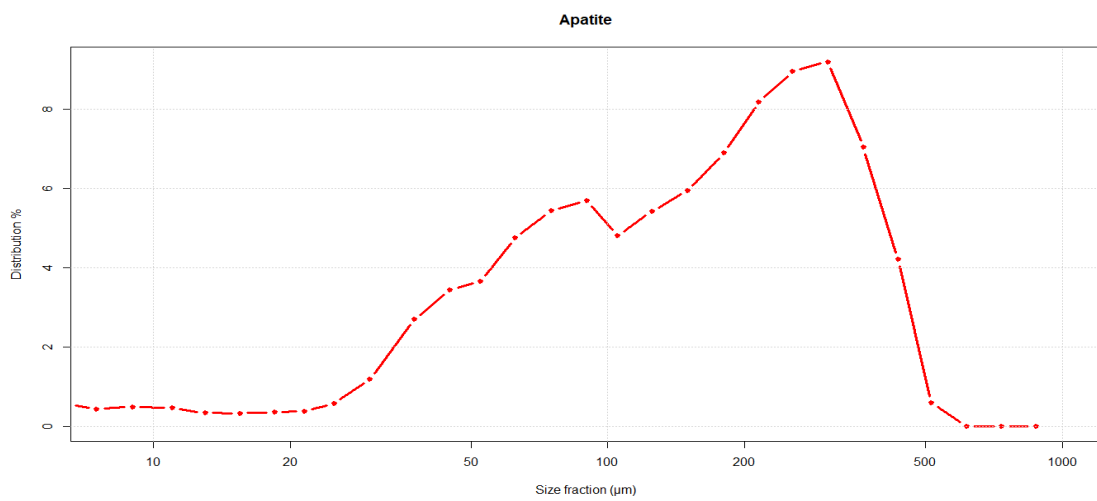
(c)

Figure 2. 11: LD average result of volume (mass) size distribution for materials (a) quartz lump (b) apatite (c) quartz fine

smaller particles. Therefore, results of laser diffraction were chosen for further analysis. However, depending on the size fraction, the divergence between the results of sieving and laser diffraction due to shape and density effects is variable and not easy to predict quantitatively (Dinis and Castilho, 2012; Finch and Wills, 2016).

2.1.2.3. Volume (mass) to number distribution conversion

Some particle size measurement techniques determine number distributions, and some determine volume distributions. For example, LD is typically considered to yield particles sizes, which approximate to a sphere of equivalent volume. So, LD technique primarily provides a volume distribution. Other techniques that measure size distributions on a particle by particle basis, such as image analysis, measure number distributions. Results from number-based systems, such as microscopes or image analysers, construct their initial result as a number distribution. In LD, the use of volume distributions introduces the concept of the equivalent sphere. An equivalent sphere is a sphere equal to real particle in the property that is measured. Thus for light scattering methods, it is a sphere that would produce the same scattering intensities as our fundamental particle; this approximates to a sphere of equal volume, although the more non-spherical a particle is, the greater the error in this approximation will be. Techniques based on number distribution can also be used to calculate a volume distribution when the particle diameters are taken to represent a spherical object's diameter. Here, as we are going to analyse the distribution of single particles, which requires all particles to be considered equally important, a conversion method was needed to convert results of laser diffraction from volume to number distribution (Tomas, 2014). Calculation of volume to number distribution is shown in chapter 4.

2.1.2.4. Micro-X-ray computed tomography

Micro-X-ray computed tomography (XCT) techniques were developed for the medical services field to provide accurate internal images of the human body. Later, XCT techniques started to be used in non-medical applications (Miller et al., 1990). It is a non-destructive technique that allows visualization of the internal structure of objects determined mainly by variations in density and atomic composition (Mees et al., 2003). With this technique, a 3D representation of the sample is generated based on 2D X-ray projections of the specimen acquired in different rotation angles. These projection images are reconstructed to the volume data by calculating the X-ray attenuation coefficient for each voxel using the "back filtered projection" algorithm (Miller et al., 1990). There are various configurations of this technique, such as the sample distance to

the source, the sample size, the required resolution, and the X-ray source energy spectrum (Mees et al., 2003). Its applications are vast in various fields, although the actual results and post-processing steps are different in each field. For doing XCT measurements, the steps are as follows: 1) sample preparation, 2) measurement and reconstruction, 3) image processing, including denoising and binarization, 4) segmentation and 5) data analysis. All steps are described in the following sub-sections. In Figures 2.12 and 2.13, the machine parts and place of sample to analyse are shown schematically.
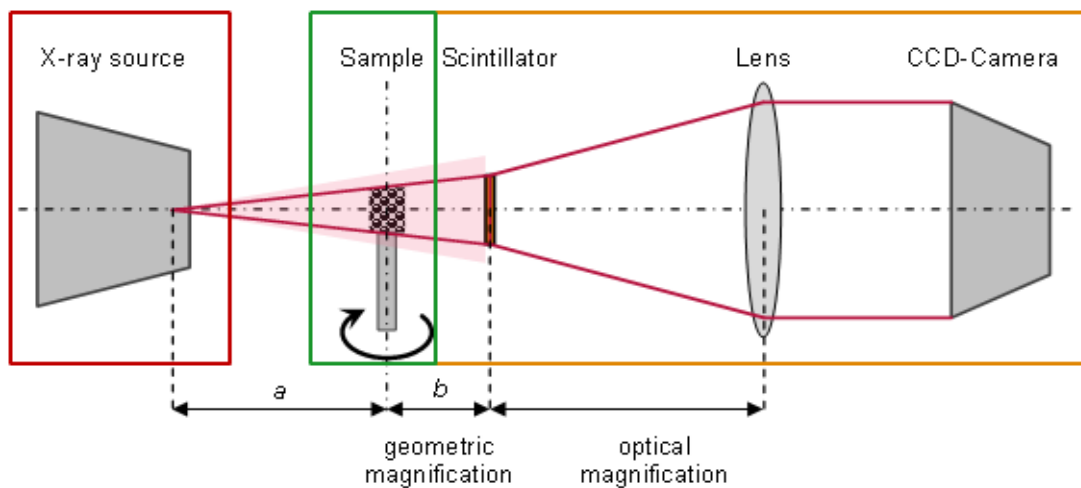
Figure 2. 12: Schematic of XCT measurements machine (Leißner and Peuker, 2017)
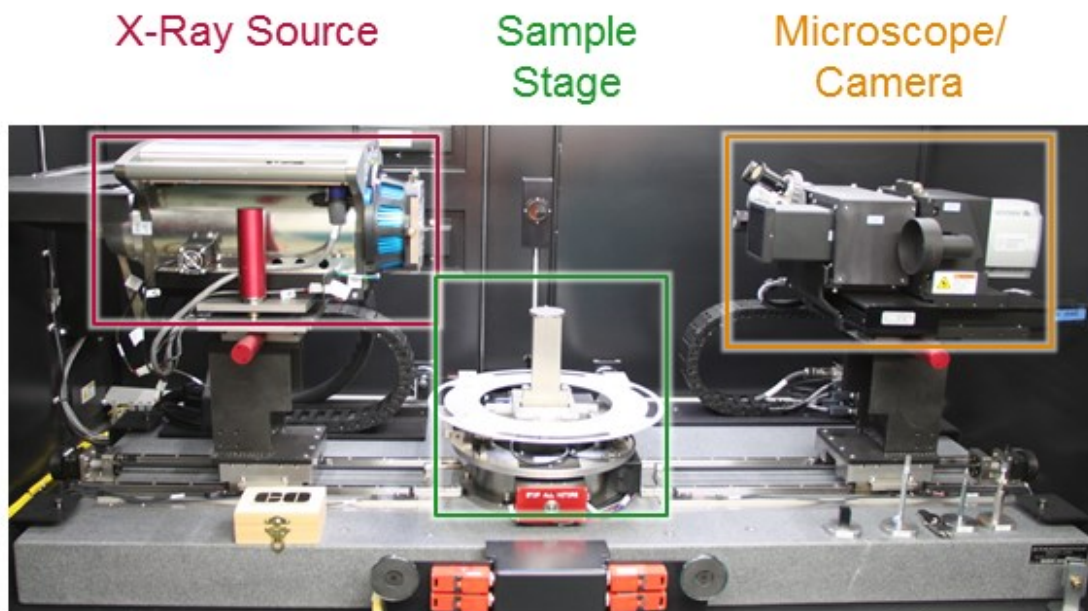
Figure 2. 13: X-ray microscope (XRM) Zeiss Xradia 510 Versa; combined a standard XCT architecture with microscopy optics enabling high-resolution tomography above limits of conventional micro XCT (Leißner and Peuker, 2017).

15

2.1.2.4.1. Sample preparation

As the goal is to develop a method able to deal with data from MLA, the sample preparation for XCT samples was chosen close to the MLA sample preparation. The goal is to have a similar population of particles with similar characteristics and biases to those possibly occurring in a sample for MLA. Two grams of sample material from the splitting step were mixed with one gram of graphite. To achieve better results, the sample size was reduced from 20mm to 10mm in side. In an MLA sample preparation, the step after adding the graphite is to suspend the sample and graphite mixture in two grams of epoxy resin to prepare the grain mount and then vertically cut the resulting epoxy block to get sections in the direction of sedimentation (Furat et al., 2018). After mixing these preparation steps, the samples were sent to the lab to start the XCT measurements.

(a)   (b)
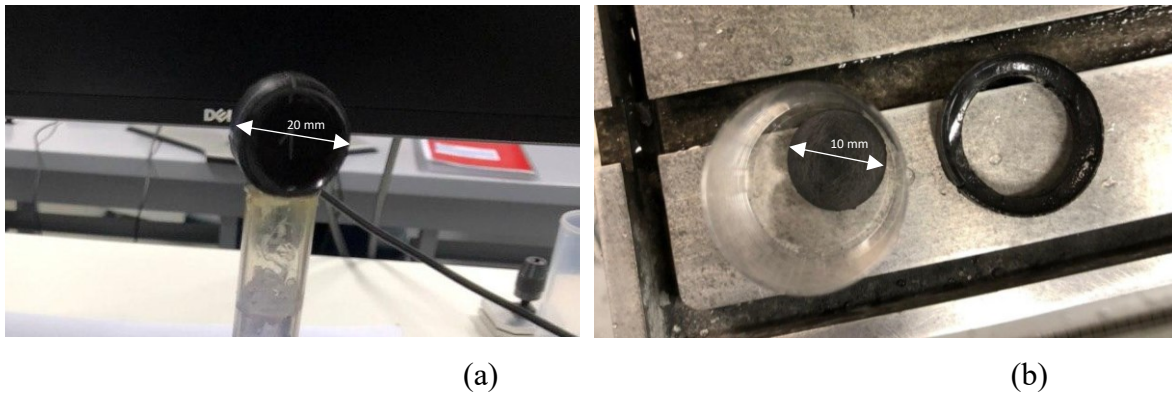
Figure 2. 14: Sample preparation to do XCT measurement (a) before and (b) after decreasing the size.

2.1.2.4.2. Measurement and reconstruction

The samples were scanned using Zeiss Xradia 510 equipment. To attain volumetric data of a sufficient resolution and an appropriate size (3D field of view) a voxel size of 3.7 μm was chosen for the XCT. The parameters of the XCT scan are listed in Table 2.5. The 3D volume reconstruction was done using the Zeiss XRM reconstruction software. This software works with a filtered back-projection algorithm and an additional beam hardening correction method (Leißner and Peuker, 2017). This image reconstruction step creates a series of images that show slices through the particle in cross-section with each slice spaced one voxel apart (Evans et al., 2015). A manual byte scaling is used to adjust the histogram's grayscale values to the range of interest.

Table 2. 5: Parameters for the XCT Scan of the considered Sample

Parameters	Values
Source position (mm)	-25
Detector position (mm)	21
Objective	4X
Camera binning	2
Magnification	4.00
Pixel size (μm)	3.66
Voltage/power (kV/W)	140
Filter	HE2
Exposure time	5
Angle (grad)	360
Projections	2,401

2.1.2.4.3. Image processing

Depending on the aim of XCT measurement and image qualities, different image processing methods are chosen. However, comparing the presentation of various image processing methods on the same set of test images often leads to different results (Schlüter et al., 2014). The methods used were divided into denoising and binarization.

Denoising

Image denoising aims to ease binarization. There are several methods to remove the noise and recover the correct image. The methods should not change the sample features; the main two methods were used for the denoising were non-local means filter and unsharp masking (Schlüter et al., 2014). The procedure was done with Avizo software. In a non-local means filter, the algorithm compares all voxel neighborhoods in a given search window with the current voxel neighbors. The similarity between the neighbors determines the weight with which a voxel value in the search window will influence the new value of the current voxel. The final weights are determined by transforming these similarity values with a Gauss kernel. Unsharp masking is a pervasive filter that sharpens edges on the elements without increasing noise. It first applies a Gaussian filter to a copy of the original image and blends it with the original. Undesired effects are finally reduced by using a mask to only apply sharpening to desired regions of the gradient image above a certain size threshold.

(a)   (b)
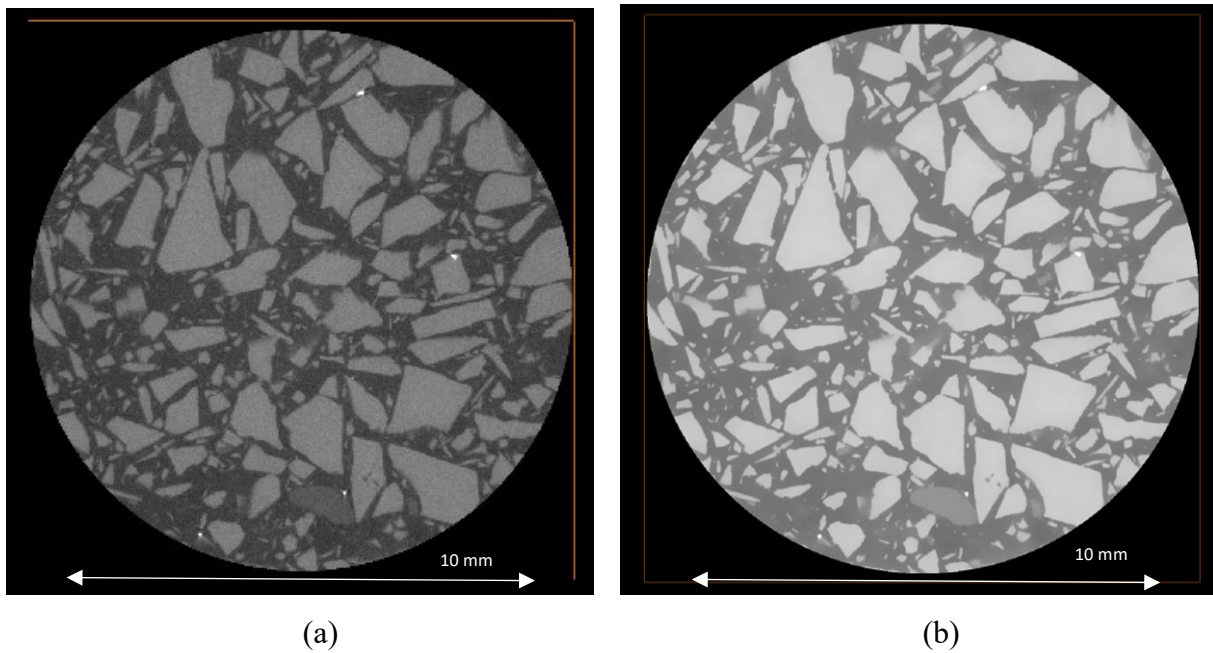
Figure 2. 15: Image (a) before and (b) after non-local means

(a)   (b)
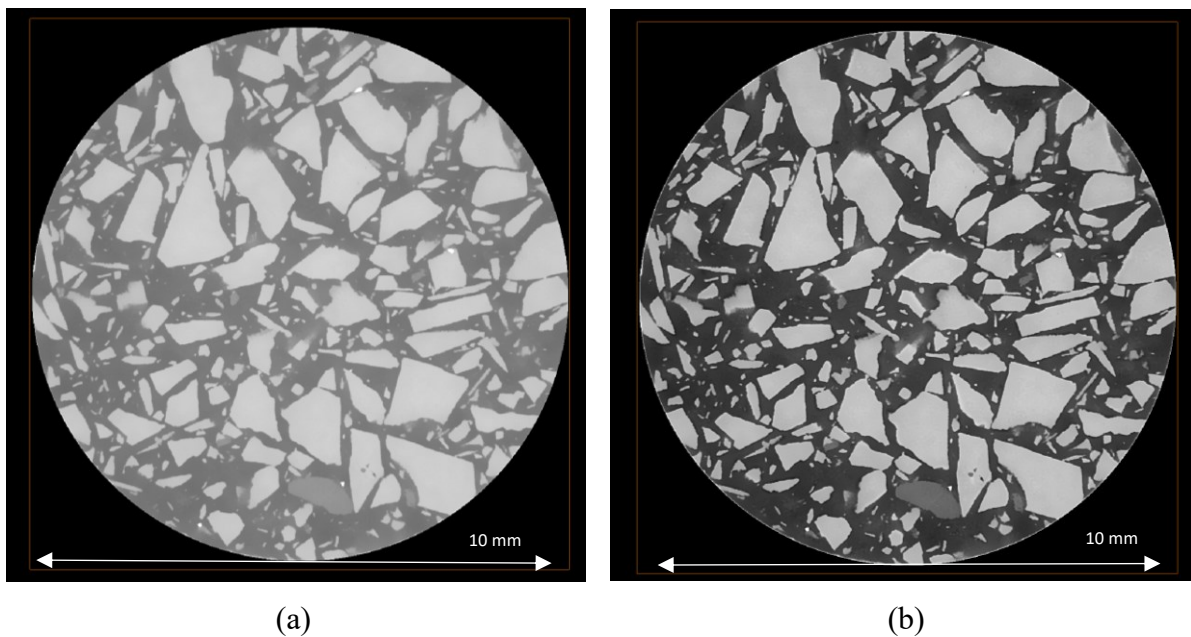
Figure 2. 16: Image (a) before and (b) after unsharp masking

Binarization

Binarization transforms a gray level image into a binary image. This method is used when the gray level image's relevant information corresponds to a specific gray level interval. A gray-scale image is binarized, which means that the foreground phase (particles) is separated from the background (Furat et al., 2018).
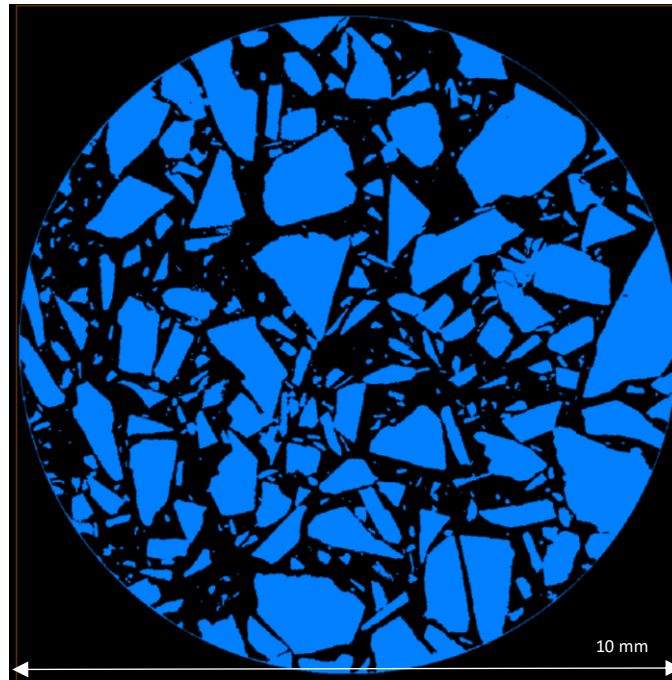
Figure 2. 17: Binarized image (Particles are in foreground with blue color)

2.1.2.4.4. Segmentation and labelling

One of the most complicated procedures for deriving data from XCT measurement is segmentation. There are different comprehensive techniques to do this, depending on the goal and complexity of data and particle characteristics such as shape and size. These techniques include watershed transform, morphological filters, and deep learning. Several filters were tried, and in the end, segmentation results were achieved by using deep learning and watershed transform. In this study, watershed method was suitable for more homogenized samples like quartz, while the deep learning method was better for non-homogenized samples like apatite. The two techniques are described in the following subsections.

Watershed transform and distance map

A classic way of separating touching objects in binary images makes use of the distance transform and the watershed method. The idea is to create a border as far as possible from the centre of the overlapping objects. This strategy works very well on rounded objects and it is called Distance Transform Watershed. It consists of calculating the distance transform of the binary image, inverting it and then applying watershed on it using the original image (Legland et al., 2016). Dragonfly software version 2020.2 was used to operate this method. After doing the binarization and putting the particles to the foreground and the pore space to the background, a distance map on pore space was created and inverted. On the inverted distance map a threshold

range was implemented. The threshold range was a new binary region of interest that gives each particle core but does not connect the particles; otherwise, they would not be separated. The next step was to label the resulting particles. After labeling binarized seeds (particles), the watershed transform was performed. Running the watershed algorithm, seeds grow to the border of each particle, typically without producing over-segmentation. Figure 2.18 shows the process gradually to the end.

Deep learning

Deep learning (also known as deep structured learning) is part of a broader family of machine learning methods based on artificial neural networks with representation learning. Learning can be supervised, semi-supervised or unsupervised (Bengio et al., 2013). In image segmentation, deep learning can learn patterns in visual inputs in order to predict object classes that make up an image. The main deep learning models used for image processing are U-Net (Shelhamer et al., 2017), Autoencoder (Kramer, 1991) and Random forest (Breiman, 2001). In this study, the images were trained with all three models and in the end U-Net model was chosen to run on all of the images. U-Net is based on the fully convolutional network and its architecture is modified and extended to work with fewer training images and to yield more precise segmentations (Shelhamer et al., 2017). For this method, dragonfly software 2020.2 was used. The deep learning method can be directly applied on grayscale images, without need of a preliminary binarization. Random areas in the image that include both particles and background were selected and the software tries different models and shows the results of each deep learning model in a separated windows (Figure 2.19). Depending on complexity of images, around 30-60% of all slices were needed for trainings to have an acceptable result. There was the possibility to compare the models and choose the one with the best segmentation results, which was evaluated visually. After obtaining a suitable segmentation model, the model was operated on whole images slices (sample space).

Labelling

Depending on the segmentation method a connectivity analysis of individual objects in the entire 3D volume needs to be done. Each pixel in an individual object is assigned an identical value, and each object is assigned a different consecutive value, starting from value 1. The assigned value depends on the location of the object in the image (top to bottom, left to right). The maximum value gives the total number of objects in the original binary image and identifies each particle as individual data. Labeled particles are identified with a different color.

(a)

(b)

(c)

(d)

(e)

(f)
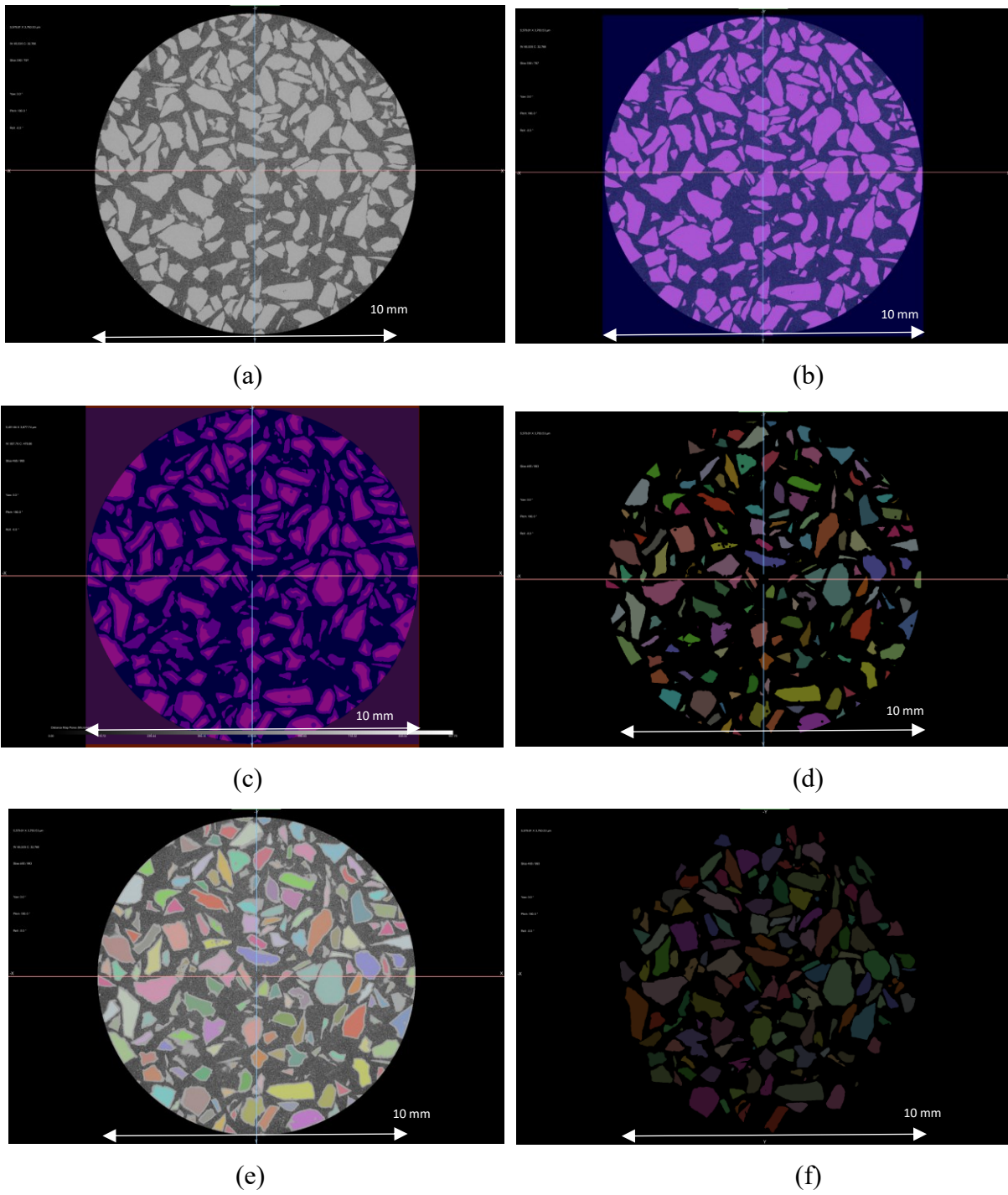
Figure 2. 18: (a) grayscale image, (b) binarized image, (c) applying threshold on inverted distance map (new binarized image) (d) labeling particles (seeds) (e) grayscale image and labeled particles, (f) after running the watershed transform and segmentation is done.
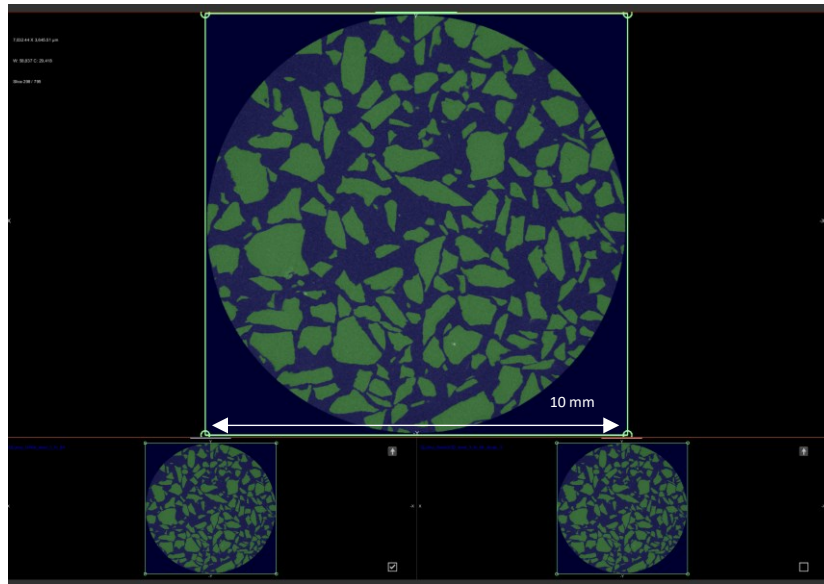
Figure 2. 19: Trained models comparison for doing segmentation.

Figure 2.20 illustrated the labelled particles in 2D and 3D views. In this study, this module was ran in Avizo software with a command name *labelling*. Explicit labelling was not necessary for outcomes of the watershed method.

(a) (b) (c)
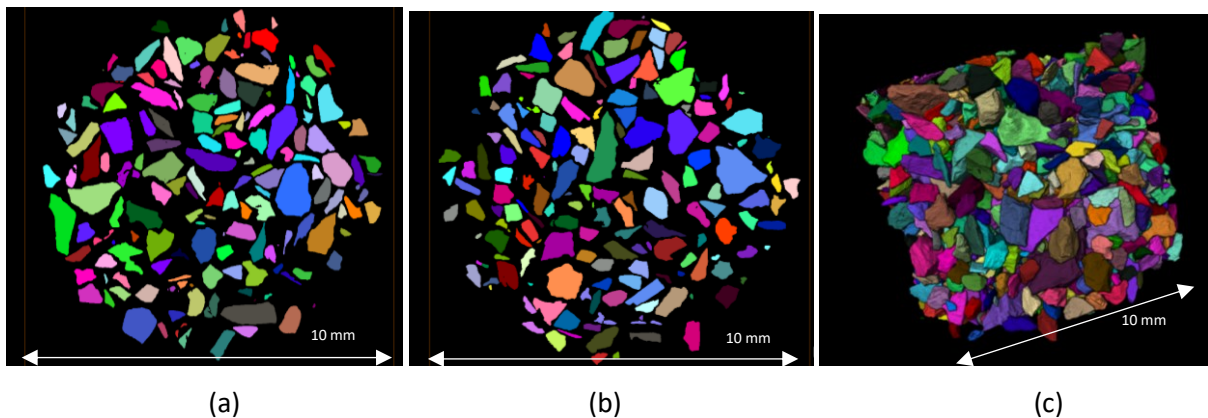
Figure 2. 20: Labeled particles for the mineral quartz lump. (a) and (b) 2D view and (c) 3D view of particles.

2.1.2.4.5. Data analyses

Analysis modules extract data values from an image. The XCT measurements can extract several properties of particles, but the important point is to set measurement parameters depending on the goal and requirements of project. For example, if the purpose is to compare area, diameter, and volume, one can set the measurements as it required. As data from different analytical techniques are combined in one statistical model, the statistical model needs to have one prop-

erty that can describe particle size from all techniques. The equivalent circular (spherical) diameter (ECD) of particles was extracted from XCT data, as the base of these measurements, such as laser diffraction, considers the diameter of particles from its volume. An equivalent circular diameter (ECD) corresponds to the diameter of the circle having the same base area of a circle (2D) or sphere (3D) of the particle.

(a)   (b)
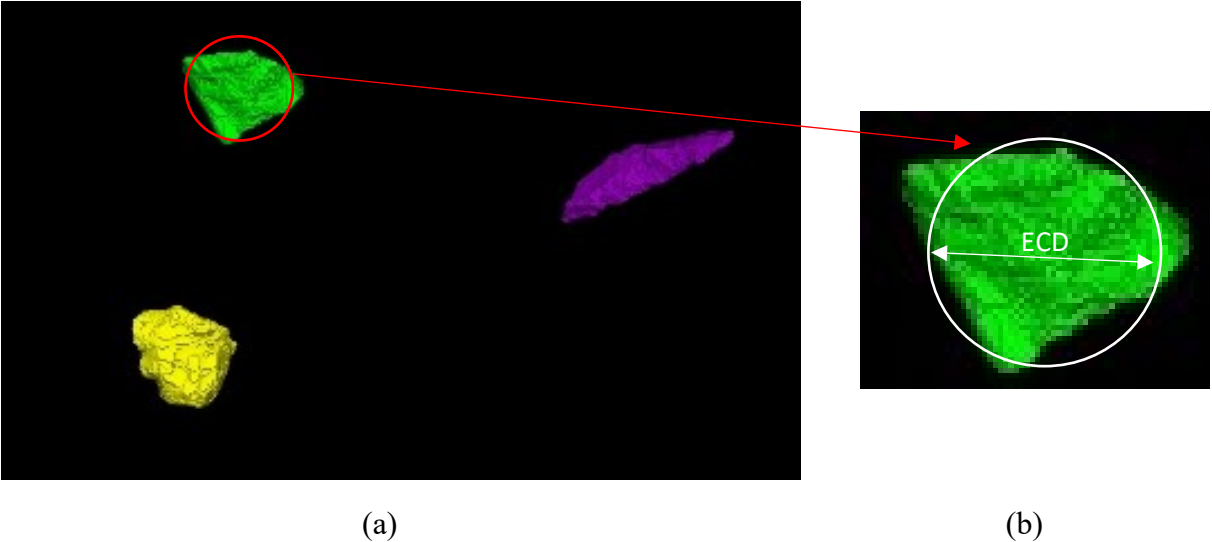
Figure 2. 21: (a) and (b) one labeled particle equivalent circular diameter.

For XCT data, it was necessary to have one series of data in 2D as data of model construction and another series in 3D as validation the method. Therefore, the ECD data of labeled particles were first extracted in 3D and from each particle its 2D cuts were generated as well.
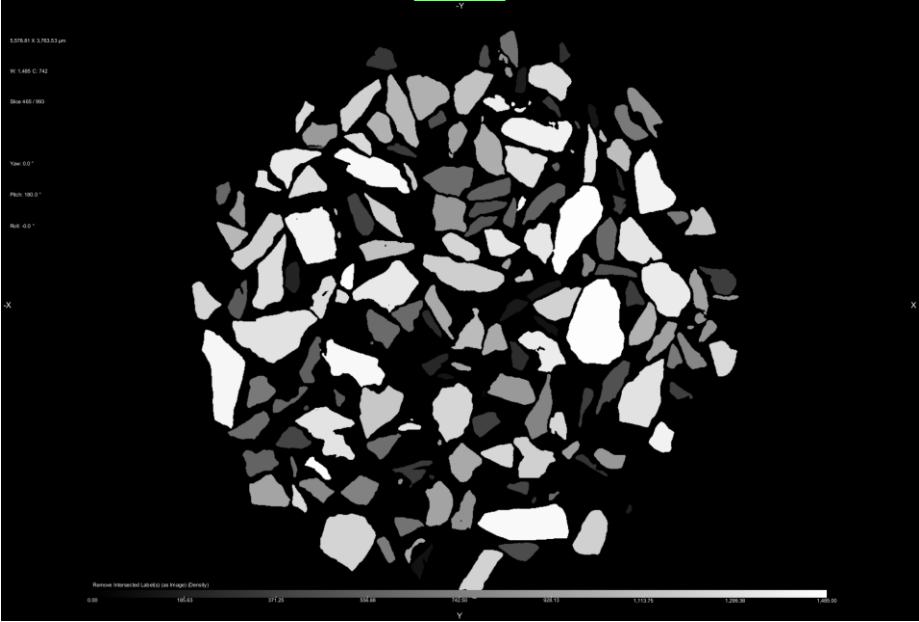
Figure 2. 22: Labeled particles in dragonfly converted to grayscale image and ready to import to the Avizo software

23
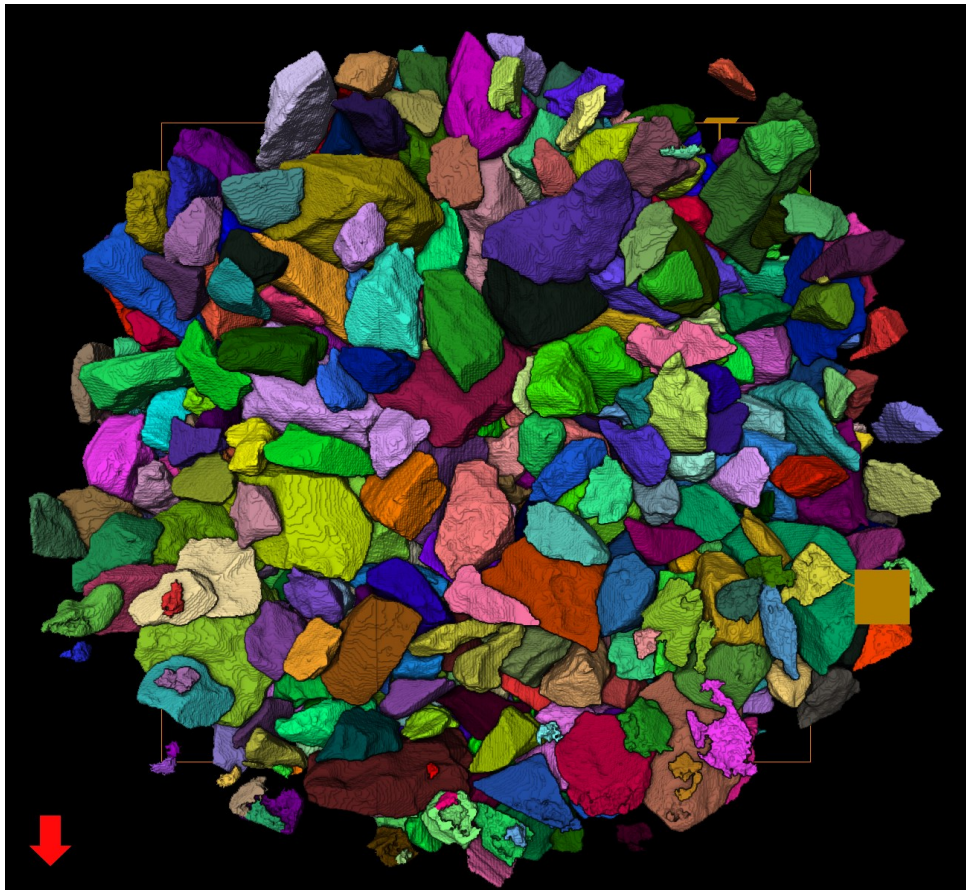
Figure 2. 23: Particles analyzed first view of 3D.
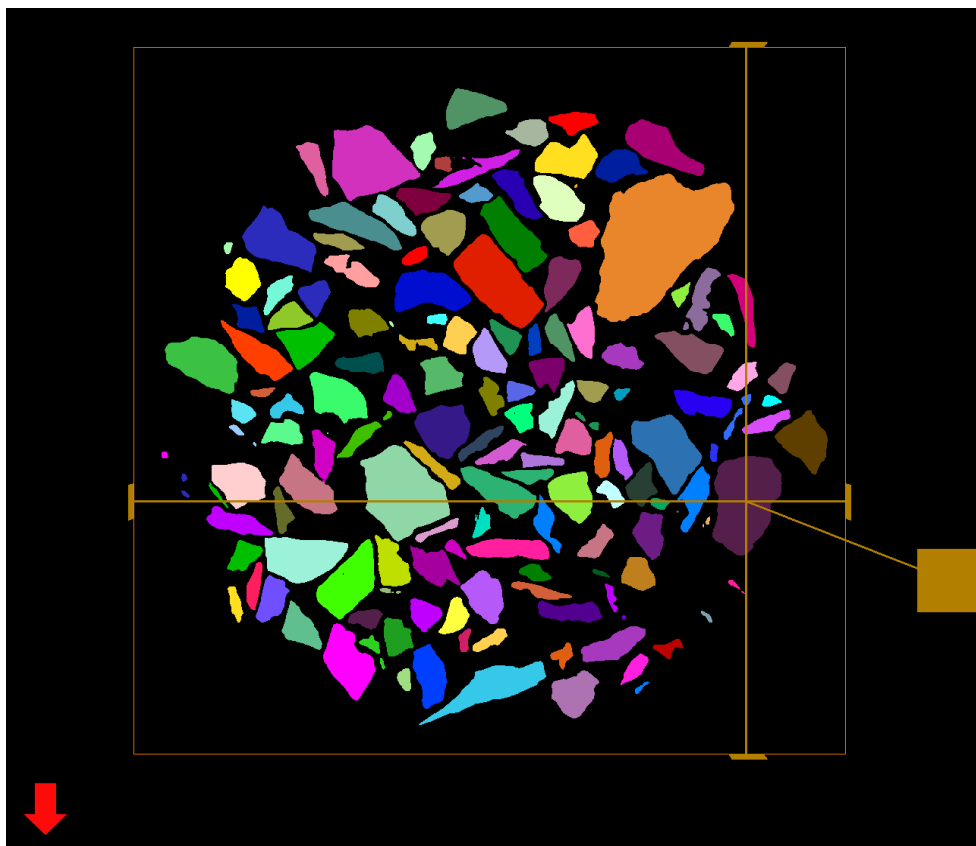
Figure 2. 24: Particles analyzed in 2D and a single particle number 1472 is selected.
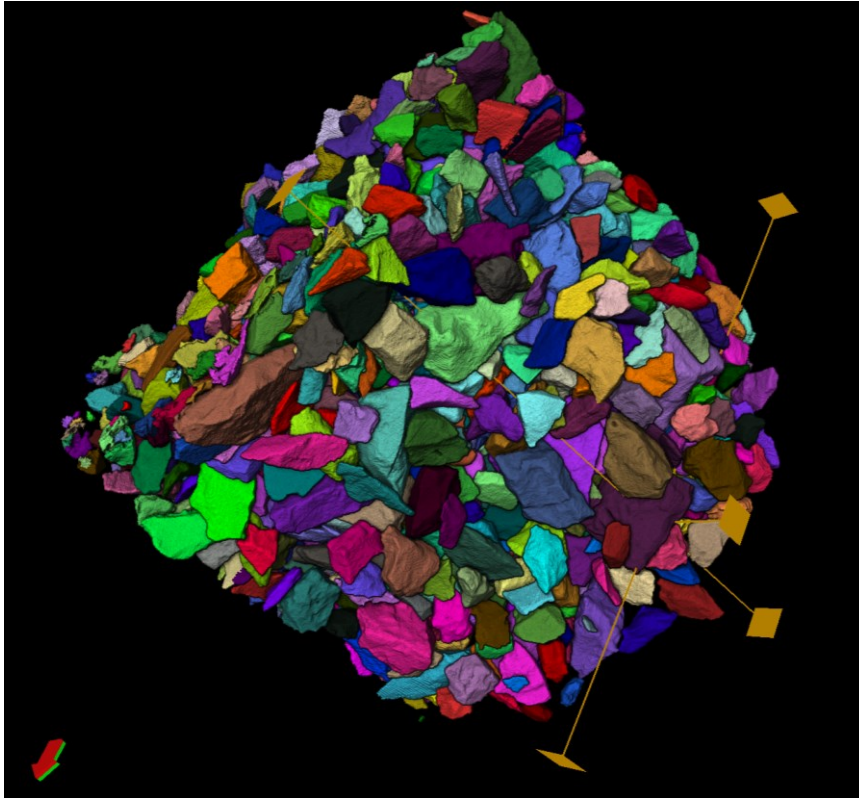
Figure 2. 25: Particles analyzed in 3D and a single particle number 1472 is selected.

Image analysis of individual particles resulted primarily in a number weighted size distribution (counting the number of particles/bin), converted easily to an area – or volume-weighted distribution. The particle distribution can be presented as a bar or line chart (histogram or curve) 2D & 3D particle size analysis of XCT image (Dalen, 2014). The data were exported as CSV file formats to use in R software for the next steps.

2.2. Statistical approach for Particle Size Distribution

In this study, a prediction statistical model was defined by using Bayes' Theorem. In Bayes' Theorem, as an inverse conditional probability, two conditional probability assessments were explored to find a quantitative relationship between them (Clementi et al., 2011). The main goal of the prediction model was to construct a probability distribution of the 3D size of individual particles from the information of their 2D cuts and the bulk particle size distribution, because the methods to measure them exhibit less complexity and less cost than a full 3D XCT. The statistical model required input data as input to predict the 3D size distribution of particles from the two-dimension size distribution; these input data for the model, corresponding to the different analytical methods, were divided into three parts depending on their roles in the model: prior, likelihood and posterior. Table 2.6 shows the model parts and analytical techniques required for it.

Table 2. 6: Statistical model parts and analytical techniques requirements

Model parts	Required Analytical technique
Prior	Laser diffraction or sieving
Likelihood	XCT (2D)
Posterior	XCT 3D

2.2.1. Bayes' theorem and particles size distribution

The unique value of the Bayesian approach is to estimate the posterior probability distributions for all the unknown objects in a model, given the data sample. To use the model, marginal distributions are constructed for all those entities we interested in, i.e., the study end variables (Lampinen and Vehtari, 2001). These can be the parameters in parametric models or the predictions in (non-parametric) regression or classification tasks. The posterior probabilities require a clear definition of the prior probabilities for the parameters. The posterior probability for the parameters θ in a model H given the data D is, according to the Bayes' rule,

$$P\left(\theta \mid D, H\right) = \frac{P\left(D \mid \theta, H\right) \cdot P\left(\theta \mid H\right)}{P\left(D \mid H\right)} \tag{2-1}$$

where $p\left(\theta \mid D, H\right)$ is the likelihood of the parameters θ, $p\left(\theta \mid H\right)$ is the prior probability of θ, and $p\left(D \mid H\right)$ is a normalizing constant, called evidence of the model H. In this study, the prior probability is identified with p (3D) and the likelihood with p (2D $\mid$ 3D), that denotes the probability of obtaining each possible 2D value given its actual 3D size , and for each individual particle. p (2D) is the normalizing constant, interpreted as the evidence of the model, which is the marginal probability distribution of two-dimensional cuts of individual particles. Therefore in this study, the Theorem is written as below:

$$p\left(3D \mid 2D\right) = \frac{p\left(2D \mid 3D\right) \cdot p\left(3D\right)}{p\left(2D\right)} \tag{2-2}$$

The normalizing constant p (2D) needs to add at the end of calculations, so for now, we can remove it and write the Theorem as:

$$P\left(3D \mid 2D\right) \alpha\ P\left(2D \mid 3D\right) . P\left(3D\right) \tag{2-3}$$

It is important to note that the particle size distribution from our analytical methods to be used in Eq. (2-3) must be defined on the same system base. For instance, image base techniques such as XCT produce number distribution of particles, while LD reports volume (mass) distribution. Therefore, it is necessary to convert LD data to number distribution before using them in Eq. (2-3).

2.2.2. Prior

In Bayes theorem, a prior probability of the target parameter is a probability distribution that would express one's beliefs about this quantity before some evidence is taken into account. Prior (p (3D)) data was considered from the information of laser diffraction as global property (bulk sample population). For evaluating the performance of the proposed method, two possible scenarios for the prior distribution were considered: 1) A prior model for performance and diagnostic purposes (Figure 2.26), and 2) A prior of actual data (Figure 2.27). For the first case, we derived the prior distribution from XCT data, and for the second one, the measurement of the laser diffraction was used, previously converted to number distribution. Furthermore, the prior obtained from LD was constrained to the particle size range that could derive from XCT.

2.2.3. Likelihood

The likelihood of a hypothesis given some data is the probability of the data assuming that the hypothesis is true. In Bayes' Theorem, likelihood results are used to update prior information. In this study, the likelihood function defines a probability distribution of the 2D size distribution given a 3D size value. This is denoted as p (2D $\mid$ 3D). The 2D of a particle can be measured by several analytical instruments, most importantly from MLA and other automated mineralogy systems based on scanning electron microscope technoloy. Additionally, we can emulate the obtention of such 2D cuts from the XCT data results. One way or another, the value of the 2D cut is observed, that is, it is known. However, for deriving the likelihood p (2D $\mid$ 3D), a reasonable assumption about the *shape* of the particle is needed. In this regard, several strategies can be applied to evaluate the likelihood. In this study, a geometric approach was followed, with the simplification of considering spherical particles, as Figure 2.28.
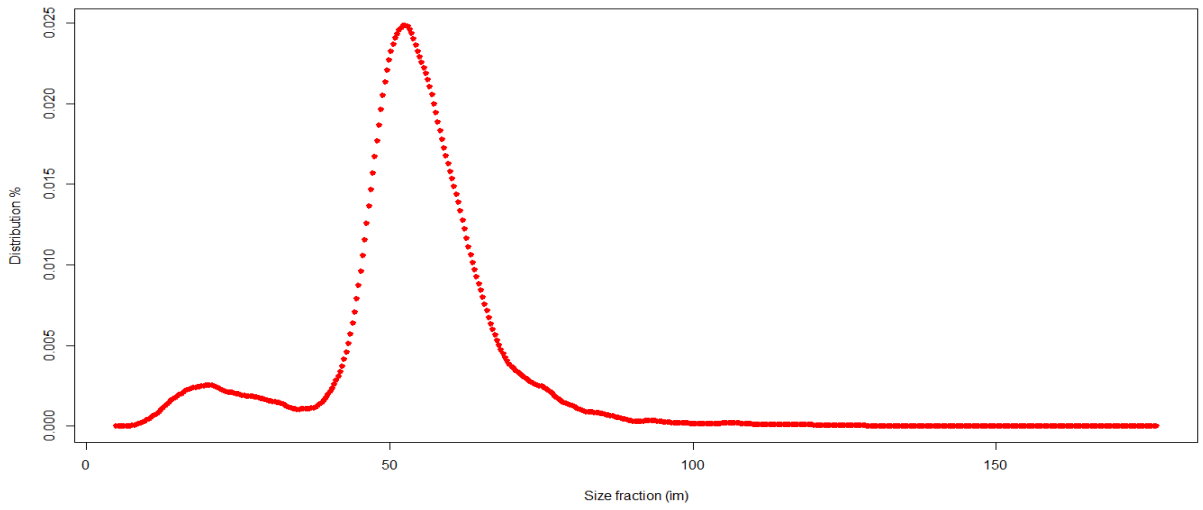
(a)
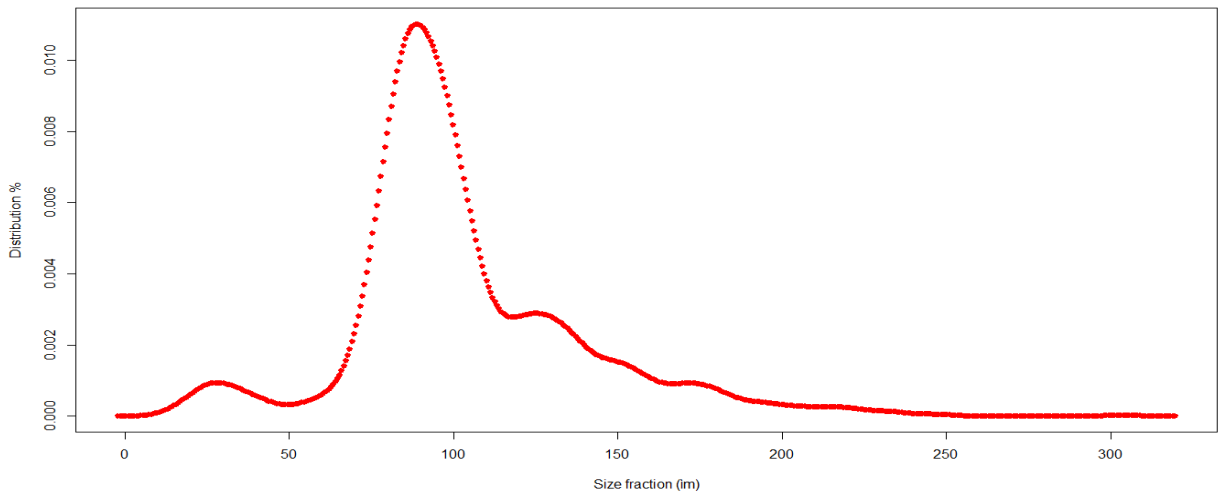
(b)
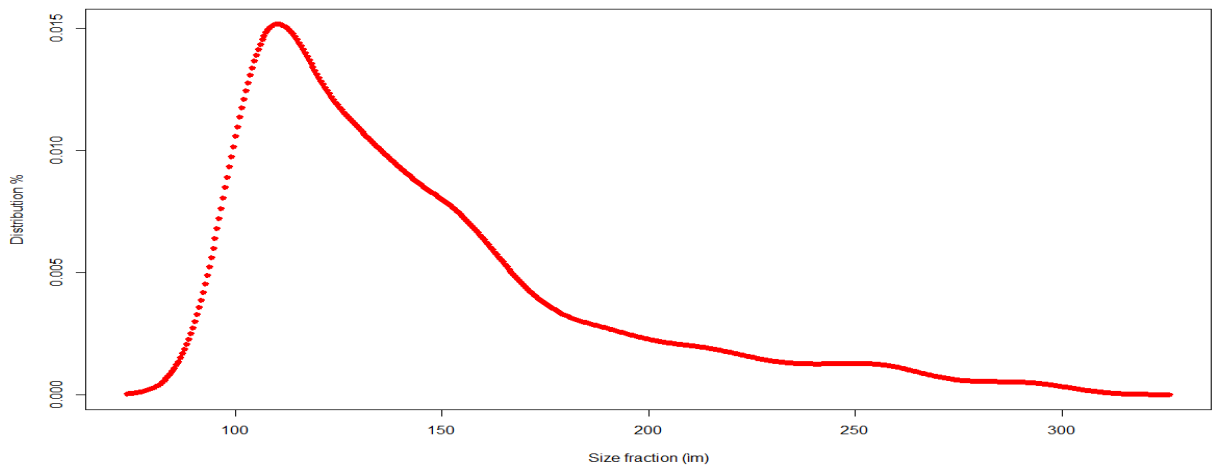
(c)

Figure 2. 26: Priors of model performance and diagnostic settings for minerals (a) quartz fine, (b) quartz lump, and (c) apatite

28
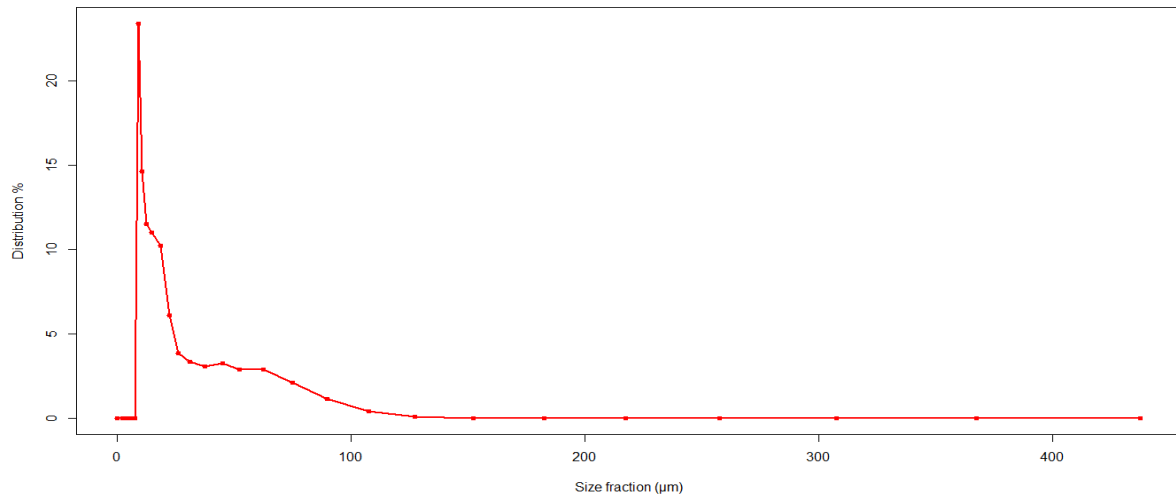
(a)
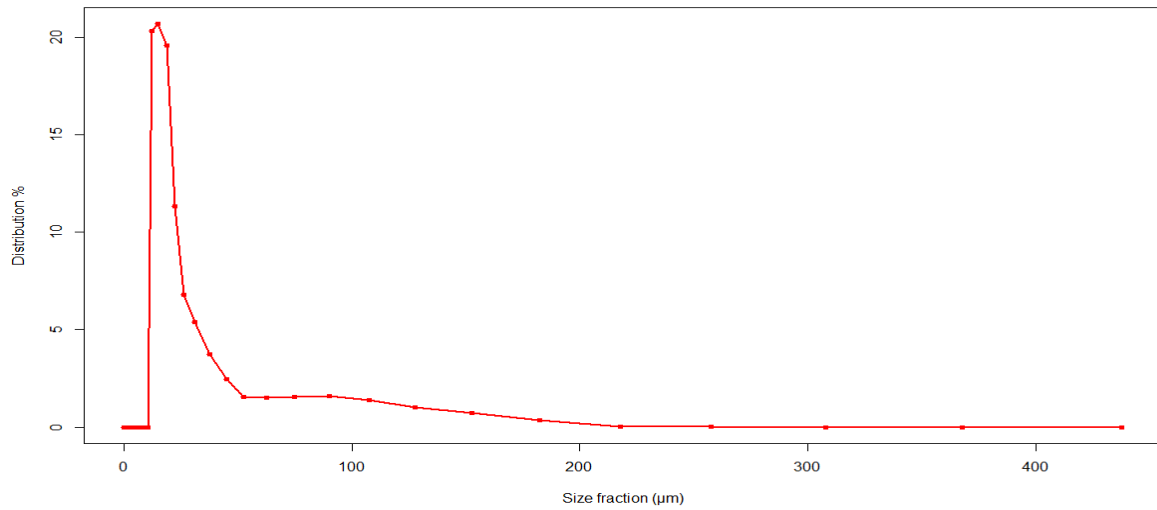
(b)
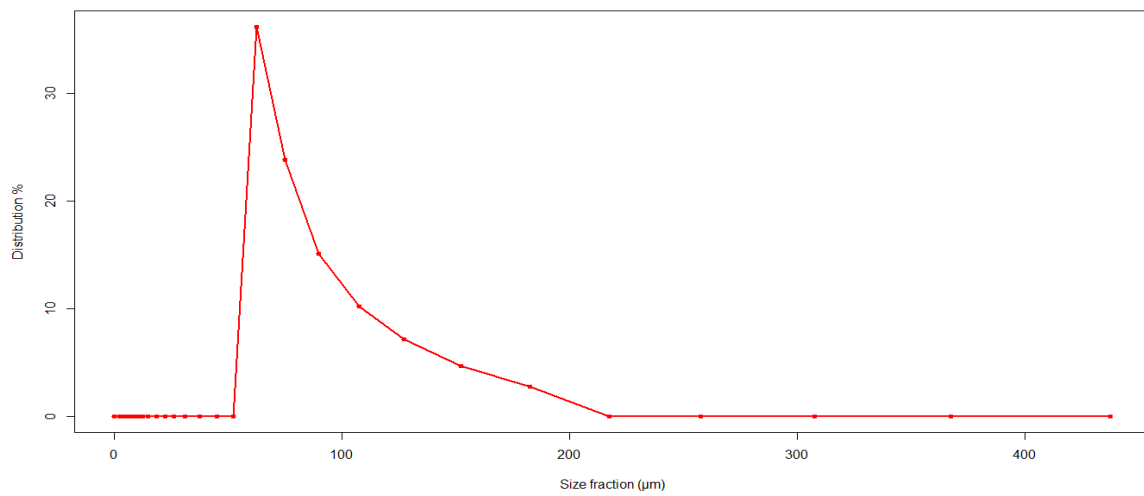
(c)

Figure 2. 27: Priors of actual data from LD data for minerals (a) quartz fine, (b) quartz lump,

and (c) apatite

Figure 2.28 (b) shows the relationship between the 2D size (denoted as r, apparent radius of the particle), and its actual 3D size (denoted as R). Furthermore a denotes the position of the 2D measurement cut through that single particle. This value is unknown; nevertheless, its probability distribution is known. As the cut is randomly distributed, its probability distribution can be reasonably assumed to be uniform between 0 and R. So by the probability theory notation can write this assumption as $\sim U(0, R)$, and its probability density function $f_a(a|R)$ as Eq. (2-4) and its cumulative density function $F_a(a|R)$ as Eq.(2-5).

(a)   (b)
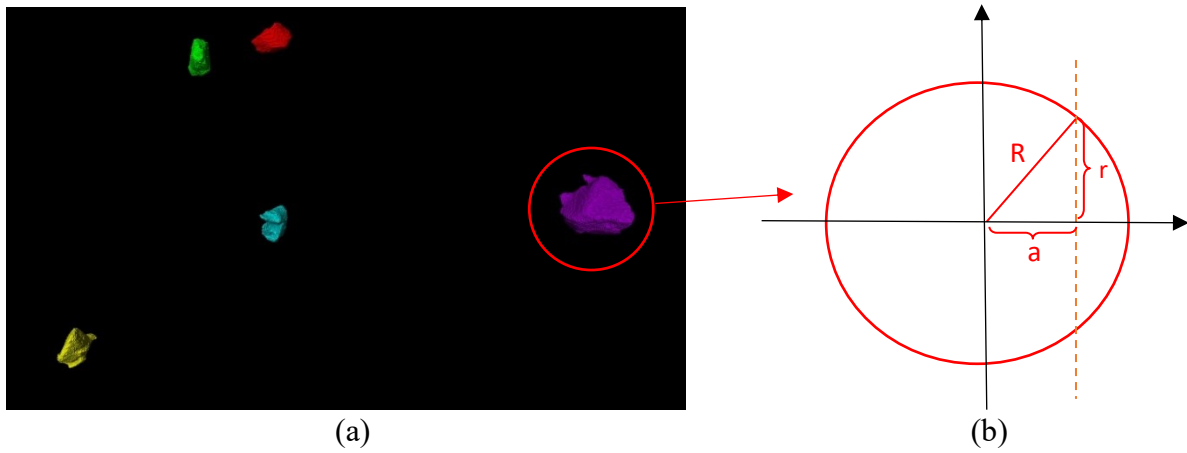
Figure 2. 28: (a) a group of particles of quartz lump, and (b) one particle is selected to show the geometric approach

$$f_a(a|R) = \begin{cases} 1/R & \text{if } 0 \leq a \leq R \\ 0 & \text{otherwise} \end{cases} \tag{2-4}$$

$$F_a(a|R) = \begin{cases} \dfrac{a}{R} & if\ 0 \leq a \leq R \\ 1 & a > R \\ 0 & otherwise \end{cases} \tag{2-5}$$

From figure 2.28, we know:

$$R^2 = a^2 + b^2$$
$$a = \sqrt{R^2 - r^2} \tag{2-6}$$
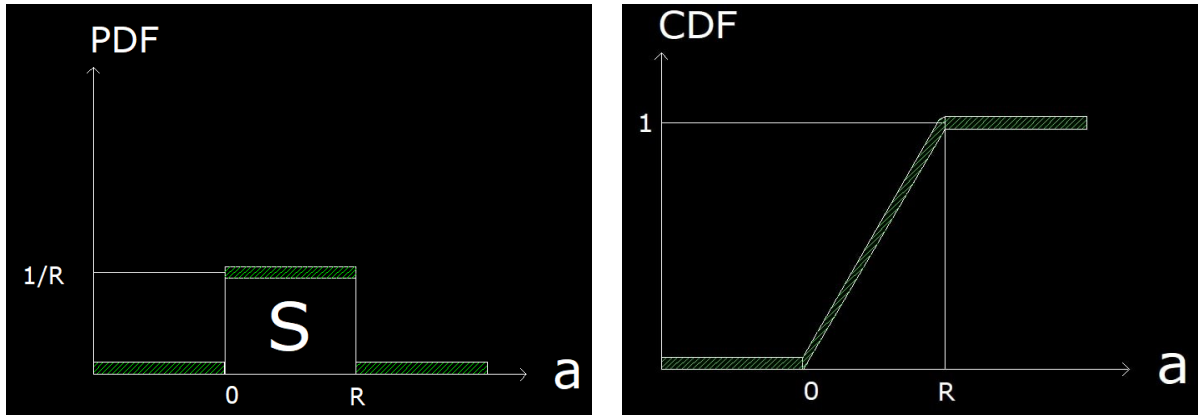
Figure 2. 29: (a) probability density function of uniform distribution and (b) cumulative density function of uniform distribution.

By using Eq. (2-5) and (2-6) can write:

$$F_a(a|R) = \begin{cases} 0 & if\ \sqrt{R^2 - r^2}\ <\ 0 \\ 1 & if\ R\ <\ \sqrt{R^2 - r^2} \\ \dfrac{\sqrt{R^2\ -\ r^2}}{R} & if\ \ 0\ <\ \sqrt{R^2 - r^2}\ <\ R \end{cases} \tag{2-7}$$

The three conditions of Eq. (2-7) can be simplified as below:

$I.$ $\sqrt{R^2 - r^2} < 0$ $R^2 - r^2 < 0^2$ $R^2 < r^2$ (impossible)

$II.$ $\sqrt{R^2 - r^2} > R$ $R^2 - r^2 > R^2$ $0 = R^2 - R^2 > r^2$ (irrelevant)

$$\tag{2-8}$$

$III.$ $0 < \sqrt{R^2 - r^2} < R$ $0 < R^2 - r^2 < R^2$ $-R^2 < -r^2 < R^2$ $R > r > 0$

So from equation (2-8) can be written as (2-9) below:

$$
F_a(r|R) = \begin{cases} 0 & if\ R < 0 \\ \dfrac{\sqrt{R^2 - r^2}}{R} & if\ r < R \end{cases}
\tag{2-9}
$$

To convert CDF to the PDF derivation performed on equation (2-9):

$$
f_a(r|R) = \frac{dF\ (r\ |\ R)}{dr} \begin{cases} 0 & if\ R < r \\ \dfrac{\dfrac{r}{R}}{\sqrt{R^2 - r^2}} & if\ r < R \end{cases}
\tag{2-10}
$$

From equation (2-10) the likelihood function is obtained to be introduced in Eq. (2.2). Depending on r, the size of apparent from 2D cuts, the likelihood of its true size R starts from a different point, but the curves are similar by a translation and a scaling on the x-axis. As it shown by the curves, the likelihood function is infinity at $R = r$.
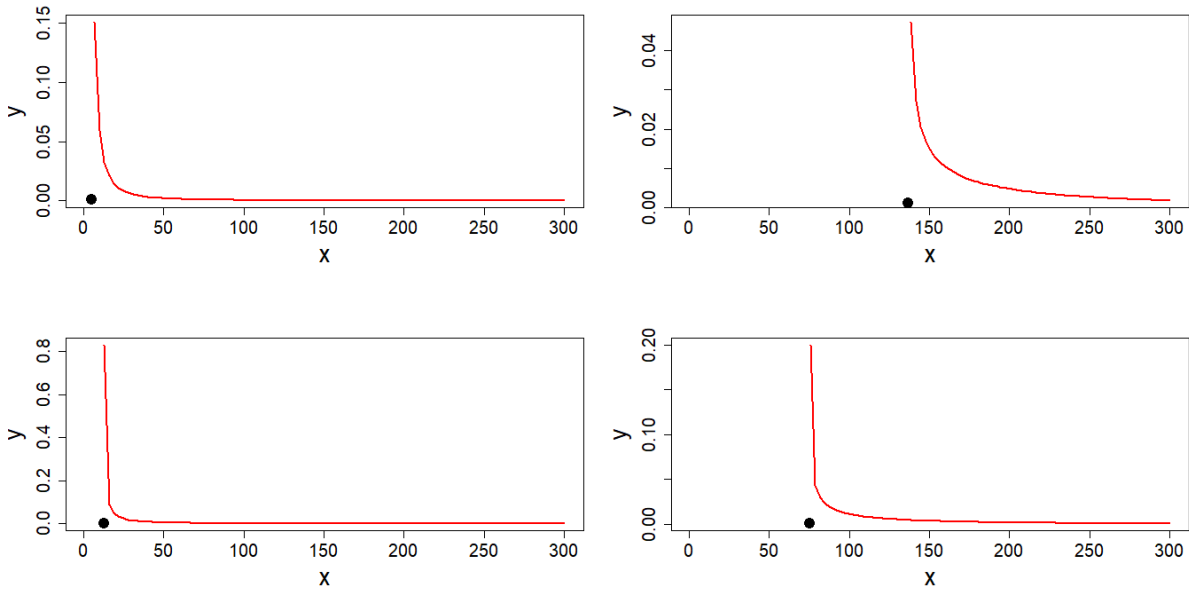
Figure 2. 30: Likelihood curves with different particle cuts; cut sizes are 5, 137, 13, and 76, respectively

2.2.4. Posterior

In Bayesian statistics, a posterior probability is the revised or updated probability of an event occurring after considering new information. In other words, by multiplying likelihood and prior probabilities distributions, the result is (proportional to) the posterior distribution. Using

equation (2-10) with the results of the prior distribution as explained in section (2.2.2), which is represented by means of a specific discretization of the bulk sample number-based particle size distribution, the posterior probability density function p (3D $|$ 2D) was obtained. Figure 2.31 shows as an illustration one case of prior, likelihood and posterior for one single particle of apparent size $r = 4$.

(a)

(b)

PDF of Posterior Curve
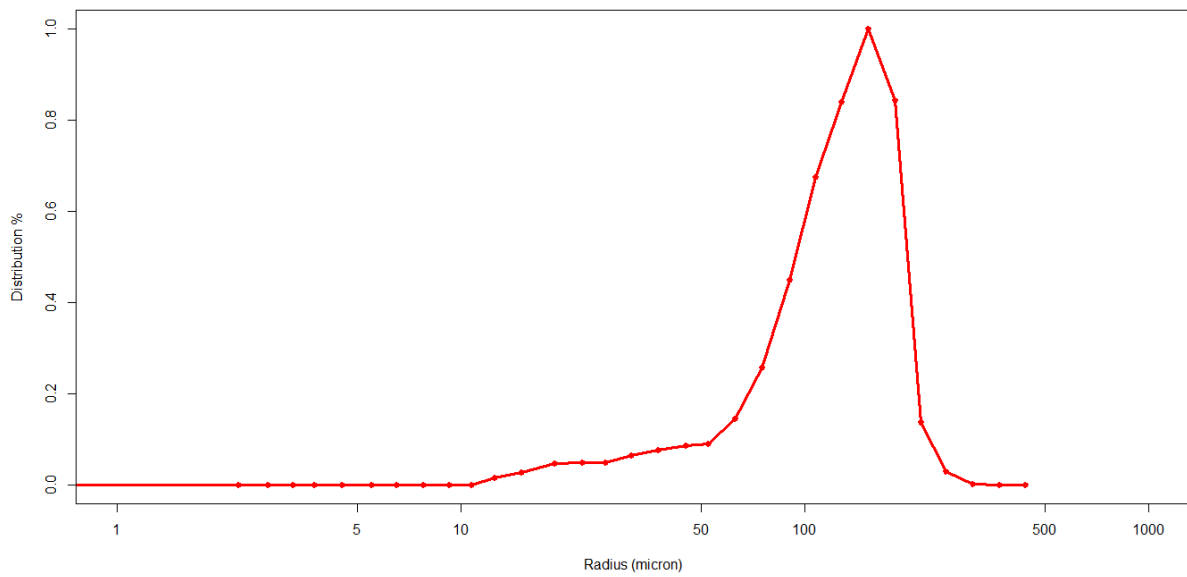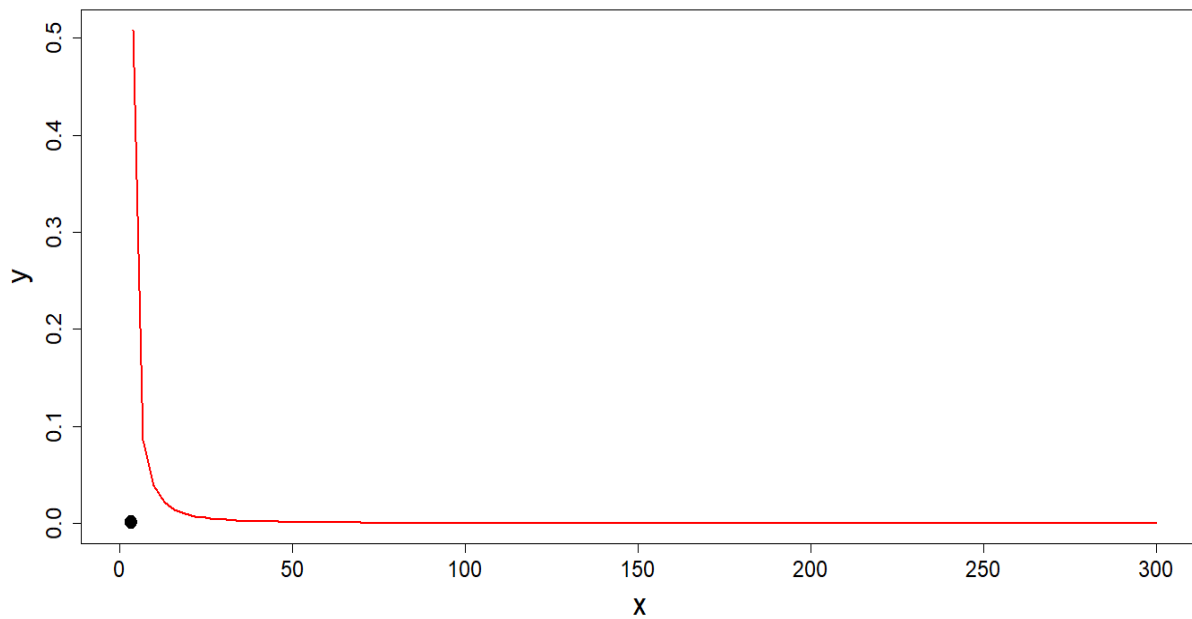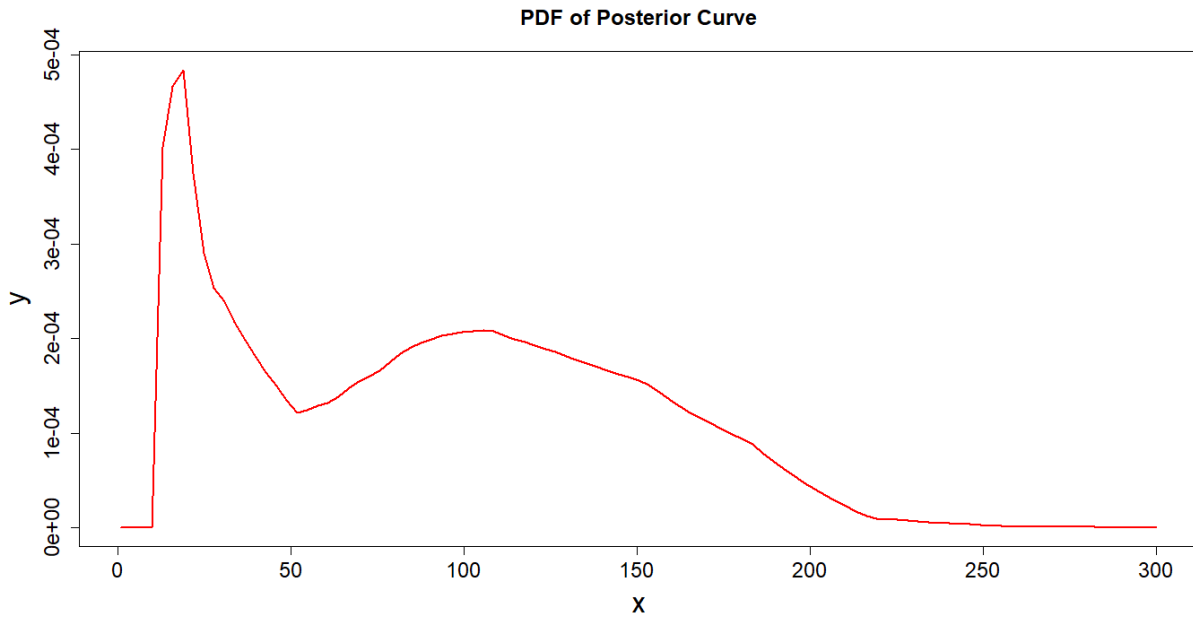
(c)

Figure 2. 31: (a) prior curve sample (b) likelihood curve with a 2D cut size 4 micron, and (c) posterior curve after multiplication

2.2.5. Validating posterior result for single particles

After obtaining the curve of the posterior, as in figure 2.31 (c), the method requires validation to check that it provides reasonable assessments of the true size R of each particle, and to assess the uncertainty of this quantity. Therefore, the actual particle size was extracted from the same XCT measurement is also shown on Figure 2.32 as a vertical line. Figure 2.32 (a) displays the actual 3D size of a particle on the curve. As can be seen, the particle's actual 3D size, with a size of 25 microns, is very close to its cut size from 2D data. Closer the actual 3D size is to the peak of the posterior curve, the more similar the true and apparent sizes are. For quantifying that similarity, we can calculate the integral of the curve from the place of the actual 3D size (green line) upwards (figure 2.32 (b)) and normalize it to the whole area of the curve as equation (2-11). The normalizing constant in Eq (2-2) can be ignored, because the normalization is taking place in Eq. (2-11). As much as $Q(R)$ is closer to 1 the true and the apparent size are more similar.
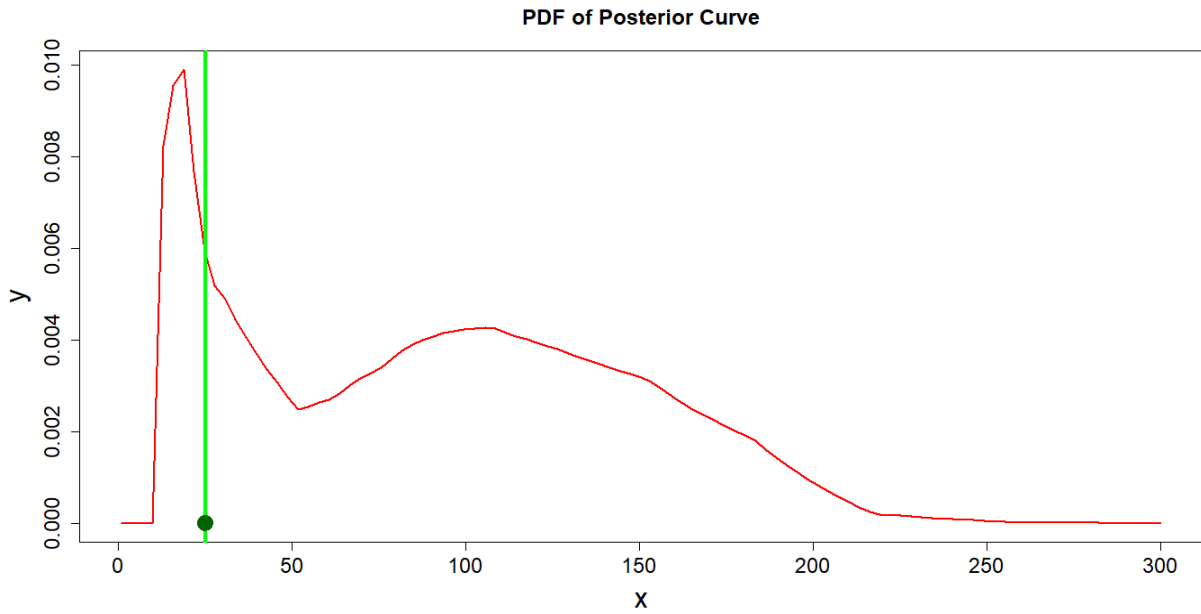
(a)
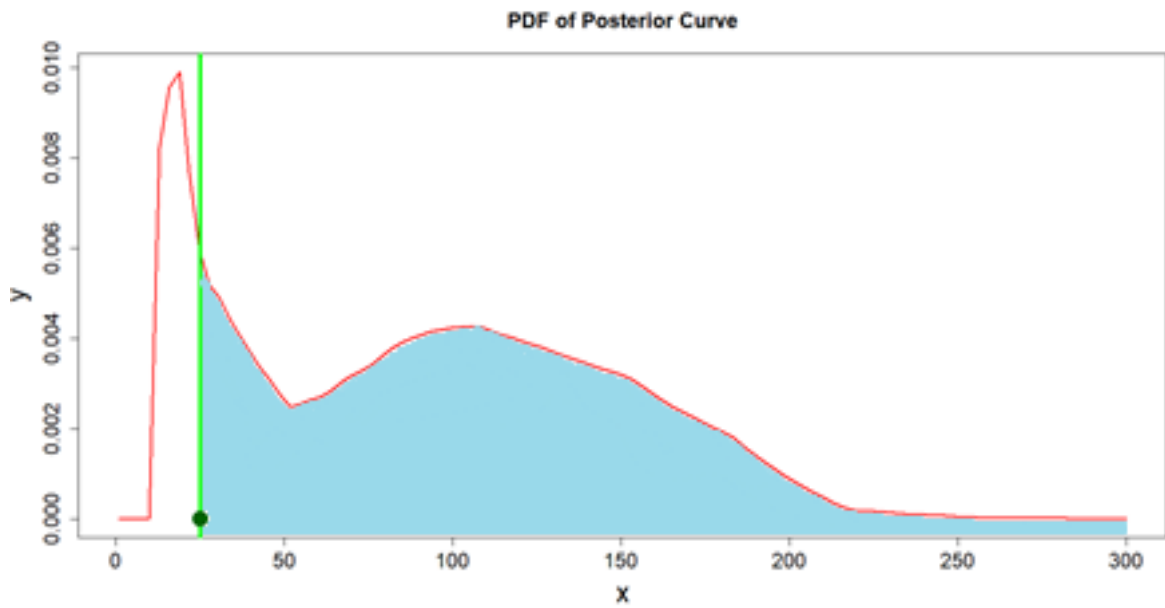
(b)

Figure 2. 32: (a) and (b) show what the posterior curve area from the actual 3D point looks like.

$$Q(R) = \frac{\int_R^\infty p(R|r)dR}{\int_0^\infty p(R|r)dR} \qquad (2\text{-}11)$$

In this way, results from all particles are made comparable to each other. If the hypotheses we assumed in constructing the model are correct in describing the actual value, then the Q(R) values must follow a uniform distribution, which is flat between zero and one, whichever form the posterior has.

Chapter 3. Model proposal, validation, and diagnostic settings

After clarifying the method and before applying the model to the actual data, a validation, and diagnostic were needed; given the available data two series of analyses were implemented. 1) model proposal, validation, and diagnostic settings and 2) usage in a realistic setting with actual data; by actual data, as it was mentioned in section 2.2.2, meaning the prior distribution derived from laser diffraction as the bulk sample.

3.1. Model Proposal

In this step, 1485 single particles from XCT data of one of the materials (quartz lump) were extracted. Each of these single particles includes several cuts from 2D data. Randomly one cut for each particle was selected. Afterwards, data was used as explained in chapter 2 to construct the model for the uncertainty on the actual 3D size of each particle via the Bayes theorem strategy. 3D data defines the prior distribution, as shown in figure 3.1.
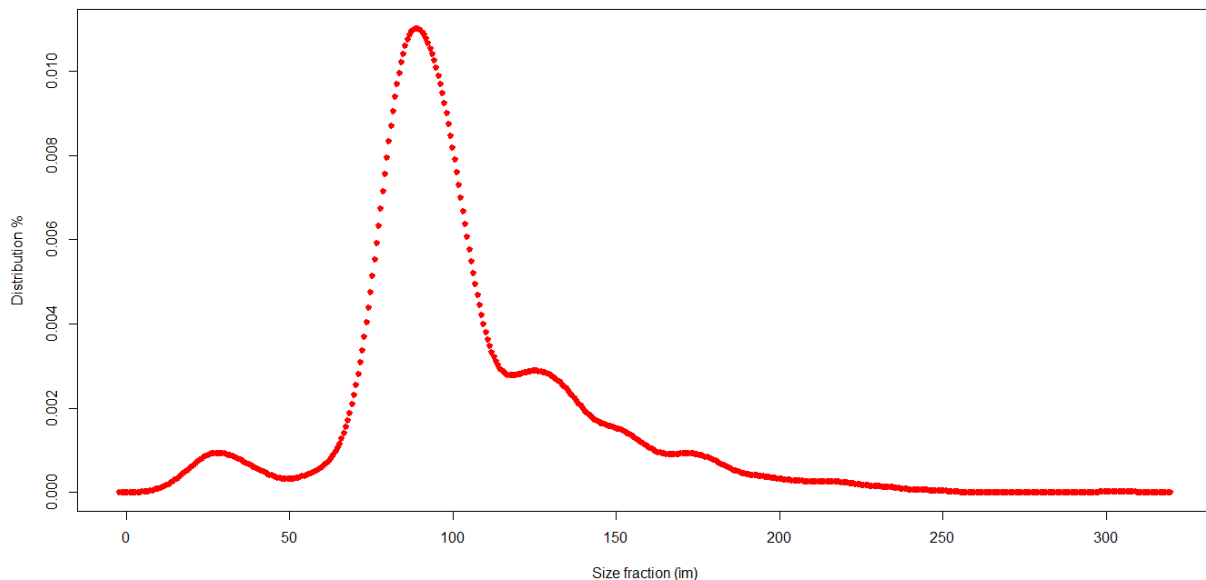
Figure 3. 1: Prior curve from XCT 3D data for mineral quartz lump size of x axis is in micron

The same 3D data was used as prior as was used in validation as actual 3D particle size. Applying this strategy helped to find how the model works, removing potential differences between the way LD and XCT measure the 3D particle size. The likelihood equation curves, depending on the cuts size (2D size), were evaluated with Eq. (2-10). After importing the data,

likelihood and prior curves were multiplied to produce a posterior curve—the actual particle size was placed on posterior curves and represented as a line. The integral $Q(R_i)$ was computed for particle i with true size R_i, and results were represented as histograms in figure 3.2.

Table 3. 1: Summary of Q-values of the histogram

Variable	Summary of Q-values of histogram					
	Min.	1ˢᵗ Qu	Median	Mean	3ʳᵈ Qu	Max
HIST	0	0.1562	0.3343	0.3760	0.5709	1
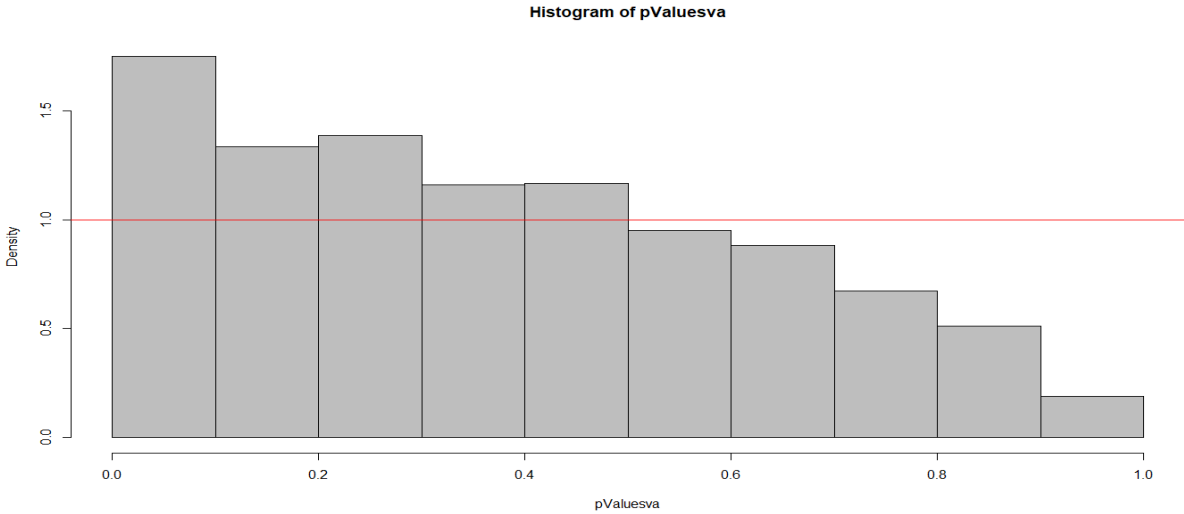
Figure 3. 2: Histogram of Q-values

The histogram was proposed to visualize how well the method works for all particles. As shown in Figure 3.2, the method has deviations from the expected result (a flat line): too low frequency of high Q-values and too high frequency of low and near-zero Q-values are identified, as the expected result should be a flat frequency. To explore the reason of the deviations from the expected behaviour, each posterior was classified as a function of the interval of the histogram they belong to. For each one of these sequences, one representative was extracted at random. These posterior curves are shown in column 2 of Table 3.2. They show the typical shapes of posteriors and under which circumstances high or low Q-values are acquired.

In Table 3.2, the actual particle size is shown by the green line on posterior curves. From sequence 1 to 10, the true size moves closer to the apparent size. This means that in sequence 10, which includes the highest Q-values, the particles tend to be cut through the middle. This is supported by the deviation, the minimum, average and maximum 3D size of all particles in each sequence (columns 4-6, Table 3.2). Furthermore, the exact number of particles in each histogram is presented as well; these numbers correspond to the height of each bar in the

histogram of Figure 3.2. In other words, the histogram is a visualization of the same numbers reported here. The size information in the table shows that particle sizes increase from highest to lowest Q-values. The average size of the cuts in each sequence shows the same trend, but less pronounced. In the following subsections, two different methods are implemented to further analyze the deviations.

3.2. Validation and Diagnostic Settings

The posterior curves are split in several series following different criteria to try to understand in which circumstance the deviations occur. Two cases are considered. One is different cuts for the same sample particles. The second one is to filter particles by their aspect ratio. These two methods and their results are provided in the following subsections.
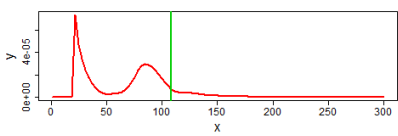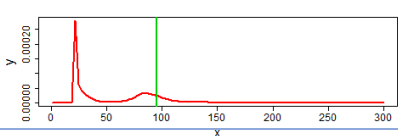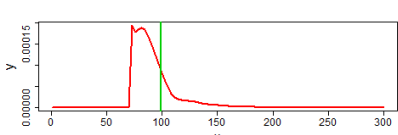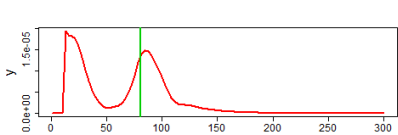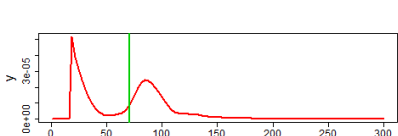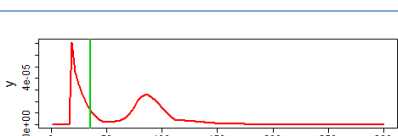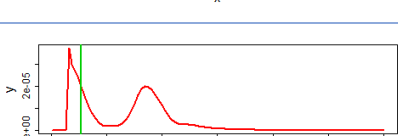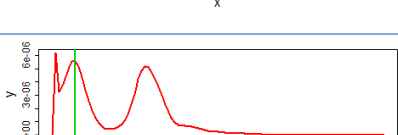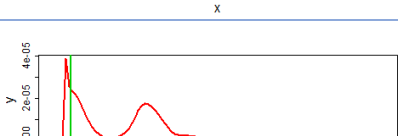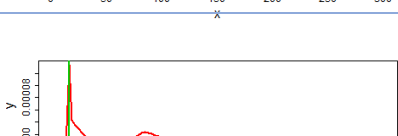
3.2.1. Cut variability

The first experiment is to select different random 2D cuts for each particle. For doing so, 300 particles are randomly sampled from the 1485 single particles from XCT data of quartz lump. For these 300 particles, five different random cuts are selected and are set in five different series. Following the same scheme as for the general case, all the model proposal procedures are applied to the five different random cuts separately. One prior curve for different random cuts and five histograms are presented in Figures 3.3 and 3.4, respectively.
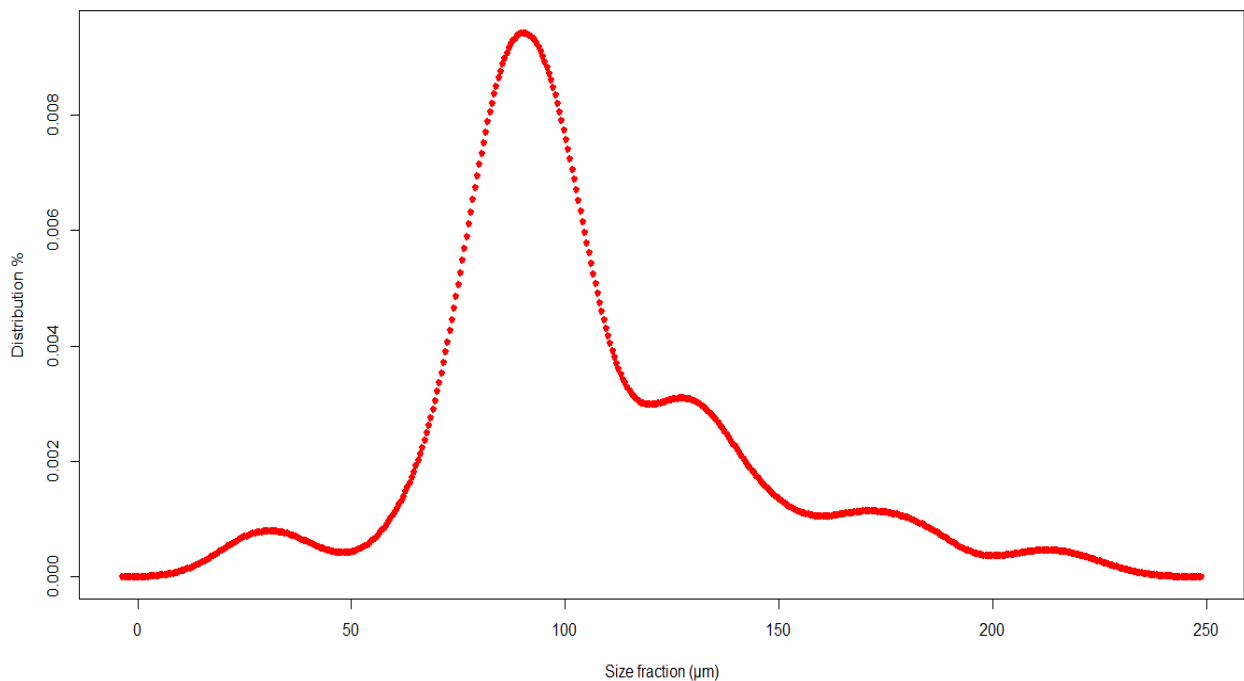
Figure 3. 3: Prior distribution for different random cuts

Table 3. 2: Examples of posterior curves and particles information in each sequence

Seq No.	Posterior's curve of each sequence	Number of 3D particles	Actual 3D particle size - (R)			2D cuts size (r)
			Min	Mean	Max	Mean
Seq 1		253	105.062	148.418	247.467	69.680
Seq 2		197	93.65	114.912	232.132	68.162
Seq 3		204	86.911	104.314	204.315	67.692
Seq 4		169	80.257	97.385	186.810	64.422
Seq 5		169	70.4705	95.435	227.672	68.833
Seq 6		141	31.138	84.845	182.709	59.093
Seq 7		127	25.33235	78.413	157.669	59.891
Seq 8		97	21.31805	72.413	144.899	58.598
Seq 9		73	13.75745	66.774	210.194	57.476
Seq 10		28	16.148	83.027	217.843	80.562

The five histograms (Figure 3.4) show possible outcomes for the same method and for the same particle population, but for a different sample. Differences between them are therefore only due to the randomness of sampling. There is always variability in the data. From the results of histograms we can see how the variability in the data propagates to variabilities in the results of the method. Again, one element of each bar is extracted to see why frequencies are different. In Tables 3.3 and 3.4, the details and summary Q-values and curves extracted from histograms and sequences numbers as the elements of each histogram bar are shown. The histograms and tables of Q-values demonstrate that the randomness of 2D cuts for the same particle does not have pronounced effects on the results of posteriors. The same behaviour as observed in the previous general case can be seen here as well: the effect of particle sizes from sequence one to ten is notable in the Tables 3.4 and 3.5.

Table 3. 3: Individual Q-values of individual cases

Summary Q-values of posterior distribution of histogram Fig 3.4										
Hist No.	Seq 1	Seq 2	Seq 3	Seq 4	Seq 5	Seq 6	Seq 7	Seq 8	Seq 9	Seq 10
1	9	19	25	40	44	58	66	77	84	94
2	9	19	29	39	46	59	66	74	90	92
3	9	19	29	33	46	59	63	76	83	91
4	7	20	27	39	44	53	69	74	81	91
5	8	19	30	39	49	60	68	71	83	91

Table 3.5 shows the size of the actual particle and the size of the 2D cut in each sequence of each variable (histogram), in columns four and five. Also, images of particles are grouped by sequences for a better visualisation and are shown from Figures 3.5 to 3.14. From the posterior's curves of each bar give hints to the reason for the observed differences, e.g., at sequence 10 representing bar number ten in all histograms. In sequence 10, the size of the actual particles is very close to the size of 2D cuts of particles; this means that the probability of cutting particles from their centre is lower than specified by the assumption of random cut and mostly happens in smaller particles. On the other hand, particles from the first bar show larger actual size than the rest, so they have a higher chance of having more cuts in different places than smaller particles.
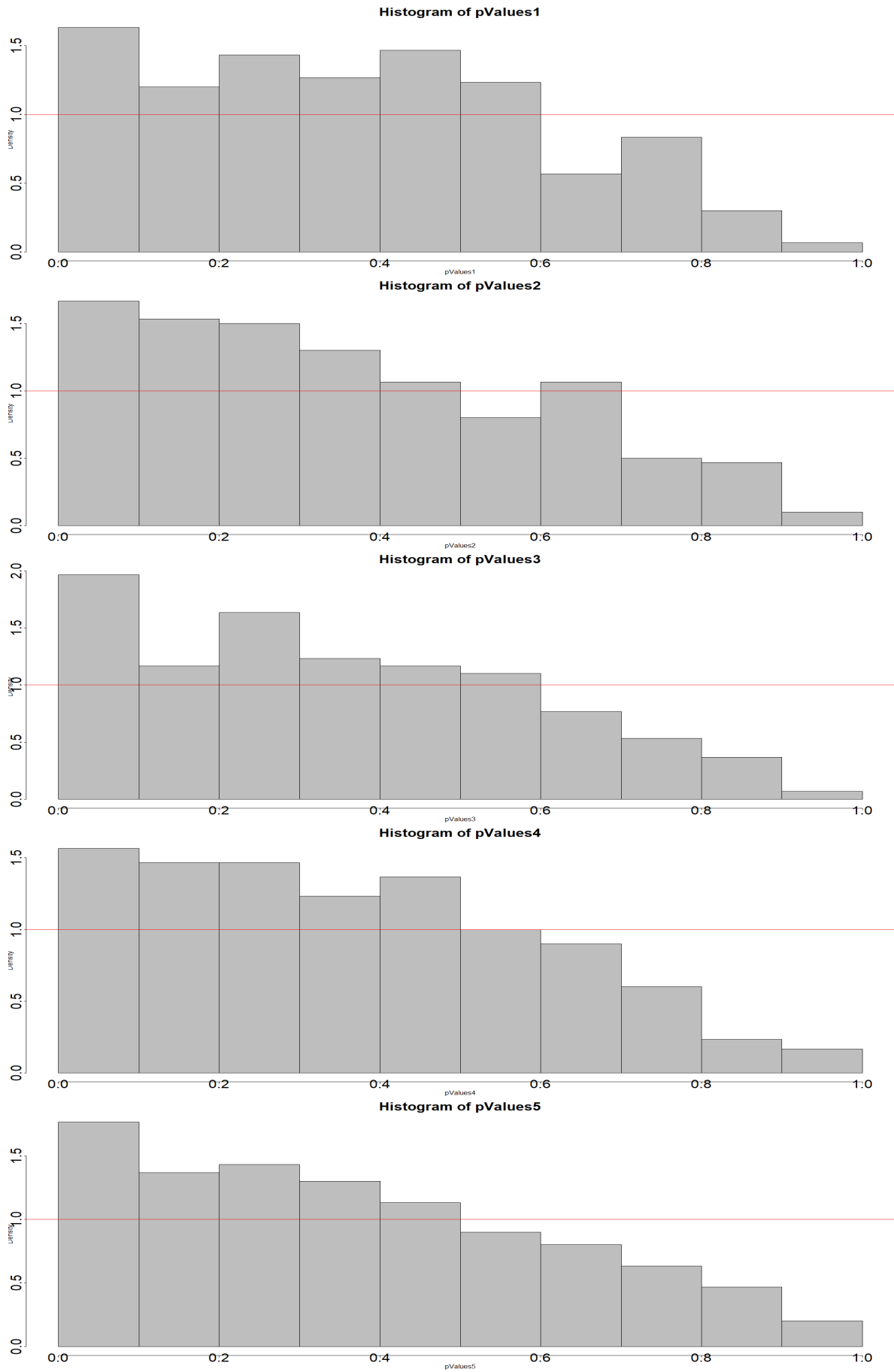
Figure 3. 4: Histograms of five variables

Table 3. 4: Posterior curves extracted from five variables and divided by each sequence.

	HIST 1	HIST 2	HIST 3	HIST 4	HIST 5
Seq 1					
Seq 2					
Seq 3					
Seq 4					
Seq 5					
Seq 6					
Seq 7					
Seq 8					
Seq 9					
Seq 10					
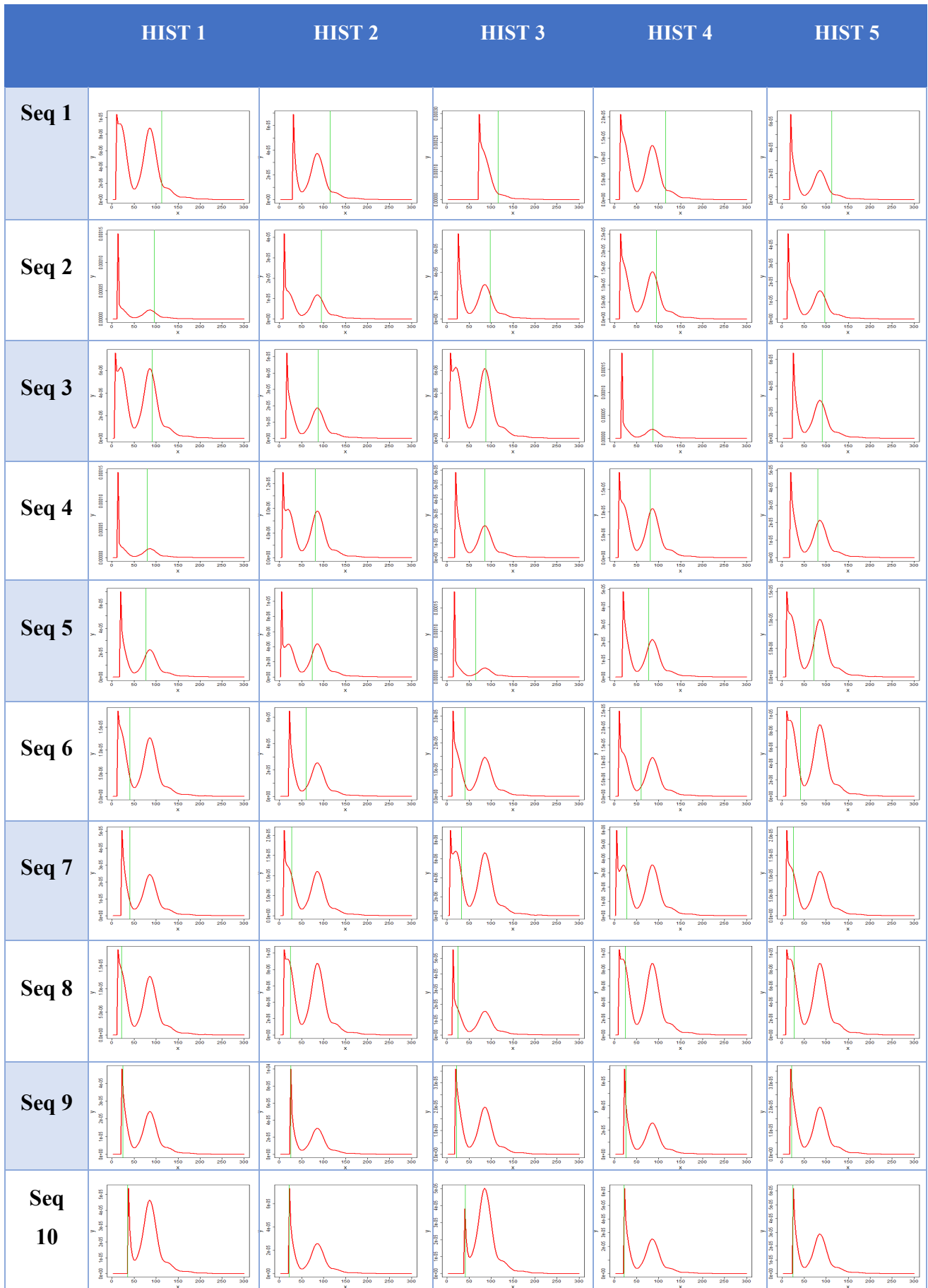
Table 3. 5: Particles information of each sequence of five variables (histograms)

Detail information of particles of each sequnce of each histogram					
Seq No.	**Figure no.**	**Particles label color**	**Particle actual size (3D)**	**Partricle cut size (2D)**	**Histogram number**
Seq 1	Fig 1	Green	226,439	14,316	1
		Violet	229,396	57,858	2
		Yellow	230,714	142,864	3
		Yellow	230,714	21,474	4
		Green	226,439	35,790	5
Seq 2	Fig 2	Green	192,262	25,809	1
		Violet	190,568	19,384	2
		Red	195,522	46,573	3
		Yellow	190,528	22,636	4
		Light blue	193,482	24,796	5
Seq 3	Fig 3	Light Blue	182,515	10,123	1
		Green	176,548	30,086	2
		Red	175,556	10,123	3
		Violet	173,635	31,744	4
		Yellow	180,854	45,834	5
Seq 4	Fig 4	Green	160,185	25,809	1
		Yellow	162,755	12,398	2
		Red	170,894	35,310	3
		Violet	160,996	17,533	4
		Yellow	162,755	34,329	5
Seq 5	Fig 5	Red	154,658	36,028	1
		Green	147,476	7,158	2
		Violet	130,081	31,744	3

		Red	154,658	34,329	4
		Yellow	144,531	16,531	5
Seq 6	Fig 6	Green	80,488	20,663	1
		Red	120,289	40,702	2
		Violet	80,488	23,740	3
		Yellow	119,881	18,482	4
		Green	83,1961	14,316	5
Seq 7	Fig 7	Red	80,57	38,988	1
		Green	55,029	18,014	2
		Yellow	64,599	10,934	3
		Green	55,029	5,844	4
		Violet	50,664	18,014	5
Seq 8	Fig 8	Violet	42,636	20,663	1
		Green	47,718	14,316	2
		Green	47,7185	25,138	3
		Green	47,7185	14,316	4
		Violet	53,804	14,316	5
Seq 9	Fig 9	Yellow	47,718	38,547	1
		Green	50,664	48,018	2
		Violet	42,636	32,012	3
		Green	50,664	41,120	4
		Violet	42,636	32,012	5
Seq10	Fig 10	Green	71,195	69,523	1
		Light blue	42,636	41,327	2
		Red	83,196	74,044	3
		Light blue	42,636	40,492	4
		Blue	47,718	45,460	5
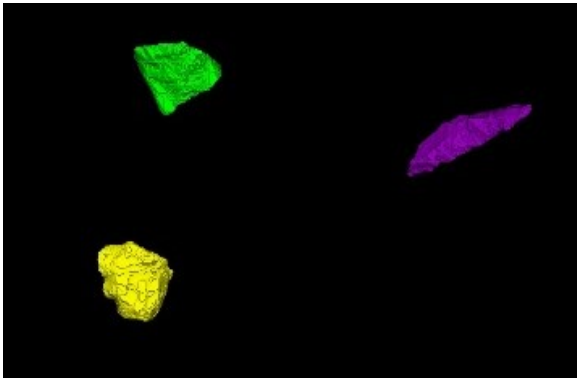
Figure 3. 5: Particles of seq 1
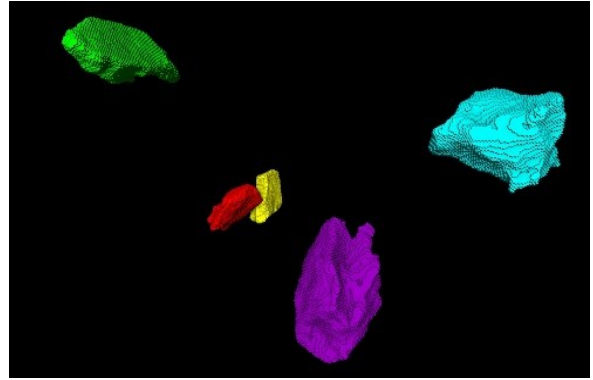
Figure 3. 6: Particles of seq 2
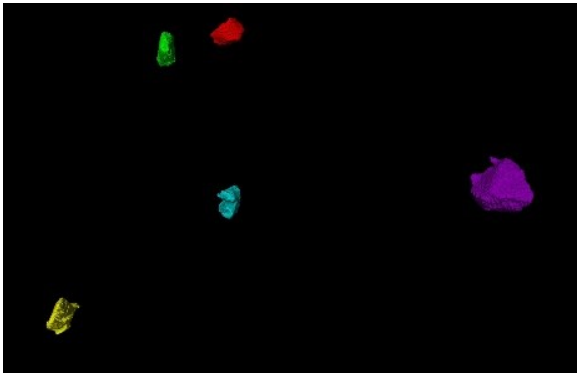
Figure 3. 7: Particles of seq 3
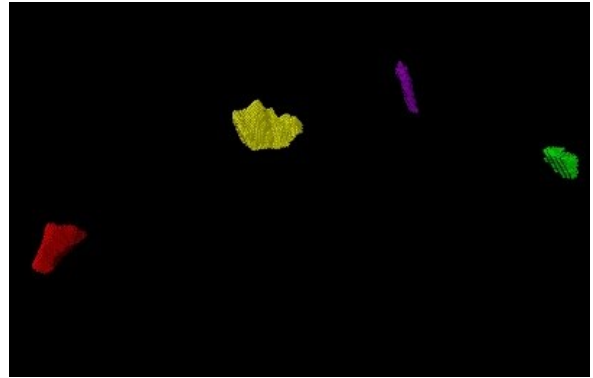
Figure 3. 8: Particles of seq 4
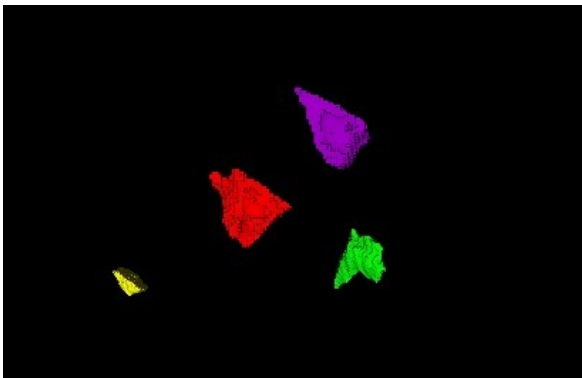
Figure 3. 9: Particles of seq 5
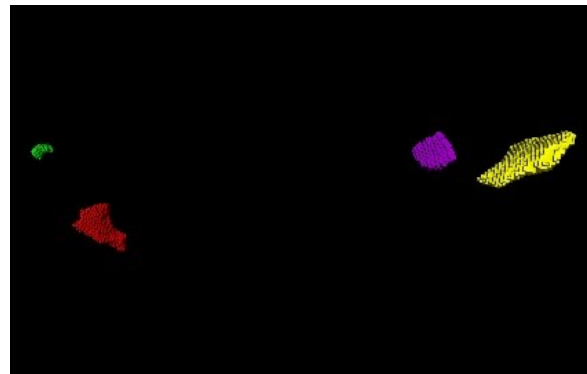
Figure3. 10: Particles of seq 6
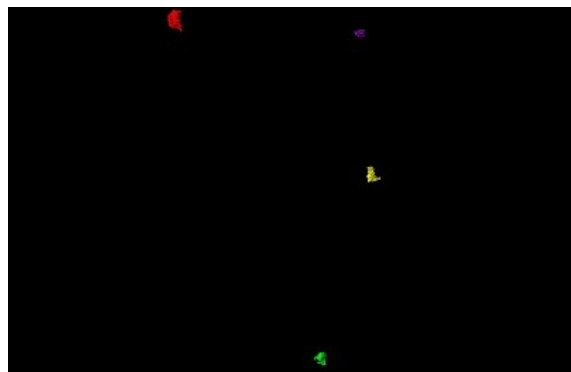
Figure 3. 11: Particles of seq 7

45
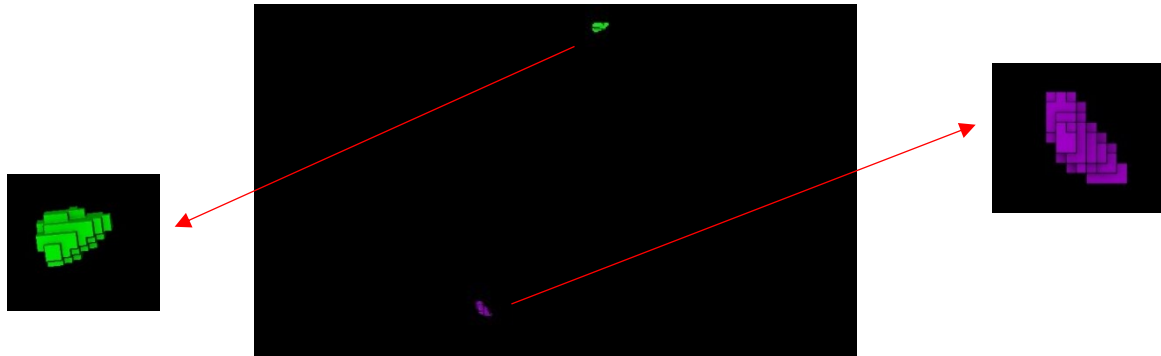
Figure 3. 12: Particles of seq 8
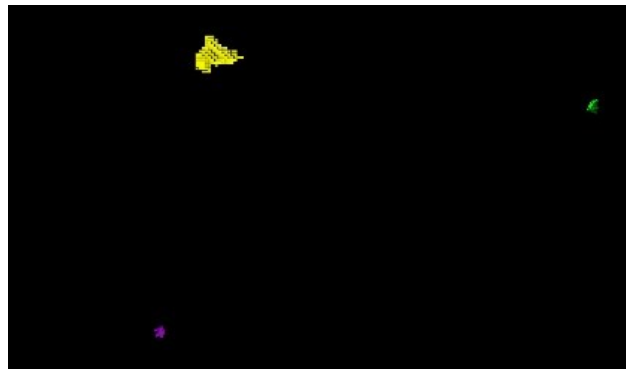
Figure 3. 13: Particles of seq 9
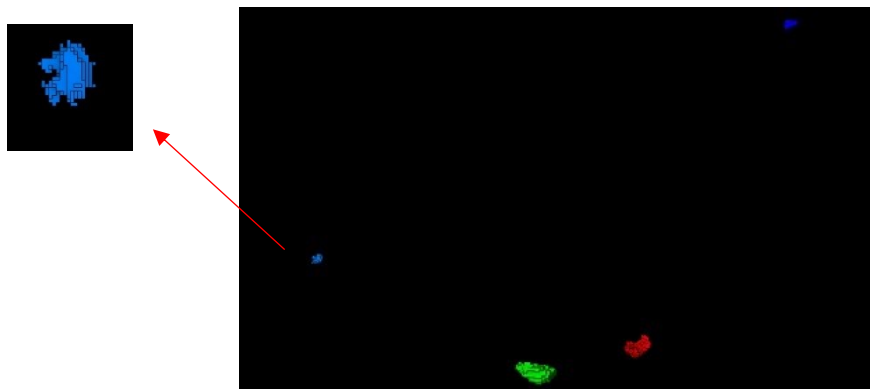
Figure 3. 14: Particles of seq 10

3.2.2. Influence of sphericity

To consider the influence of sphericity of the particles and to observe deviations resulting from this property, the aspect ratio of particles was taken into account. Aspect ratio is defined as the ratio of longest width to the longest length of particles. There are two series of particle data available (real particles size 3D and cuts of particles 2D), aspect ratio was calculated separately for the two systems. Both aspect ratio on 3D particles and of their 2D cuts were considered. If there is a systematic underestimation of a certain kind for very high aspect ratio of particles, we

can consider the possibility of putting a warning that the estimate should be discounted due to the high or low aspect ratio in this case.

3.2.3. Aspect ratio of 3D particles

The aspect ratio of 3D particles provides information on the particles properties that allow for the assessment of the quality of the method. Mainly, it gives information on why the method has some deviations in terms of particle shapes. To evaluate the influence of 3D aspect ratio on the results, the sample space is split by aspect ratio quartiles, as shown in Table 3.6.

Table 3. 6: Quartiles of aspect ratio of 3D particles (prior data).

Quartiles of aspect ratio of 3D particles					
	0%	25% (Q1)	50% (Q2)	75% (Q3)	100% (Q4)
Range	0.1395188	0.3568155	0.4397003	0.5281389	0.8236856

An individual prior is derived from the particles falling within each quartile. The same methods are applied to obtain histograms, a summary of Q-values, and posterior curves for the data in each quartile of the 3D aspect ratio of particles.
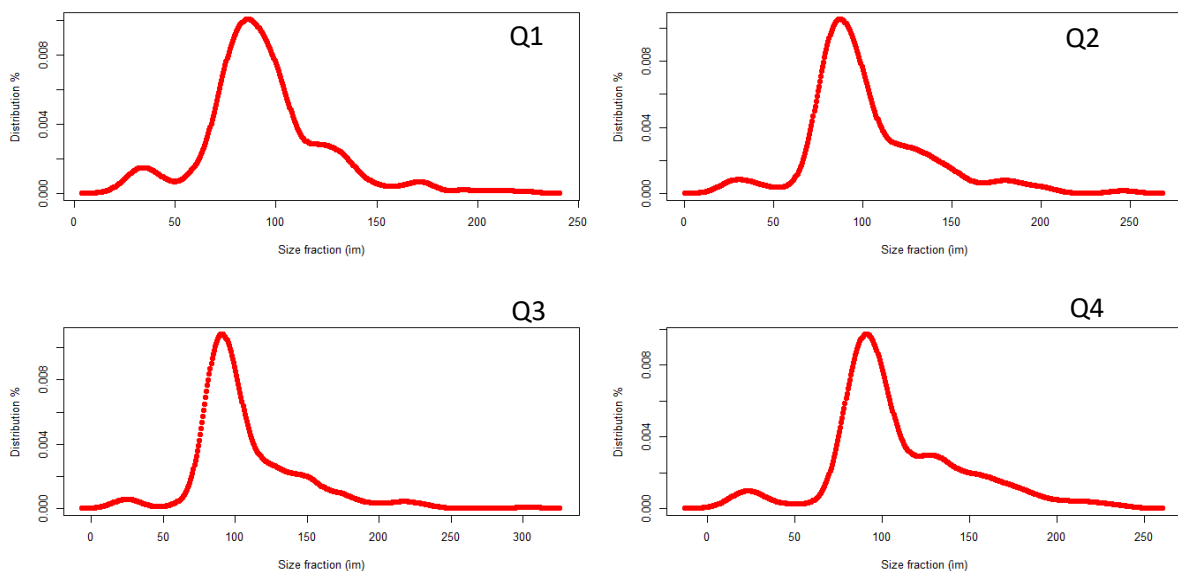
Figure 3. 15: Prior curves of each quartile of aspect ratio of 3D particles

From the histograms in Figure 3.16 can see the method is performing similarly for all aspect ratio classes. The histograms are roughly flat, but that decrease in the last three bars.

Table 3. 7: Summary of Q-values of each quartile of aspect ratio of 3D particles

Aspect ratio quartiles	Summary Q-values of aspect ratio of 3D particles					
	Min.	1st Qu	Median	Mean	3rd Qu	Max
Q1	0.006	0.150	0.325	0.359	0.550	0.943
Q2	0.001	0.153	0.339	0.365	0.549	0.996
Q3	0	0.156	0.352	0.375	0.554	1
Q4	0.002	0.175	0.350	0.381	0.577	1

Table 3.7 reports, for each aspect ratio class, how the Q-values are distributed. Essentially, we would expect the minimum to always be 0 and the maximum to be 1, while the quartiles and median should be near 0.25, 0.5 and 0.75, respectively. It is shown that all 4 series show similar deviations from these expectations, with none of aspect ratio group showing a large difference. However, the Q-values slightly increase from quartile one to four. It can be concluded that the aspect ratio of 3D particles influences the method, but not notably.
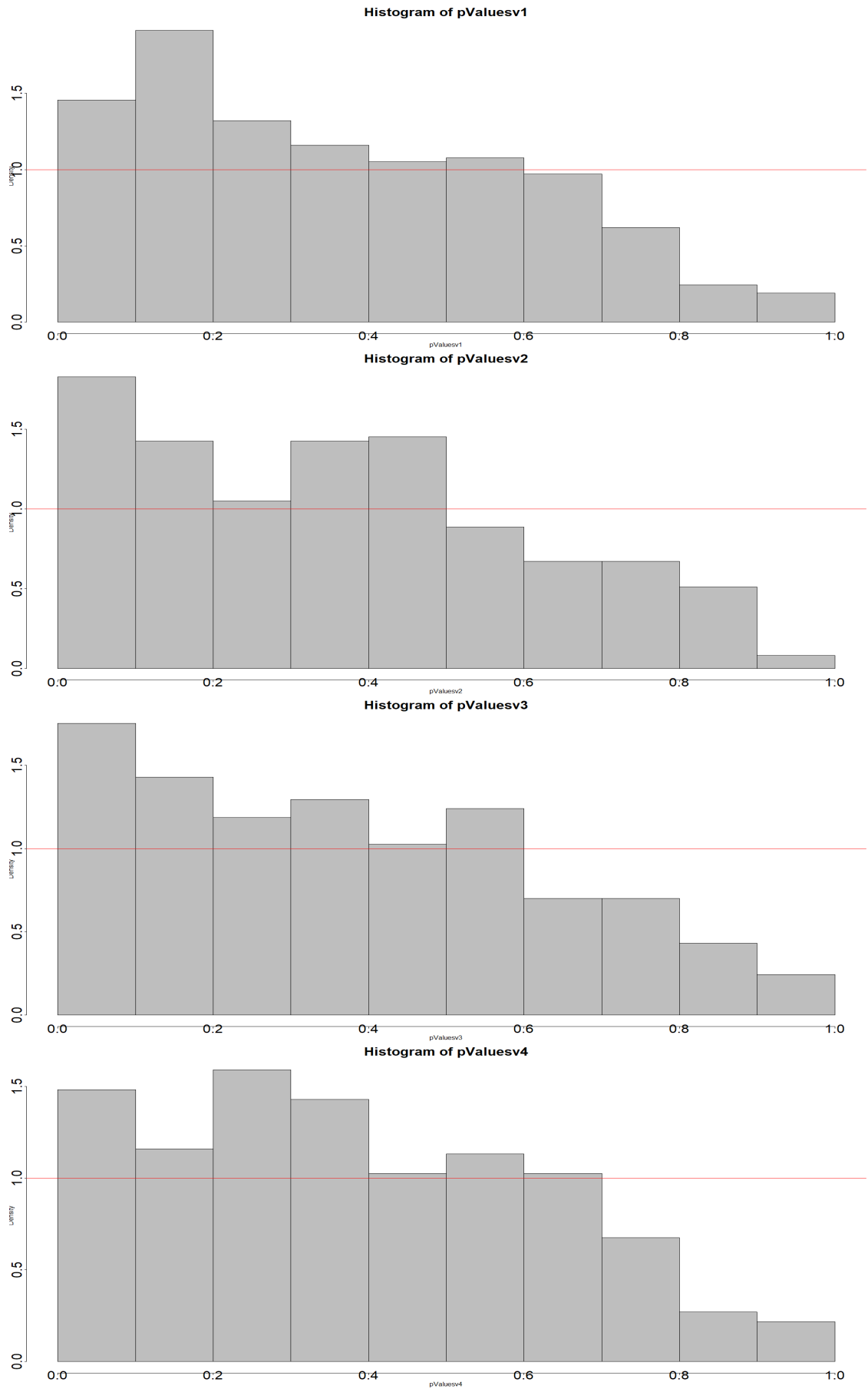
Figure 3. 16: Histograms of each quartile of the aspect ratio of 3D particles

Table 3. 8: Posterior examples of each quartile of aspect ratio of 3D particles and sequences
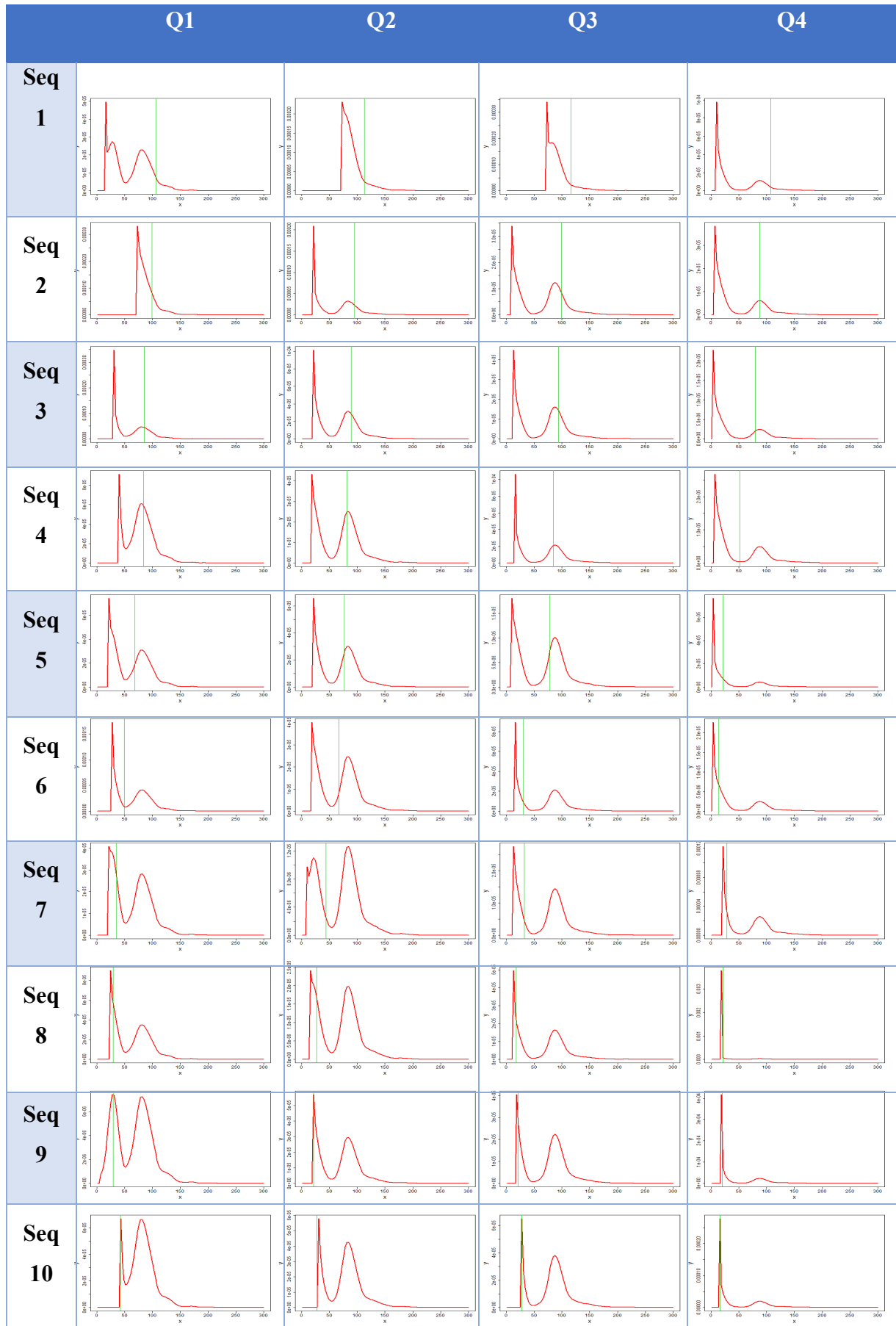
In table 3.8, the posterior curves of each quartile are displayed. As can be observed, the posterior curves behave differently, such as column one - row two or column two - row one, where a spike in leftmost part of the posterior is noticeable, which means the size of particles cut (2D) is big. On the other hand, in the fourth column and some in the third column in most sequences, the spike does not exist and small bumps appeared instead. It can be concluded that, when there are small bumps, the cut is small for the aspect ratio near one (more spherical shape). In figure 3.17 boxplots of real particle size by quartiles of aspect ratio of 3D particles are shown.
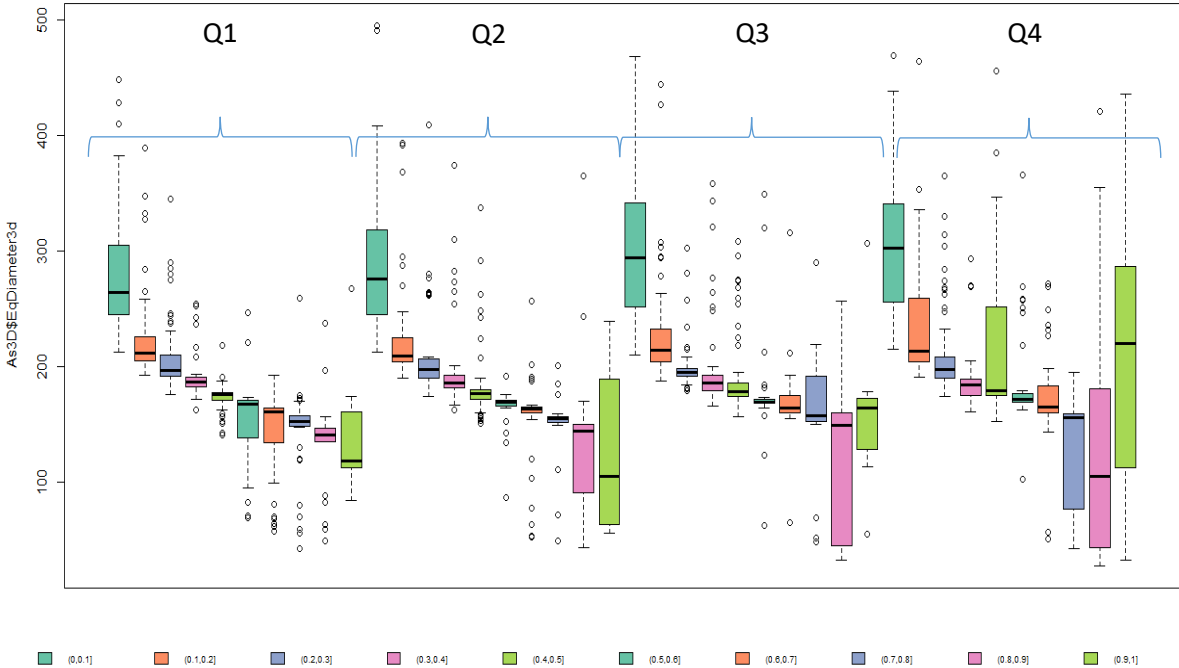
Figure 3. 17: Boxplots of each quartile of the aspect ratio and the sequences of them with 3D size of particles for quartz lump

In figure 3.17, the actual 3D size vs. ten sequences of the histograms and four aspect ratio classes is shown, with the highest to lowest sphericity (aspect ratio) from right to left. A clear, decreasing trend is apparent in all four 3D aspect ratio quartiles. As shown for each aspect ratio class, the larger the Q-value is, the smaller particles become. For example, in the leftmost quartile (Q1), the ten boxes represent one of the sequences between 0-0.1 and 0.9-1. As Figure 3.17 shows, particles with the lowest Q-values are large and with increasing Q-value, the particles get smaller. In the lowest quartile, we see lower frequencies and not as much data as in the other quartiles. The box plot in the last (sequences) bar of the 4th quartile has a larger spread of data, but the number of particles here is very low. It can also be observed that the

median decreases consistently for each sequence in the first two quartiles (the tick bar). In the third and fourth quartiles, there are higher uncertainties; in the last bars, the boxes are more extensive and much more prominent.

Moreover, the lack of data relative to the other sequences is the reason for the larger spread of data for the last sequence of each quartile. It can be concluded that the aspect ratio of actual particles (3D) does not have a significant influence on the quality of the results. Furthermore, we see that for every quartile of aspect ratio, the larger particles tend to have lower Q-values, and this is general for all aspect ratios. This occurs consistently, except for the highest aspect ratios.
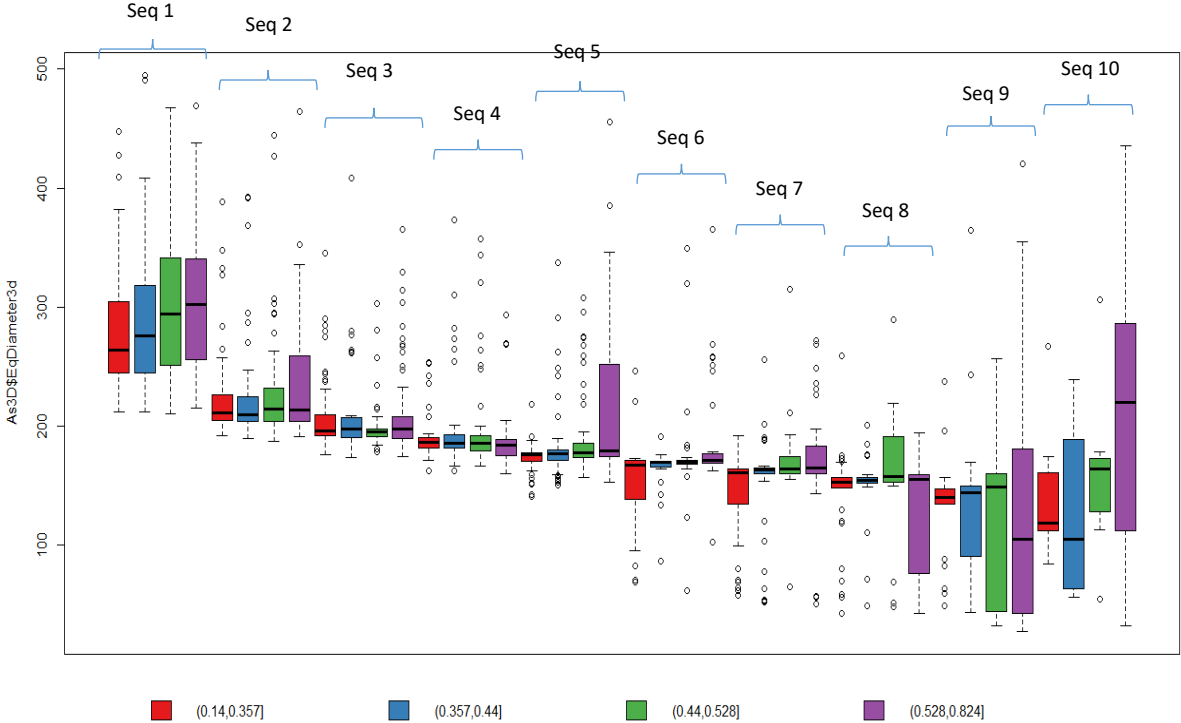
Figure 3. 18: Boxplots grouped by quartiles of aspect ratio by each sequence of quartz lump.

Figure 3.18 shows the same information as figure 3.17, but with a differnet ordering of the boxes, to get a clearer visualization of the influence of aspect ratio. Quartiles of aspect ratio for each sequence are grouped next to each other. As it is shown decreasing trend is same as figure 3.17. At figure 3.18 is shown in each sequence, the size classes tend to increase from quartile 1 to 4. It means in the same sequence with equal Q-values, size of particles increase from lower to higher sphericity. This trend continues until sequence 9. In sequences 9 and 10 things are more uncertain and have bigger boxes with the reason for this being the lower frequencies in those boxes. From figure 3.18 can conclude that the particles size are bigger in higher aspect ratio class of particles (more sphere particles) with the same Q-values. Figures 3.19 to 3.22

show the same observation as the above boxplots for two different materials, apatite, and quartz fine.
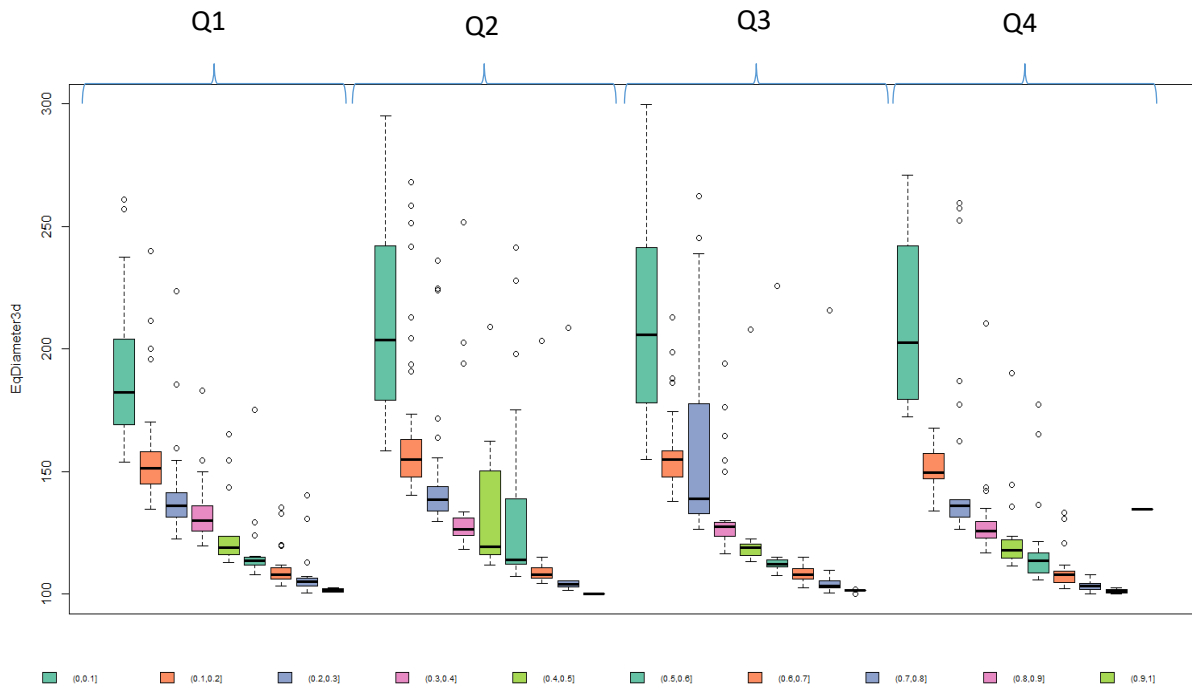
Figure 3. 19: Boxplots of each quartile of the aspect ratio and the sequences of them with real size of particles for apatite
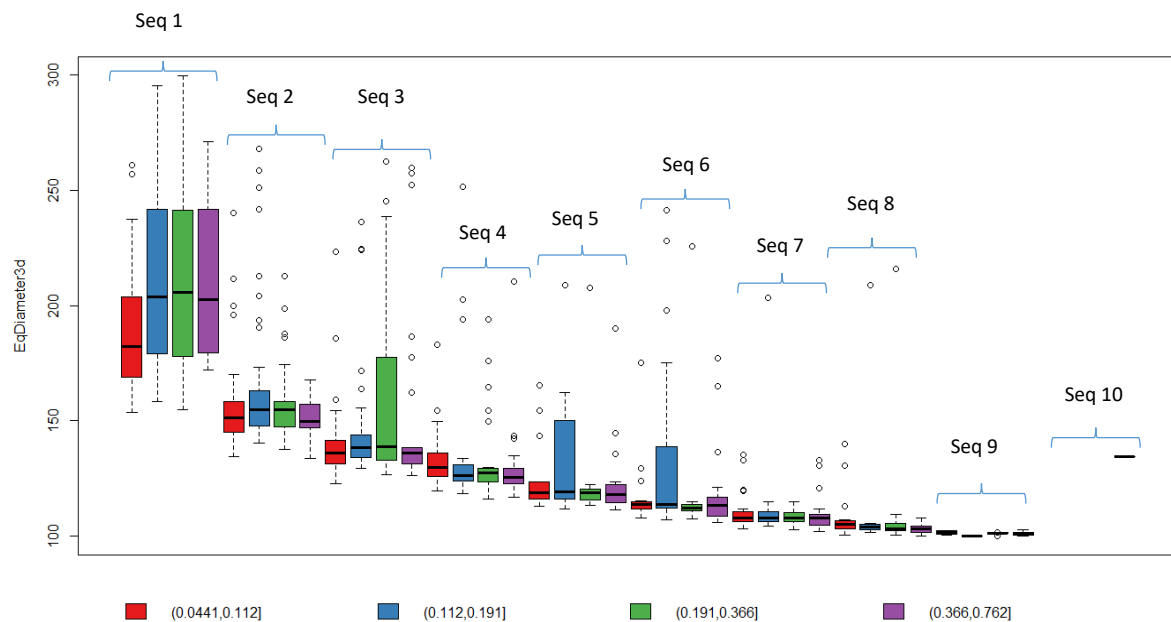
Figure 3. 20: Box plots grouped by quartiles of aspect ratio by each sequence for apatite

As we can see, for apatite this change the change of size is more pronounced from the first to the last sequence in comparison to minerals such as quartz. The reason for this is a higher

amount of smaller particles than larger particles in the sample space, also size of particles in each sequence increases from lower to higher aspect ratio classes.
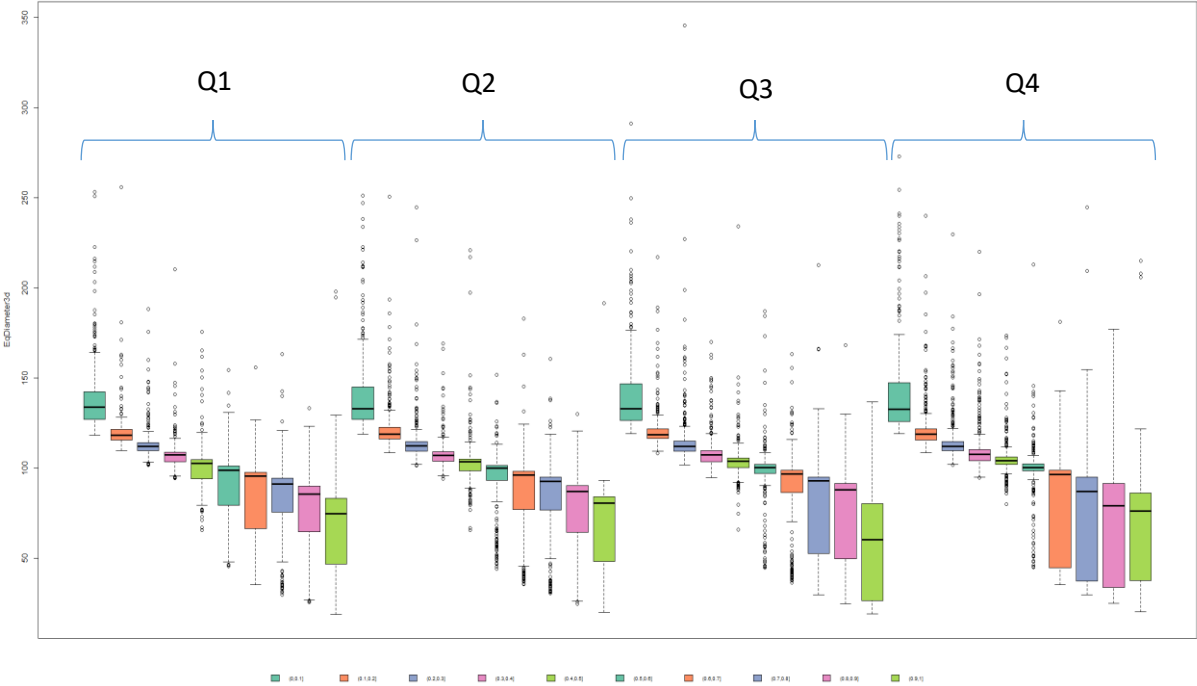

Figure 3. 21: Boxplots of each quartile of the aspect ratio and the sequences of them with real size of particles for quartz fine
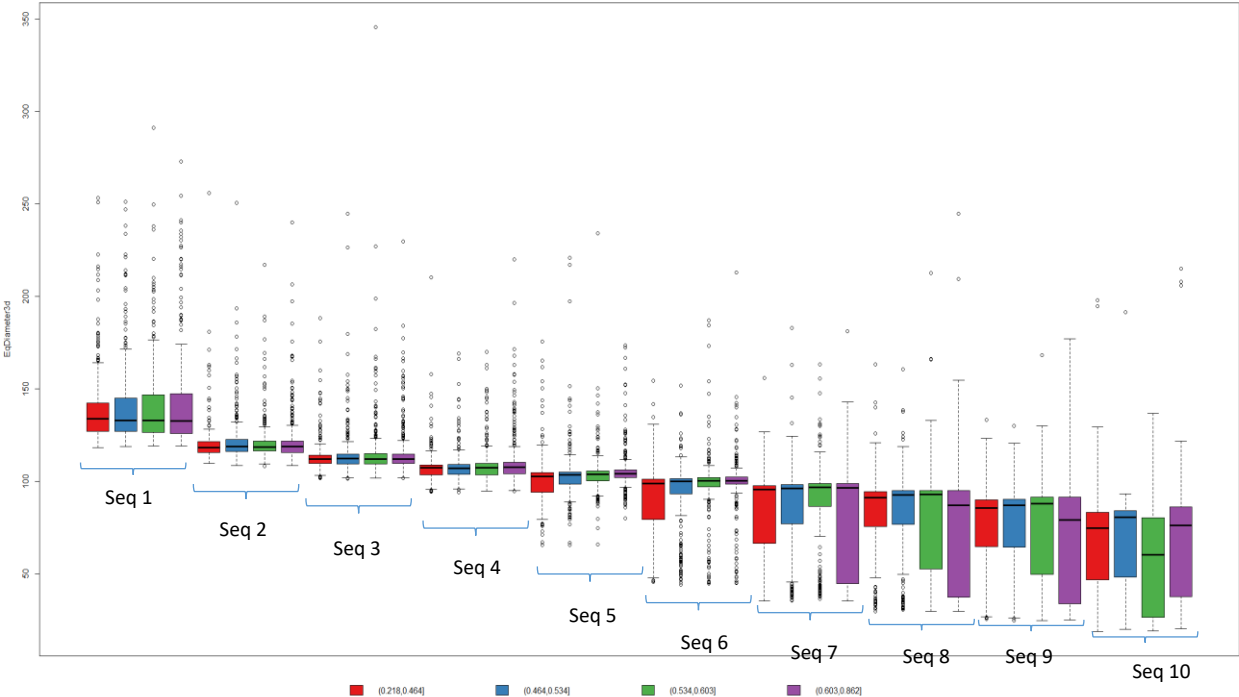
Figure 3. 22: Box plots grouped by quartiles of aspect ratio by each sequence for quartz fine.

As we can see for quartz fine, the change is smoother because of more homogeneous size classes. As shown in the box plots, the effect of particle aspect ratio on the current method is not significant and the main property that has influenced Q-values is particle size. This is true across all minerals considered. It could be observed that as the particles get smaller, the sequence number increases and the frequency of particles decreases.

3.2.3.1. Aspect ratio of 2D particle cuts

Considering the aspect ratio on 2D cuts, i.e. the apparent aspect ratio, can provide insight on how shape of 2D cuts can influence the method. To evaluate the influence of aspect ratio of 2D cuts on the results, the samples of particles are split by 2D cuts aspect ratio quartiles, as shown in Table 3.9.

Table 3. 9: Quartiles of aspect ratio of 2D particles (r).

Quartiles of aspect ratio (r size)					
	0%	25%	50%	75%	100%
Range	0.1168673	0.3906805	0.5260452	0.6483720	0.9226922
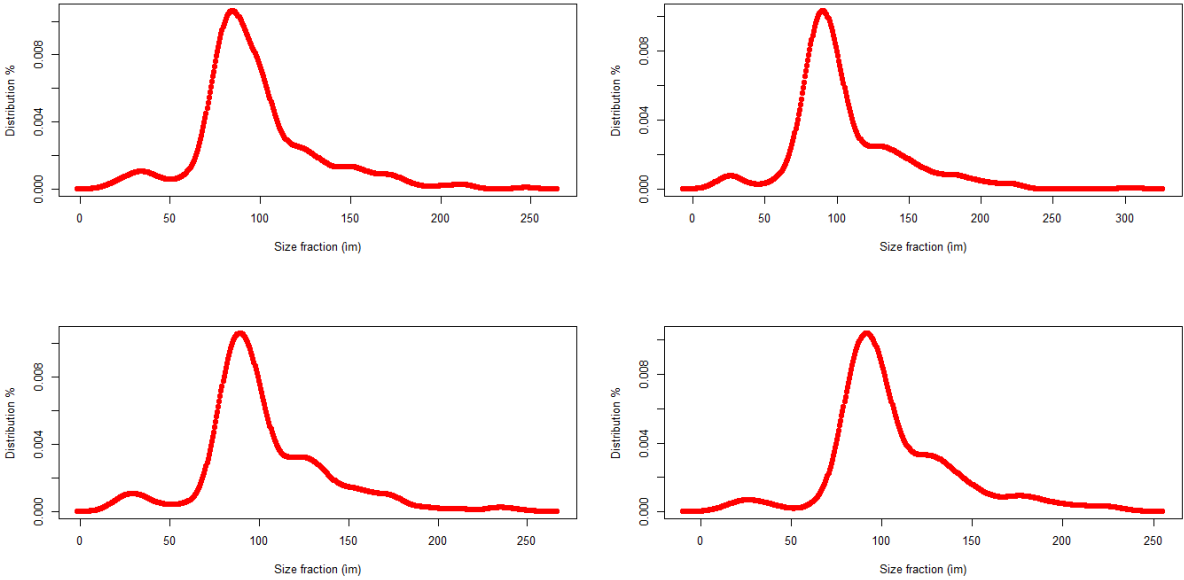
Figure 3. 23: Prior curves of each quartile of aspect ratio of 2D particles

The same as for the previous subsection, priors are derived from each quartile of 2D cuts. The same process was implemented as in the previous section. From the histogram of each quartile, as seen in Figure 3.24, the effect of sphericity from the first quartile to the last quartile of 2D

aspect ratio is evident. The Q-values increase more noticeably than in the results of the 3D aspect ratio. However, deviations from the first bars to the last bars of the histograms remain. In Figure 3.24, histograms of Q-values display a slight increase from the first quartiles of aspect ratio to the fourth.
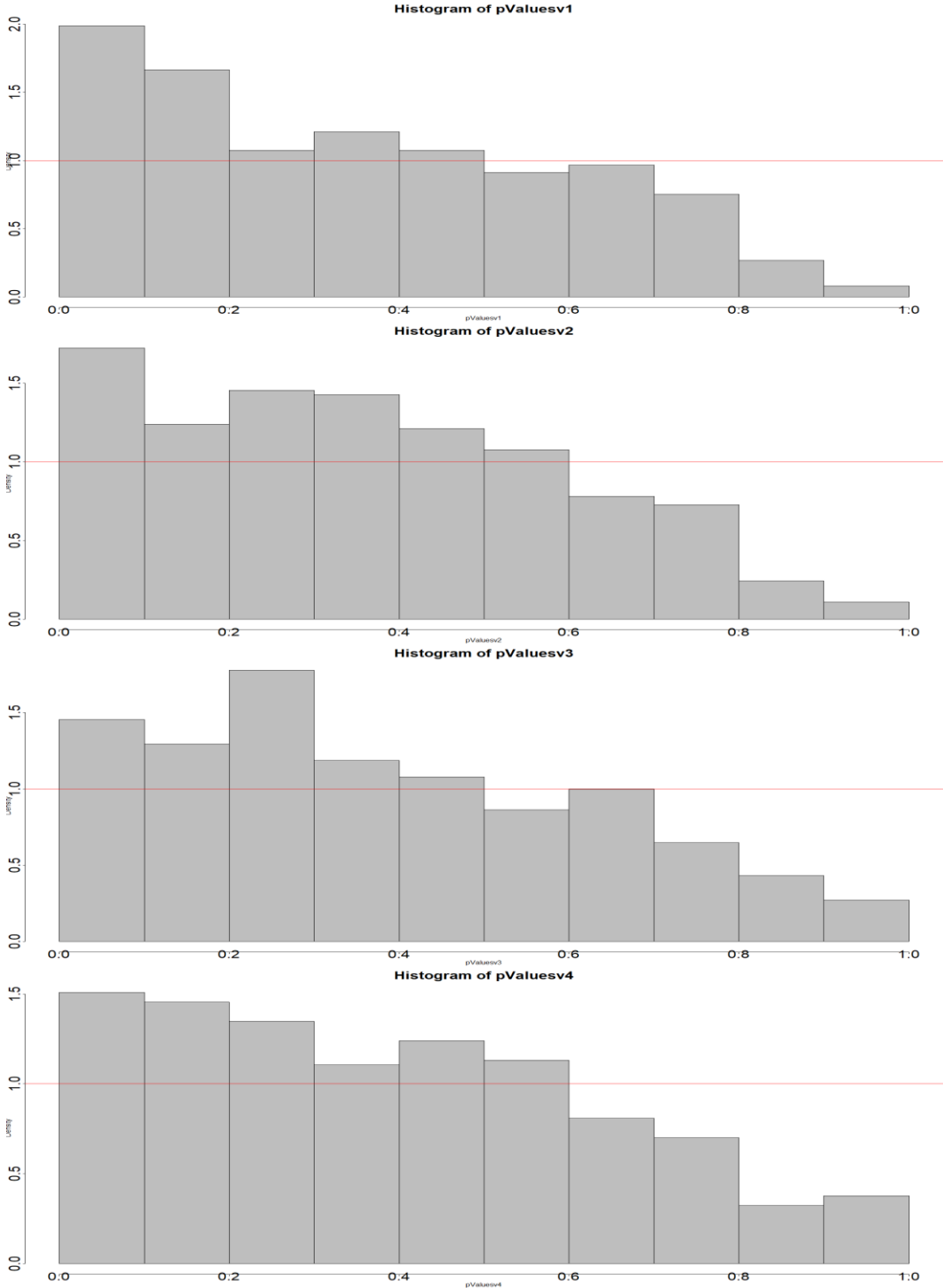
Figure 3. 24: Histograms of each quartile of the aspect ratio of 2D cuts of particles

Table 3. 10: Summary of Q-values of each quartile of aspect ratio of 2D cuts of particles

Aspect ratio range	Summary Q-values					
	Min.	1st Qu	Median	Mean	3rd Qu	Max
Q1	0.001	0.132	0.327	0.351	0.561	0.936
Q2	0	0.170	0.346	0.362	0.539	0.973
Q3	0.001	0.177	0.336	0.383	0.578	0.963
Q4	0.003	0.163	0.376	0.390	0.573	1

In Table 3.10, the distribution of the Q values for each aspect ratio class are reported. It is expected that the minimum will always be 0 and the maximum 1, while the quartiles and median should be near 0.25, 0.5 and 0.75, respectively. All 4 series show similar deviations from these expectations, none of aspect ratio group shows a significant difference. However, the Q-values increase slightly from quartile one to four; it is seen that the aspect ratio of 2D cuts of particles influences the method but not significantly.

In Table 3.11, posterior curves of each quartile and sequence are shown. As it is shown from quartiles one to four (columns one to four), the spikes of the posterior curves get smoother; however, there are exceptions, such as sequence three in the fourth quartile since a big particle can seldom be cut across the center. In figure 3.25 to figure 3.30 boxplots of the three minerals and the influence of the size of real particles and aspect ratio of 2D cuts are shown.

From the boxplots of all the minerals, it can be interpreted that particle cut sphericity affects the method but not as much as the property of size of particles. It is shown, by quartiles of aspect ratio of 2D cuts of particles there is the same results as the previous settings of aspect ratio of 3D particles. The only different from previous setting is that in the same sequence the size of particles are randomly distributed in each quartile of aspect ratio and do not change gardually with increasing the sphercicity from quartile 1 to 4.

The aim of these exercises were to evaluate which effects or properties of particles control how well the method works. The possible criteria that have an influence are real size, real aspect ratio and apparent aspect ratio. From all the observed properties in this chapter, the influence of size, both 3D and 2D, is the main factor that affects the results.

Table 3. 11: posterior examples of each quartile of aspect ratio of 2D cuts
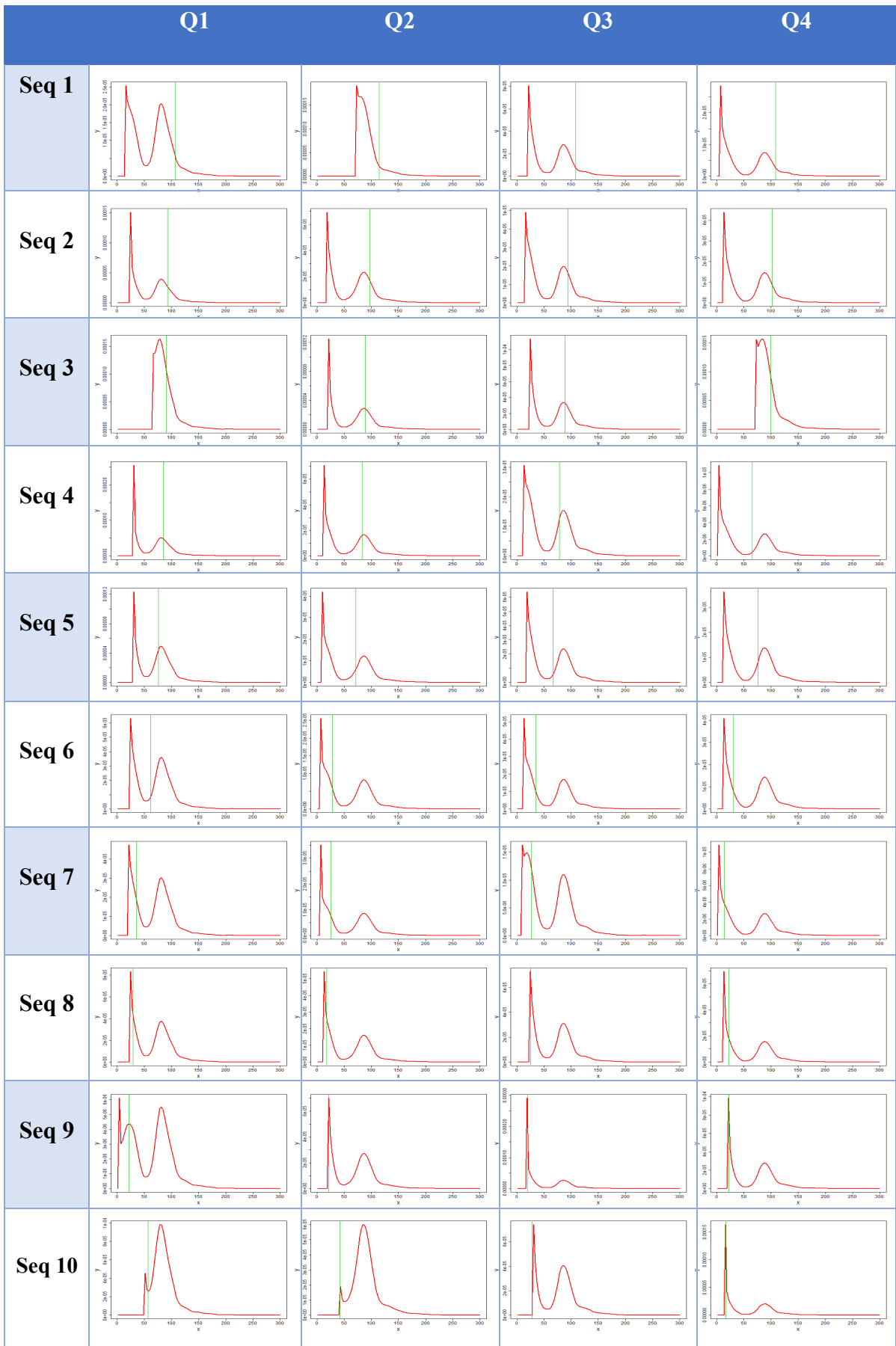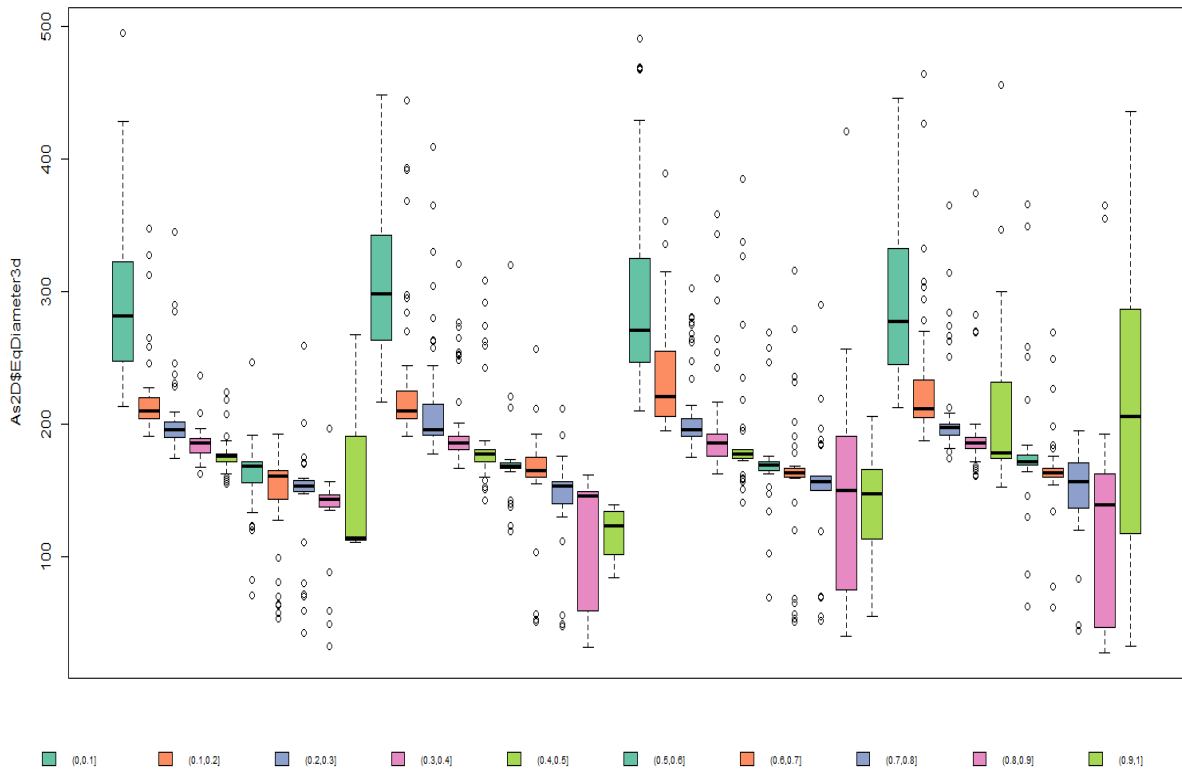
Figure 3. 25: Boxplots of each quartile of the aspect ratio of 2D cuts and the sequences of them for quartz lump
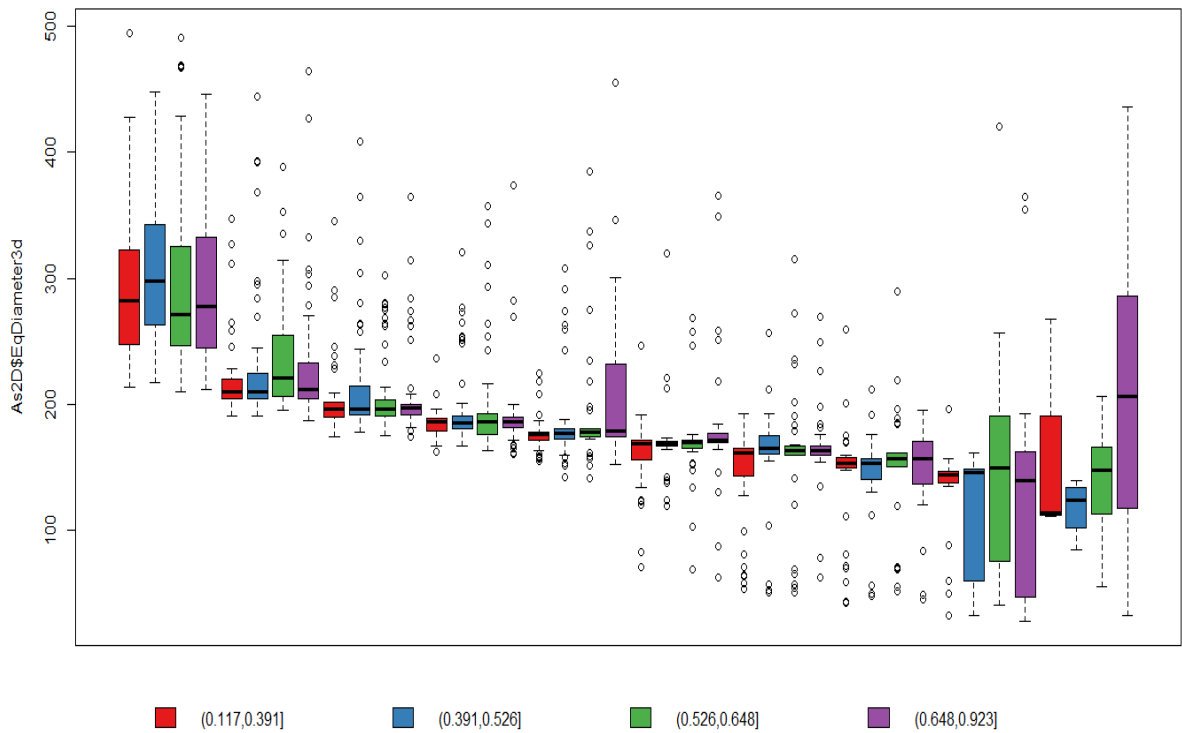
Figure 3. 26: Boxplots grouped by ten sequences and four quartiles of aspect ratio of 2D cuts for Quartz lump.
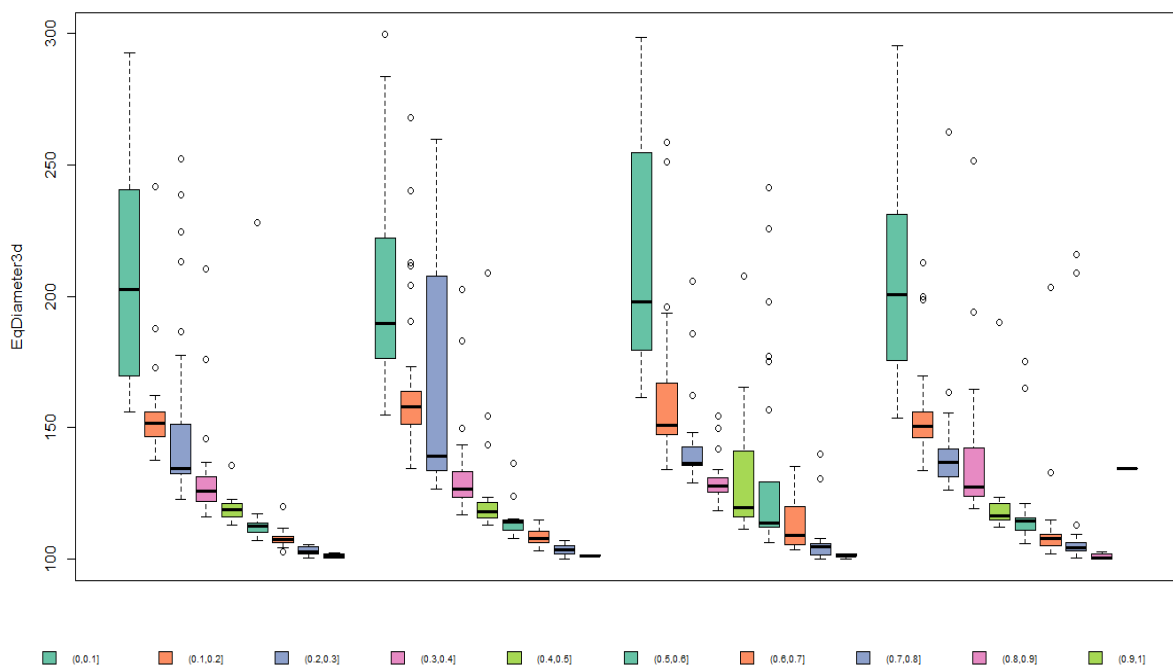
Figure 3. 27: Boxplots of each quartile of the aspect ratio of 2D cuts and the sequences of them for Apatite
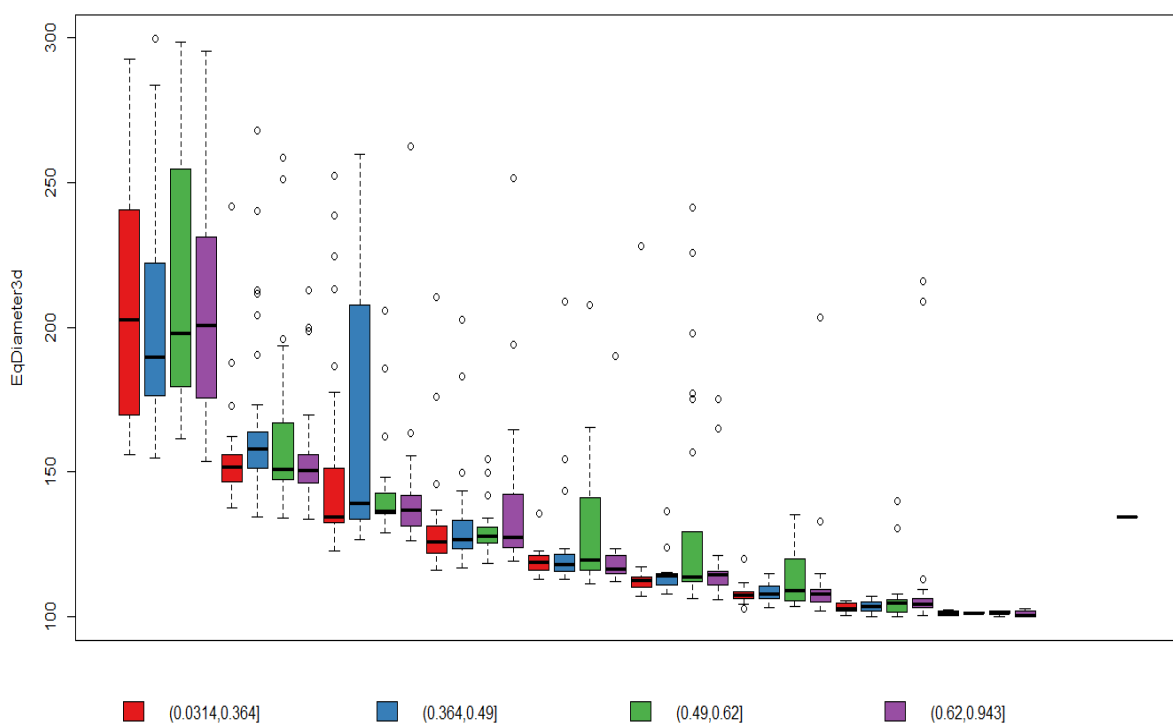
Figure 3. 28: Boxplots grouped by ten sequences and four quartiles of aspect ratio of 2D cuts for Apatite
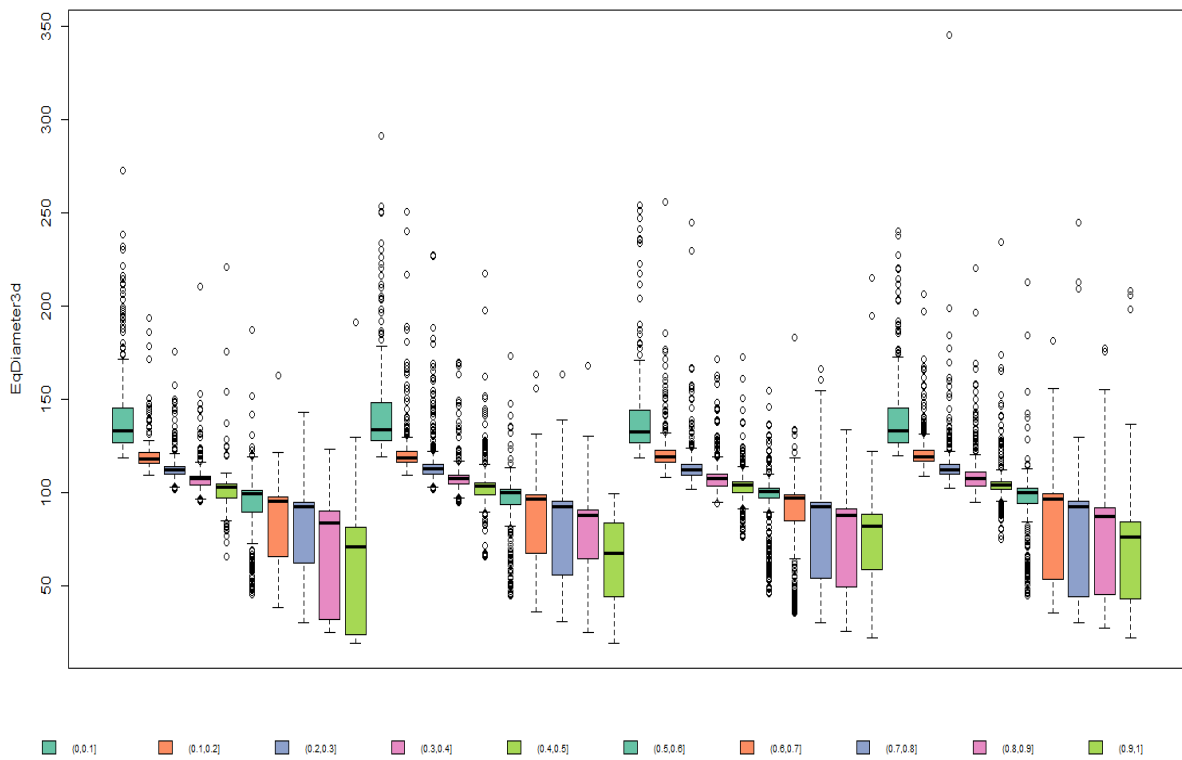
Figure 3. 29: Boxplots of each quartile of the aspect ratio of 2D cuts and the sequences of them for quartz fine
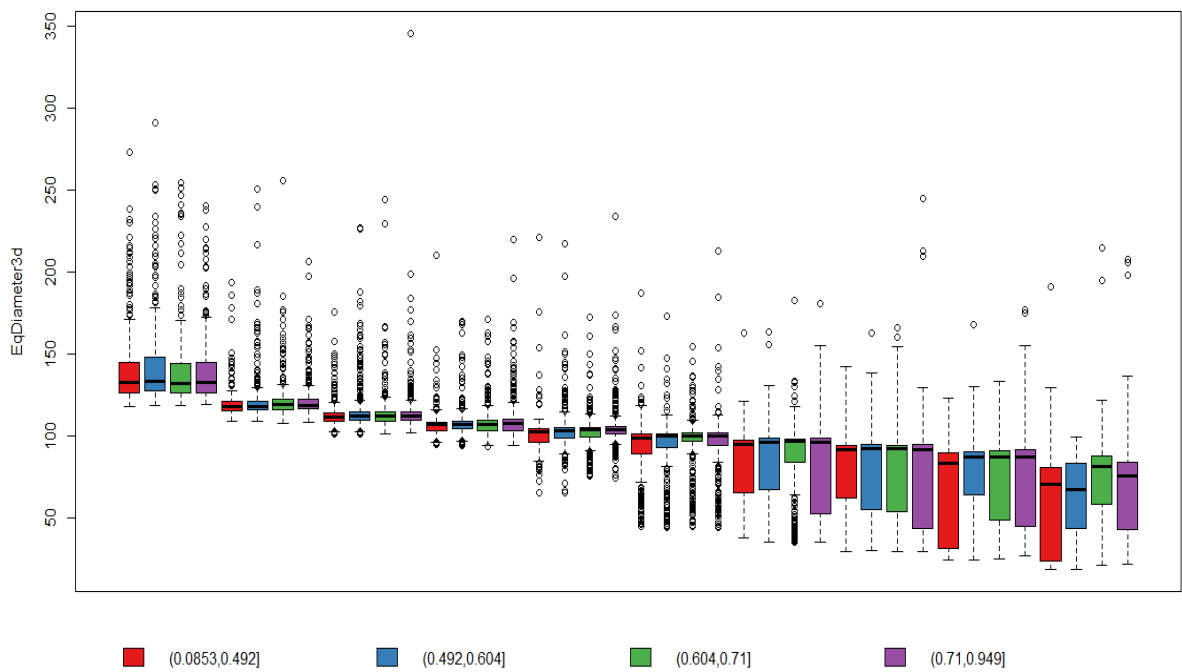
Figure 3. 30: Boxplots are grouped by ten sequences and four quartiles of aspect ratio of 2D cuts for quartz fine

Chapter 4. Results

After proposing the model and identifying the deviations, and influence of size in the model, the method is implemented on actual data. As already mentioned in methodology chapter 2, to incorporate the data of LD into the model, a conversion to number distribution is required. After conversion the prior curves are extracted. Tables 4.1 to 4.2 show the obtain distribution before and after conversion from volume (mass) to number distribution and Figures 4.1 to 4.3 show the prior curves of prior distribution from the data of Table 4.2. The likelihood equation curves, depending on the cuts size (2D size) are evaluated same method in chapter 2 with Eq. (2-10). Prior curves and likelihood curves are multiplied as Eq. (2-3) to obtain posterior curves as it is shown in Table 4.4. The actual particle size was placed on posterior curves and implemented as a green line (Table 4.4). The integral of $Q(R)$ from Eq. (2-11) is computed and results are represented as histograms in figures 4.4 to 4.6 for each mineral separately. All the details are shown in the following subsections of this chapter.

4.1. Calculation of Volume (Mass) to Number Distribution Conversion

First of all, results of prior data from table 2.4 are filtered by the size of particles in the range that could have XCT data; the results are shown in Table 4.1. After wards, the data of Table 4.1 is imported into equation (4-1), and number distribution are derived, as seen Table 4.2.

$$q_0(d) = \frac{\int_{d_u}^{d} d^{-3} q_3(d)\, d(d)}{\int_{d_u}^{d_0} : d^{-3} q_3(d)\, d(d)} \approx \frac{\sum_{i=1}^{n} d_{m,i}^{-3} \cdot \mu_{3,i}}{\sum_{i=1}^{N} d_{m,i}^{-3} \cdot \mu_{3,i}} \tag{4-1}$$

In Eq. (4-1) q_0 (d) represents the number distribution and d_u and d_0 represent lower and upper particle size limit respectively. q_3(d) denotes particle size-frequency distribution and $d_{m,i}$ and $\mu_{3,i}$ represent mean interval and mass fraction, respectively. N is the overall number of intervals and n denotes the running number of intervals.

4.2. Prior Distribution Data and Curves

Table 4. 1: Laser diffraction results base on volume (mass) distribution

Sieve size (µm)	Fraction (wt %)		
	Quartz lump	Quartz fine	Apatite
0.5	0	0	0
4.5	0	0	0
5.5	0	0	0
6.5	0	0	0
7.5	0	0	0
9	0	0	0
11	0	0	0
13	0	0	0
15.5	0	0	0
18.5	0	0.415	0
21.5	0	0.422	0
25	0.329	0.522	0
30	0.555	0.826	0
37.5	0.972	1.415	0
45	1.026	1.546	0
52.5	1.018	1.606	0
62.5	1.319	2.288	0
75	1.558	3.585	0
90	1.787	6.569	0
105	1.867	9.748	9.745
125	2.980	15.797	10.972
150	5.249	19.745	12.038
180	9.199	18.497	13.952
215	13.795	11.413	16.552
255	17.159	4.511	18.131
305	20.470	1.062	18.611
365	17.265	0.029	0
435	2.810	0	0
515	0.606	0	0
615	0.032	0	0
735	0	0	0
875	0	0	0

Table 4. 2: Laser diffraction result of base on number distribution

Sieve size (μm)	Fraction (number %)		
	Quartz lump	Quartz fine	Apatite
0.5	0	0	0
4.5	0	0	0
5.5	0	0	0
6.5	0	0	0
7.5	0	0	0
9	0	0	0
11	0	0	0
13	0	0	0
15.5	0	0	0
18.5	0	23.413	0
21.5	0	14.644	0
25	20.315	11.527	0
30	20.673	11.017	0
37.5	19.584	10.218	0
45	11.319	6.115	0
52.5	6.805	3.847	0
62.5	5.373	3.340	0
75	3.713	3.061	0
90	2.464	3.246	0
105	1.559	2.918	36.168
125	1.517	2.882	23.826
150	1.564	2.107	15.127
180	1.586	1.143	10.223
215	1.387	0.411	7.199
255	1.024	0.096	4.662
305	0.722	0.013	2.794
365	0.356	0.0002	0
435	0.034	0	0
515	0.004	0	0
615	0.0001	0	0
735	0	0	0
875	0	0	0

As it has shown in Tables 4.1 and 4.2 the size of smaller particles are considered 0 in different size ranges. And also for one mineral (apatite) the range size of bigger particles are considered 0 as well. The main reason of it as mentioned in subsection 2.2.2 is because of particle size range should be the same as size range that could derive from XCT technique.
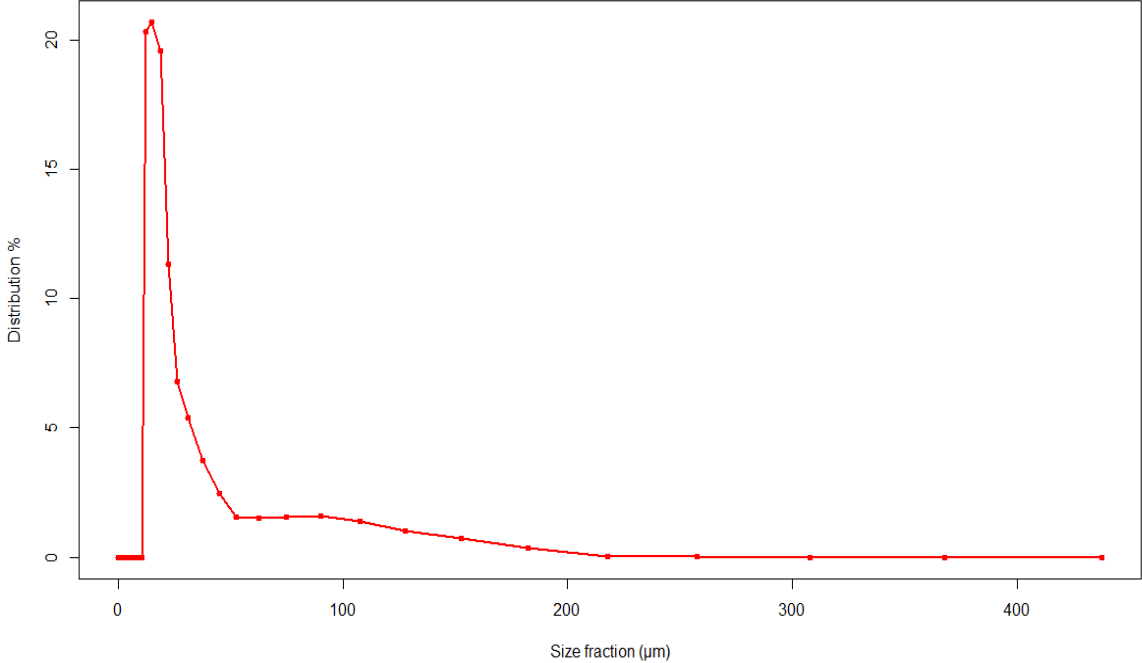
Figure 4. 1: Prior curve of quartz lump base on number distribution
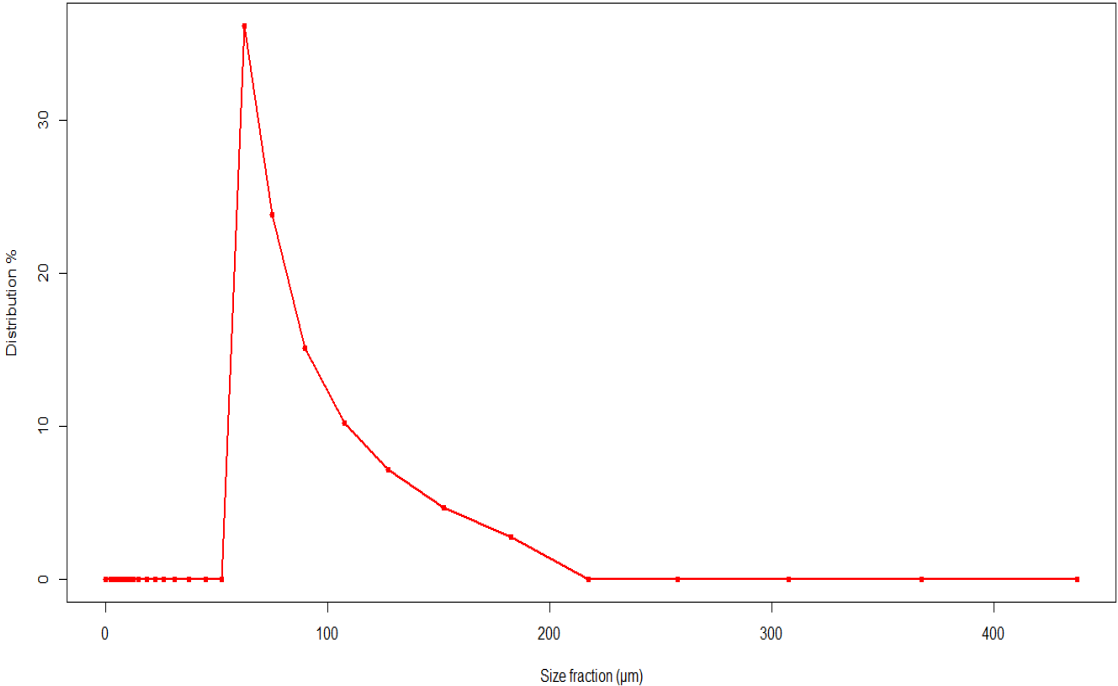
Figure 4. 2: Prior curve of apatite base on number distribution
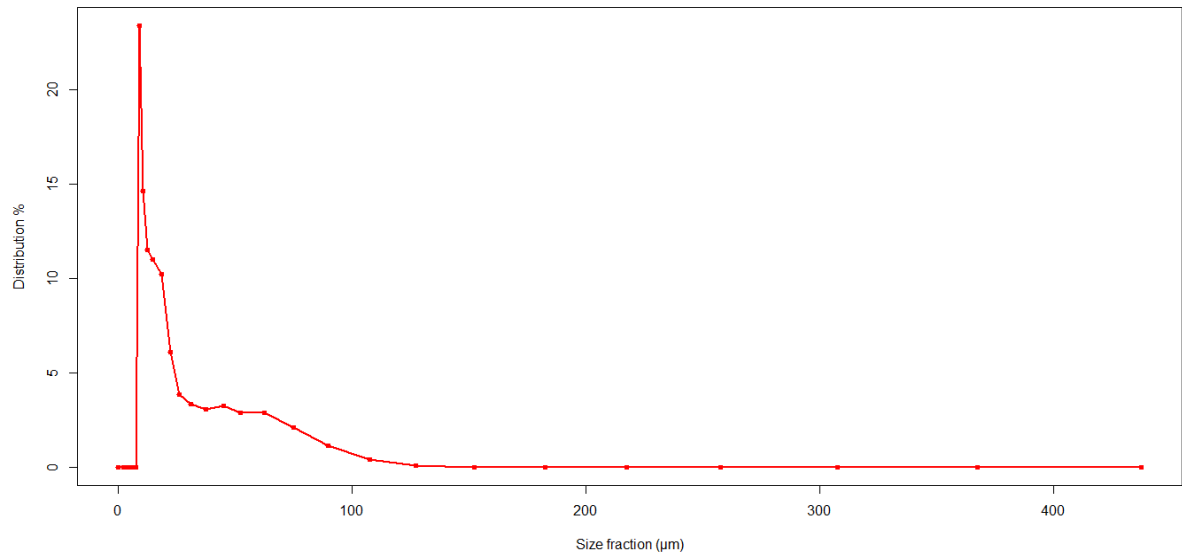
Figure 4. 3: Prior curve of quartz fine base on number distribution

4.3. Histograms of Actual Data for all Minerals
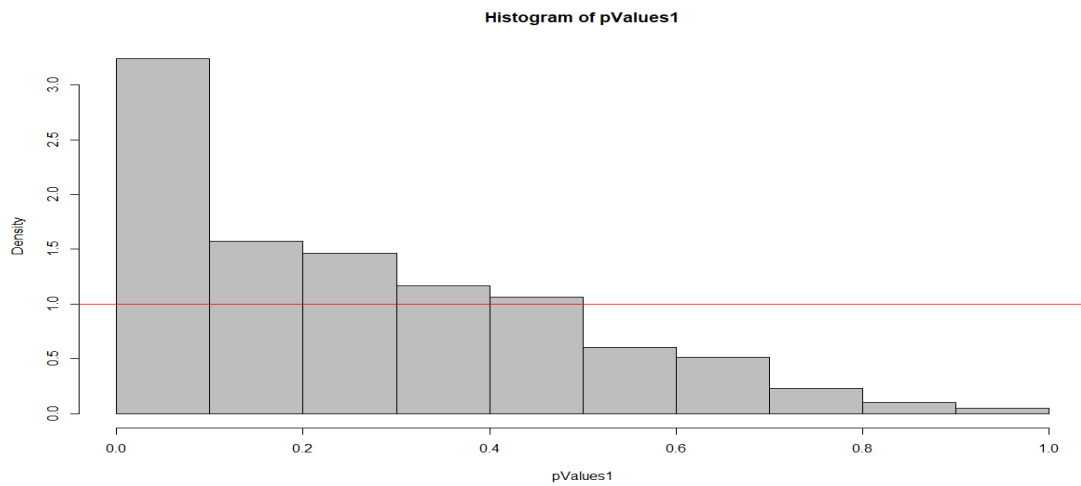
Figure 4. 4: Histogram frequency of quartz lump
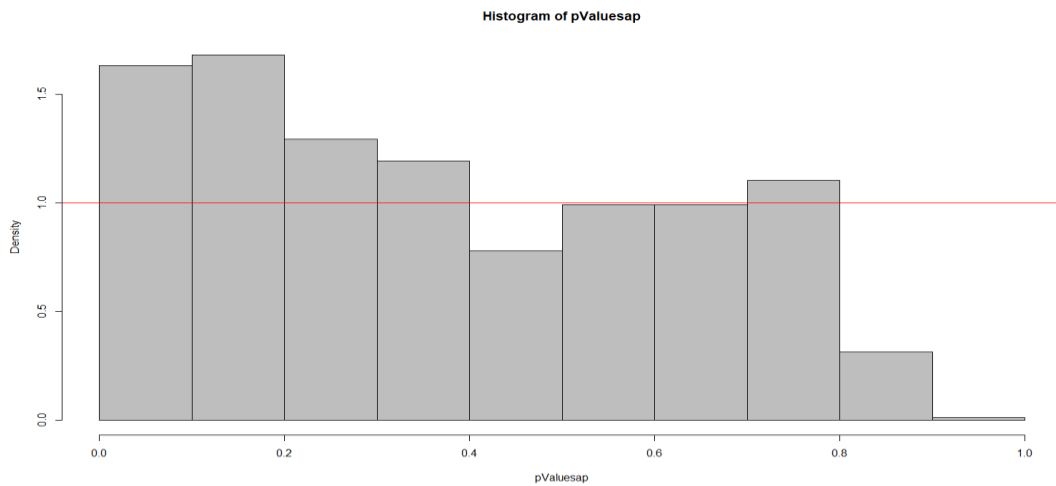
Figure 4. 5: Histogram frequency of apatite
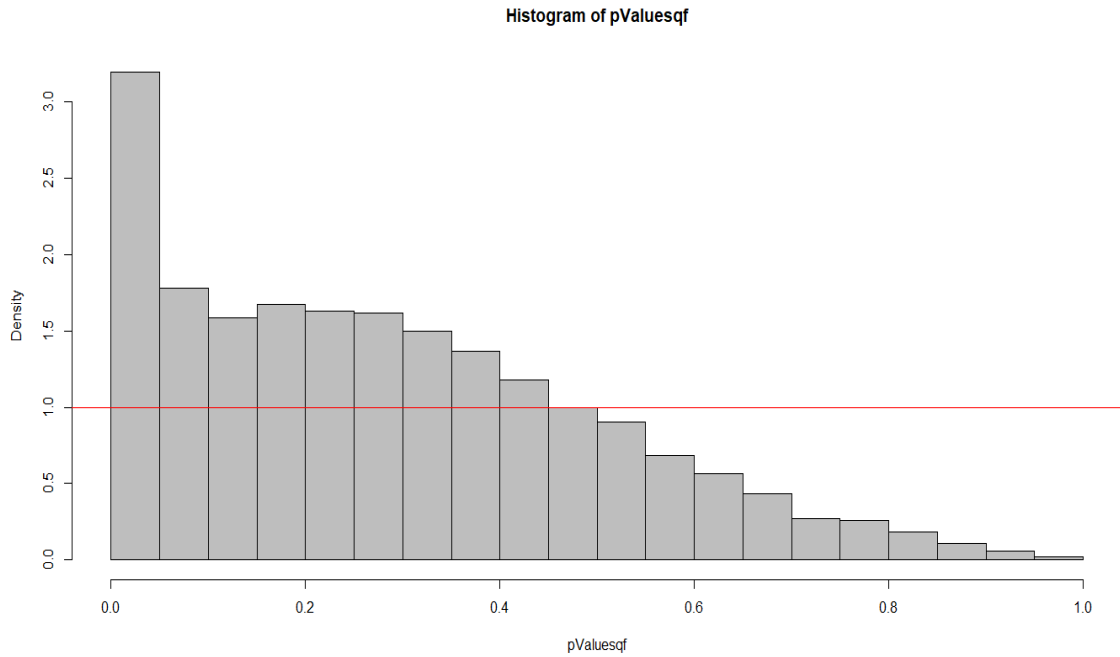
Figure 4. 6: Histogram frequency of quartz fine

4.4. Q-values of Minerals

Table 4. 3: Summary of Q-values of actual data

Aspect ratio range	Summary Q-values of actual data for minerals					
	Min.	1st Qu	Median	Mean	3rd Qu	Max
Quartz lump	0	0.067	0.212	0.257	0.406	0.954
Apatite	0.012	0.322	0.619	0.612	0.964	1
Quartz fine	0	0.169	0.361	0.389	0.588	1

The results show the method behaves the same way as in the previous chapter for diagnostic settings. It is shown that the histograms bars are roughly decreasing from the first bar to the last bar, which implies lower frequency of higher Q-values. Apatite behaves differently on a combination of actual data. This is possibly because of its limited range of size, as is shown in table 4.3. The summary Q-values in table 4.3 indicate that the method works better for smaller particles than larger ones. Posterior curves in Table 4.4 are also presented as examples of a combination with actual data. The validation line (indicating actual 3D size) moves to the left along the x-axis in different sequences, that is, apparent and real size become more or more similar.

4.5. Posterior Curves Examples of Minerals

Table 4. 4: Posterior curves of examples for actual data

	Quartz lump	Apatite	Quartz fine
Seq 1			
Seq 2			
Seq 3			
Seq 4			
Seq 5			
Seq 6			
Seq 7			
Seq 8			
Seq 9			
Seq 10			

Chapter 5. Conclusions, Strengths vs. Weaknesses and Future Work

5.1. Conclusions

The aim of this work is to derive a method with the specific objective of quantifying the uncertainty on the actual 3D size of each and every individual particle by combining the 2D cuts of particles from the cross-sections (possibly coming from MLA, in this work obtained from XCT) with 3D particle size distribution from the sample population (laser diffraction or sieving). This should serve to improve the assessment of data from MLA and other 2D automated mineralogy techniques in the future. For this, a statistical prediction model is provided that allows the probability distribution of particle size from 2D cuts to be generated in actual 3D. A series of analyses are applied, in a combination of analytical and statistical methods. Analytical techniques to obtain data and validate the model are divided into three parts: laser diffraction, XCT in 2D and XCT in 3D. In parallel, the statistical model subdivided in 1) prior, 2) likelihood, and 3) posterior.

For the prior, bulk sample population is needed, which is derived from laser diffraction data; laser diffraction measurement were performed several times and an average result was taken from all measurements. LD results are based on volume distributions, and a conversion to number distribution is required to consider particles equally important. The results of LD are restricted to the size range of particles which are measurable by XCT analysis as the likelihood input data (2D cuts) and validation data (3D) come from this technology. Two possible scenarios are considered for a prior distribution: 1) prior for model performance diagnostics; and 2) prior for actual data. The calculation of the likelihood required the establishment of a relationship between the two-dimensional cut of single particles with the actual 3D size, assuming that the particles are spherical (Eq. 2-10) for simplicity. The real two-dimensional cuts of the particles are generated from XCT data, although in reality they can be derived from MLA. For deriving the data from XCT, several steps were followed and the data are measured as the equivalent circular diameter of each particle. After completing the analytical dataset, the data is embedded into the statistical model. The model takes global properties of particles and converts them to individual particle information. For validating the method, the actual particle size in 3D from XCT data are displayed on the posterior curve. The results are more acceptable the closer the true 3D size is to the peak of the distribution of the posterior curve. For this, a Q-value of validation is calculated by evaluating an integral of the upper tail of the posterior curve,

from the validation point to infinity, divided by the whole area under the curve, as shown in Eq. (2-11). As $Q(R)$ becomes closer to 1, the true and the apparent size are more similar to true size of the particle.

The method performance is evaluated by using the XCT data both as prior and as validation. Histograms show the whole results to compare the variabilities of the method, and evaluate which particle properties may control the method performance. There is a relation between larger particle size and lower Q-values. The effect of size is more noticeable than the effect of aspect ratio of particles; however, splitting the analysis in 2D sphericity classes showed slightly better performance. These behaviours were also observed when using the second scenario for the prior, i.e. using laser diffraction data as prior, thus allowing to conclude that the differences in the physical measurement process between LD and XCT are not strong for this method performance. However, size of particles has a notable effect on Q-values.

From the histograms of final results we can find that two biases are apparent, being highlighted as well by previous literature studies. The same as Cuzzi and Olson (2017) found biases of 1) larger particles are more sampled because of their larger size; and 2) a random cut is likely to be non-diametrical. Benito et al. (2019) further developed the method by considering ways to tackle the biases proposed by Cuzzi and Olson.

5.2. Strengths and Weaknesses

The method strengths are that it can be applied to different analytical techniques with different sets of measurements and represent results as one output. For example, this study used laser diffraction and XCT, one based on volume and the other on number distribution. The various diagnostic checks helped identify the deviations, localize them and improve the model before running it on actual data. Any single-particle used in the model can be tracked and its properties observed.

The weaknesses of the current method include that is limited to the dominantly spherical particles as all particles must be considered perfect spheres. The deviation of overestimation in the first bar of the histogram of actual application data increased as the probability of counting particles cuts for bigger particles increases, and also in higher Q-values have less frequencies as the last bar of histograms.

5.3. Future Work

By considering the current behaviour of the model and decreasing the biases by using the techniques were mentioned from previous studies, the model should be extended to incorporate particle shape parameters such as length, width and height, sphericity or aspect ratio. In this way, the various particles shapes could be considered. However, this would increase the complexity of the calculations. From an analytical point of view, perhaps measurements could be replicated for classed particles to more accurately observe the behaviour of the method for particles of different size classes. 2D cuts can achieve from MLA analysis and use as the inputs of the model.

Bibliography

Al-Thyabat, S.; Miles, N. J.; Koh, T. S. (2007): Estimation of the size distribution of particles moving on a conveyor belt. In Minerals Engineering 20 (1), pp. 72–83. DOI: 10.1016/j.mineng.2006.05.011.

Bengio, Yoshua; Courville, Aaron; Vincent, Pascal (2013): Representation learning: a review and new perspectives. In IEEE transactions on pattern analysis and machine intelligence 35 (8), pp. 1798–1828. DOI: 10.1109/TPAMI.2013.50.

Benito, Santiago; Cuervo, Carlos; Pöhl, Fabian; Theisen, Werner (2019): Improvements on the recovery of 3D particle size distributions from 2D sections. In Materials Characterization 156, p. 109872. DOI: 10.1016/j.matchar.2019.109872.

Breiman, Leo (2001): Random Forests. In Machine Learning 45 (1), pp. 5–32. DOI: 10.1023/A:1010933404324.

Clementi, Luis A.; Vega, Jorge R.; Gugliotta, Luis M.; Orlande, Helcio R.B. (2011): A Bayesian inversion method for estimating the particle size distribution of latexes from multiangle dynamic light scattering measurements. In Chemometrics and Intelligent Laboratory Systems 107 (1), pp. 165–173. DOI: 10.1016/j.chemolab.2011.03.003.

Cuzzi, Jeffrey N.; Olson, Daniel M. (2017): Recovering 3D particle size distributions from 2D sections. In Meteoritics & Planetary Science 52 (3), pp. 532–545. DOI: 10.1111/maps.12812.

Dalen, Gerard-van (2014): 2D & 3D particle size analysis of micro-CT images.

Dinis, P.; Castilho, A. (2012): Integrating Sieving and Laser Data To Obtain Bulk Grain-Size Distributions. In Journal of Sedimentary Research 82 (9), pp. 747–754. DOI: 10.2110/jsr.2012.62.

Eisenhour, Don D. (1996): Determining chondrule size distributions from thin-section measurements. In Meteoritics & Planetary Science 31 (2), pp. 243–248. DOI: 10.1111/j.1945-5100.1996.tb02019.x.

Evans, C. L.; Wightman, E. M.; Yuan, X. (2015): Quantifying mineral grain size distributions for process modelling using X-ray micro-tomography. In Minerals Engineering 82, pp. 78–83. DOI: 10.1016/j.mineng.2015.03.026.

Fandrich, Rolf; Gu, Ying; Burrows, Debra; Moeller, Kurt (2007): Modern SEM-based mineral liberation analysis. In International Journal of Mineral Processing 84 (1-4), pp. 310–320. DOI: 10.1016/j.minpro.2006.07.018.

Finch, James A.; Wills, B. A. (Eds.) (2016): Wills' mineral processing technology. An introduction to the practical aspects of ore treatment and mineral recovery. Eighth edition. Oxford, UK, Waltham, MA: Butterworth-Heinemann. Available online at http://proquest.tech.safaribooksonline.de/9780080970547.

Furat, Orkun; Leißner, Thomas; Ditscherlein, Ralf; Šedivý, Ondřej; Weber, Matthias; Bachmann, Kai et al. (2018): Description of Ore Particles from X-Ray Microtomography (XMT) Images, Supported by Scanning Electron Microscope (SEM)-Based Image Analysis. In Microscopy and microanalysis : the official journal of Microscopy Society of America, Microbeam Analysis Society, Microscopical Society of Canada 24 (5), pp. 461–470. DOI: 10.1017/S1431927618015076.

Goldsmith, P. L. (1967): The calculation of true particle size distributions from the sizes observed in a thin slice. In Br. J. Appl. Phys. 18 (6), pp. 813–830. DOI: 10.1088/0508-3443/18/6/317.

Harris, Marcia L.; Sapko, Michael J.; Zlochower, Isaac A.; Perera, Inoka E.; Weiss, Eric S. (2015): Particle size and surface area effects on explosibility using a 20-L chamber. In Journal of loss prevention in the process industries 37, pp. 33–38. DOI: 10.1016/j.jlp.2015.06.009.

Kramer, Mark A. (1991): Nonlinear principal component analysis using autoassociative neural networks. In AIChE J. 37 (2), pp. 233–243. DOI: 10.1002/aic.690370209.

Lampinen, Jouko; Vehtari, Aki (2001): Bayesian approach for neural networksÐreview and case studies.

Legland, David; Arganda-Carreras, Ignacio; Andrey, Philippe (2016): MorphoLibJ: integrated library and plugins for mathematical morphology with ImageJ. In Bioinformatics (Oxford, England) 32 (22), pp. 3532–3534. DOI: 10.1093/bioinformatics/btw413.

Leißner, Thomas; Peuker, Urs (2017): 3D Xray microscopy computed tomography (poster).

Li, He; Li, Jingwen; Bodycomb, Jeffrey; Patience, Gregory S. (2019a): Experimental Methods in Chemical Engineering. Particle Size Distribution by Laser Diffraction—PSD. In Can. J. Chem. Eng. 97 (7), pp. 1974–1981. DOI: 10.1002/cjce.23480.

Li, He; Li, Jingwen; Bodycomb, Jeffrey; Patience, Gregory S. (2019b): Experimental Methods in Chemical Engineering: Particle Size Distribution by Laser Diffraction—PSD. In Can. J. Chem. Eng. 97 (7), pp. 1974–1981. DOI: 10.1002/cjce.23480.

Mees, F.; Swennen, R.; van Geet, M.; Jacobs, P. (2003): Applications of X-ray computed tomography in the geosciences. In Geological Society, London, Special Publications 215 (1), pp. 1–6. DOI: 10.1144/GSL.SP.2003.215.01.01.

MILLER, J. D.; LIN, C. L.; CORTES, A. B. (1990): A Review of X-Ray Computed Tomography and Its Applications in Mineral Processing. In Mineral Processing and Extractive Metallurgy Review 7 (1), pp. 1–18. DOI: 10.1080/08827509008952663.

Olawuyi, Babatunde James; Asante Samuel (2016): Particle size distribution methods as adopted for different materials.

Orive, L. M. (1976): Particle size-shape distributions. The general spheroid problem. I. Mathematical model. In Journal of microscopy 107 (3), pp. 235–253. DOI: 10.1111/j.1365-2818.1976.tb02446.x.

Rickman, Douglas; Lohn-Wiley, Blake; Knicely, Joshua; Hannan, Brian (2016): Probabilistic solid form determined from 2D shape measurement. In Powder Technology 291, pp. 466–472. DOI: 10.1016/j.powtec.2015.10.044.

Russ, John C.; Dehoff, Robert T. (2000): Practical Stereology. Boston, MA: Springer US.

Sahagian, Dork L.; Proussevitch, Alexander A. (1998): 3D particle size distributions from 2D observations. Stereology for natural applications. In Journal of Volcanology and Geothermal Research 84 (3-4), pp. 173–196. DOI: 10.1016/S0377-0273(98)00043-2.

Schlüter, Steffen; Sheppard, Adrian; Brown, Kendra; Wildenschild, Dorthe (2014): Image processing of multiphase images obtained via X-ray microtomography. A review. In Water Resour. Res. 50 (4), pp. 3615–3639. DOI: 10.1002/2014WR015256.

Shelhamer, Evan; Long, Jonathan; Darrell, Trevor (2017): Fully Convolutional Networks for Semantic Segmentation. In IEEE transactions on pattern analysis and machine intelligence 39 (4), pp. 640–651. DOI: 10.1109/TPAMI.2016.2572683.

Skubacz, Krystian; Wojtecki, Łukasz; Urban, Paweł (2016): The influence of particle size distribution on dose conversion factors for radon progeny in the underground excavations of hard coal mine. In Journal of environmental radioactivity 162-163, pp. 68–79. DOI: 10.1016/j.jenvrad.2016.05.020.

Tomas (2014): Mechanische Verfahrenstechnik - Partikeltechnologie.

Wu, Jiangyu; Feng, Meimei; Xu, Jingmin; Qiu, Peitao; Wang, Yiming; Han, Guansheng (2018): Particle Size Distribution of Cemented Rockfill Effects on Strata Stability in Filling Mining. In Minerals 8 (9), p. 407. DOI: 10.3390/min8090407.

ZHOU, Jian; Li, Chuanqi; Arslan, Chelang A.; Hasanipanah, Mahdi; Bakhshandeh Amnieh, Hassan (2019): Performance evaluation of hybrid FFA-ANFIS and GA-ANFIS models to predict particle size distribution of a muck-pile after blasting. In Engineering with Computers 47 (3), p. 476. DOI: 10.1007/s00366-019-00822-0.